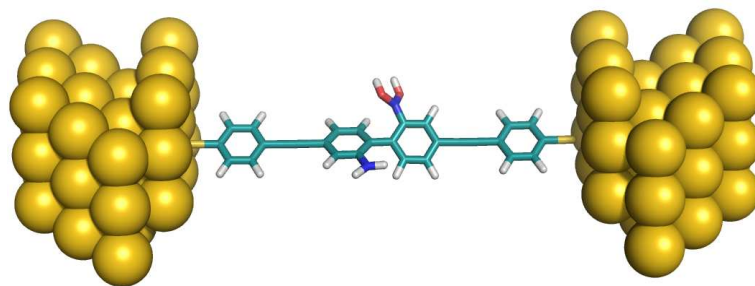


Theoretical Modeling and Simulation of Electron-Phonon Scattering Processes in Molecular Electronic Devices

Alessio Gagliardi



Theoretical Modeling and Simulation of Electron-Phonon Scattering Processes in Molecular Electronic Devices

Dissertation zur Erlangung des akademischen Grades
Doktor der Naturwissenschaften (Dr. rer. nat.)
vorgelegt dem
Department Physik der Fakultät für Naturwissenschaften
Universität Paderborn

Dipl. Ing. Alessio Gagliardi

Paderborn, 2007

Dem Department Physik der Fakultät für Naturwissenschaften als Dissertation vorgelegt.

Eingereicht am: 4.5.2007
Tag der mündlichen Prüfung: 29.6.2007

Promotionskommission

Vorsitzender	Prof. Dr. Artur Zrenner
Erstgutachter	Prof. Dr. Thomas Frauenheim
Zweitgutachter	Prof. Dr. Wolf Gero Schmidt
Drittgutachter	Prof. Dr. Aldo Di Carlo
Beisitzer	Prof. Dr. Torsten Meier

Copyright statement

Chapter 6 reproduced with permission from A. Gagliardi, A. Pecchia, A. Di Carlo, S. Sanna, Th. Frauenheim and R. Gutierrez, Nano Letters, Vol. 4, 2109. Copyright 2004 American Chemical Society.

Chapter 7 reproduced in part with permission from, A. Gagliardi, G. C. Solomon, A. Pecchia, J. R. Reimers, A. Di Carlo, Th. Frauenheim, N. S. Hush, Journal of Chemical Physics, Vol. 124, 094704. Copyright 2006 American Institute of Physics.

Chapter 8 reproduced in part with permission from A. Gagliardi, G. C. Solomon, A. Pecchia, J. R. Reimers, A. Di Carlo, Th. Frauenheim, N. S. Hush, Nano Letters, Vol. 6, 2431. Copyright 2006 American Chemical Society. Journal of Chemical Physics, Vol.125, 184702. Copyright 2006 American Institute of Physics.

Chapter 9 reproduced in part with permission from A. Gagliardi, G. C. Solomon, A. Pecchia, J. R. Reimers, A. Di Carlo, Th. Frauenheim, N. S. Hush, Physical Review B, Vol. 75, 174306. Copyright 2007 American Physical Society.

Archiv

Elektronische Dissertationen und Habilitationen der Universität Paderborn
<http://www.ub.upb.de/ebibliothek/hochschulschriften/ediss>

Alessio Gagliardi, *Theoretical Modeling and Simulation of Electron-Phonon Scattering Processes in Molecular Electronic Devices*. PhD Thesis (in English), Department of Physics, Faculty of Science, University of Paderborn, Germany (2007).

Abstract

The entire field of molecular electronics relies on a very simple concept: a single organic molecule, or a thin layer of organic molecules, are used as a bridge between two metallic contacts. The bias applied induces a current from one contact to the other. The basic idea is that the current is dominated by the chemical properties of the molecule between the contacts and that this electric characteristic can be easily tuned by an external perturbation in order to get a switch. However, despite the intense investigation many issues are still waiting to be fully addressed. One of them is the dissipation induced in the molecule by the coupling between the vibrational modes and the charge carriers. Due to the size of the device this interaction must be described quantum mechanically via an electron-phonon scattering process. The quantitative evaluation of dissipation in molecular electronics is fundamental for the entire field, especially for future introduction of such kind of devices in the electronic industry.

The author of this work and Dr. Alessandro Pecchia of the University of Rome "Tor Vergata" have implemented a code based on non-equilibrium Green's functions formalism to investigate electron-phonon scattering in molecular devices. The first application presented is the evaluation of the dissipation in octanedithiols sandwiched between two gold contacts showing which are the most relevant modes in scattering electrons. The electron-phonon scattering is much more than the study of the "quantum resistance". The inelastically scattered electrons in fact can be directly used as probes to investigate the geometry and the electronic structure of the device. This spectroscopy technique is called inelastic electron tunneling spectroscopy (IETS). Despite the IETS is an old spectroscopy technique, its application in the molecular electronic field is recent and many features need to be fully understood.

The electron-phonon code has been used to investigate the properties of IETS, first simulating directly IETS in octane-thiol systems, later on addressing the problem of selection rules in this spectroscopy technique. It is well known in fact that the selectivity of IETS is rather different from the one of other more conventional techniques, like infrared or Raman. However the lack of a precise knowledge of selection rules in IETS renders a clear assignment of IET spectra difficult.

The definition of selection rules requires two steps. First, the definition of the point group of the system. It is obvious that, also if the molecule in the gas phase shows high symmetry, this will be reduced by the presence of the electrodes and the distortions of the structure. Despite that, the molecule remains the dominant feature of IETS measurements. We can univocally identify the point group of the device just taking the point group of the unperturbed molecule and reducing it to a subgroup due to the effects of the electrodes. The second issue is to define a basis set to which the point group is applied to. It is well known that canonical molecular orbitals are not the best choice due to the strong interference effects between them during transport. However, the current can be decomposed in a sum of independent "channels" obtained diagonalizing directly the operator involved in the transmission and not the Hamiltonian. The choice of this set of channels is not unique, but all of them permit to avoid interference.

These tools have been applied to investigate IETS in a benzenedithiols molecule between model gold contacts. The interpretation of the current in terms of independent channels provides not only information about selection rules, but also in which region electrons are scattered, leading to a deep comprehension of where the dissipation occurs and which chemical substitutions in the device can improve its performances.

Alessio Gagliardi, *Theoretische Modellierung und Simulation von Elektron–Phonon Streuprozessen in Molekularelektronischen Bauteilen*. Dissertation (in englischer Sprache), Department Physik, Fakultät für Naturwissenschaften, Universität Paderborn (2007).

Kurzfassung

Das Gebiet der Molekularelektronik beruht auf einem einfachen Konzept: Ein einzelnes oder eine dünne Schicht organischer Moleküle verbindet zwei metallische Kontakte. Das Anlegen einer Spannung induziert einen Strom von einem Kontakt zum anderen. Die Grundidee ist, dass der Strom wesentlich von den chemischen Eigenschaften des Moleküls zwischen den Kontakten abhängt und dass diese elektronische Charakteristik leicht mit Hilfe einer äußeren Störung gestimmt werden kann, um einen Schalter zu realisieren. Trotz intensiver Untersuchungen warten jedoch viele Aspekte noch immer auf ihre eingehende Behandlung. Einer davon ist die Dissipation, welche im Molekül durch die Kopplung zwischen den vibronischen Moden und den Ladungsträgern verursacht wird. Durch die Größe des Bauteils muss diese Wechselwirkung quantenmechanisch durch einen Elektron–Photon Streuprozess beschrieben werden. Die quantitative Auswertung der Dissipation ist fundamental für das gesamte Feld der Molekularelektronik, insbesondere in Hinblick auf die industrielle Anwendungen.

Der Autor dieser Arbeit und Dr. Alessandro Pecchia von der Universität von Rom “Tor Vergata” haben einen Code implementiert, der auf dem Nichtgleichgewichts–Green–Funktionen–Formalismus basiert, um Elektron–Phonon Streuung in molekularen Bauteilen zu untersuchen. Die erste Anwendung ist die Berechnung der Dissipation in Oktanthiolat eingebettet zwischen zwei Goldkontakten, die zeigt, welches die relevantesten Moden bei der Elektronenstreuung sind, eine fundamentale Frage für die Stabilität des Bauteils. Die inelastische Streuung umfasst jedoch weitaus mehr als eine Untersuchung des “Quantenwiderstands” des Bauteils. Die inelastisch gestreuten Elektronen können direkt als Sensor für die Geometrie und Elektronenstruktur des Bauteils verwendet werden. Diese spektroskopische Technik wird als Inelastische Elektronen–Tunnel–Spektroskopie (IETS) bezeichnet. Obwohl bereits recht alt, ist die IETS auf dem Gebiet der Molekularelektronik neu, und viele Eigenschaften müssen erst noch verstanden werden.

Der Elektron–Photon Code wurde verwendet, um die Eigenschaften der IETS zu untersuchen, zunächst durch direkte Simulation des IETS in Oktandithiol–Systemen, später, um das Problem der Auswahlregeln anzugehen. Tatsächlich ist es bekannt, dass die Selektivität der IETS sehr verschieden von der anderer, konventionellerer Techniken wie Infrarot oder Raman ist. Das Fehlen einer genauen Kenntnis über die Auswahlregeln in der IETS gestaltet eine klare Zuordnung der Spektren schwierig. Die Definition von Auswahlregeln erfordert zwei Schritte. Zuerst muss die Punktgruppe des Systems festgelegt werden. Auch wenn das Molekül in der Gasphase hochsymmetrisch ist, ist es offensichtlich, dass die Symmetrie durch Anwesenheit der Elektroden und strukturelle Verzerrungen verringert wird. Dennoch bleibt das Molekül das wesentliche Merkmal der IETS Messungen. Unter Berücksichtigung des wesentlichen Effekts der Elektroden, können wir die Punktgruppe des Systems eindeutig definieren als diejenige des ungestörten Moleküls, abzüglich aller End–End–Symmetrieoperationen. Das zweite Problem besteht darin, einen geeigneten Basisatz zu finden. Es ist wohl bekannt, dass kanonische Molekülorbitale nicht die beste Wahl sind, wegen der starken Interferenzeffekte zwischen ihnen während des Transports. Der Strom kann jedoch in eine Summe voneinander unabhängiger “Kanäle” zerlegt werden, die man durch Diagonalisierung der Matrix des Transmissionsoperators (nicht des Hamiltonians) erhält. Die Wahl dieser Menge von Kanälen ist nicht eindeutig, jede Wahl ermöglicht es jedoch, Interferenz zu vermeiden. Die Interpretation des Stromes mit Hilfe unabhängiger Kanäle liefert auch Informationen darüber, wo die Elektronen gestreut werden, was zu einem tiefer gehenden Verständnis führt, wo die Dissipation stattfindet und welche chemischen Substitutionen am Bauteil die Leistungsfähigkeit des Bauteils erhöhen können.

Contents

Introduction	1
1 Molecular Electronics: a Brief Overview	5
1.1 Molecular electronics experimental techniques	6
1.1.1 Break junction experiments	6
1.1.2 Molecular monolayer devices	8
1.1.3 Nanopores	10
1.1.4 Electromigration experiments	11
1.1.5 Scanning tunneling microscope experiments	12
1.2 Inelastic electron tunneling spectroscopy	13
2 Modeling Molecular Electronic Devices	17
2.1 The general problem of molecular conduction	18
2.2 The Hamiltonian of the system	20
2.3 From the Hamiltonian to the current: Meir-Wingreen equation	22
2.4 Lifetimes of interest	26
3 Non-Equilibrium Green's Functions	29
3.1 Three representations	30
3.1.1 Schrödinger representation	30
3.1.2 Heisenberg representation	31
3.1.3 Interaction representation	31
3.2 S -Matrix	32
3.3 Equilibrium Green's functions	33
3.4 Wick's theorem	34
3.5 Feynman's diagrams	36
3.6 Dyson's equation	39
3.7 Time-loop S -matrix: NEGF	41
3.7.1 Dyson's equations for NEGF	44
4 Density Functional Based Tight-Binding	47
4.1 DFT and Kohn-Sham formulation	48

4.1.1	The Kohn-Sham equations	49
4.2	DFTB: method and approximations	51
4.2.1	Pseudo-atomic starting density	52
4.2.2	Tight-binding integrals and the two-centre approximation	53
4.2.3	Repulsive potential	54
4.2.4	Second-order correction	55
4.2.5	DFTB secular equation	57
4.3	Disadvantages of DFT in transport simulations	58
5	The Electron-Phonon Code	61
5.1	Approximations in the electron-phonon code	62
5.2	The scheme of the device and the open boundary conditions	64
5.3	The electron-phonon self-energies	66
5.4	Computation of the electron-phonon couplings	68
5.5	The flowchart of the code	69
6	Power Dissipation in Molecular Electronic Devices	73
6.1	Dissipation in alkanethiols	74
6.1.1	Geometry and vibrational modes	74
6.1.2	Power dissipation in the molecule	75
7	Simulation of Inelastic Electron Tunneling Spectroscopy in Alkanethiols	81
7.1	IETS approximation	81
7.2	The choice of binding site	82
7.2.1	Atomic partitioning of the system	83
7.2.2	Correction of the DFTB vibrational frequencies	84
7.3	Discussion of the IETS simulations	84
7.3.1	Nature of the orbitals controlling conduction and IETS	88
7.3.2	Nature of the vibrations that produce IETS	89
7.4	Conclusions	91
8	The Role of Symmetry and Channels in Conduction	93
8.1	The definition of the symmetry of conduction	94
8.1.1	Application to molecular system	95
8.2	The definition of channels in elastic transport	99
8.2.1	Büttiker channels	100
8.2.2	Γ -channels	103
8.3	Conclusions	106
9	Propensity Rules in IETS	109
9.1	Theoretical formalism	109
9.2	From Γ -channels to A-channels	111
9.3	Propensity rules in IETS	118
9.4	Conclusions	121

Conclusion	123
A Atomic Units	127
B Surface Green's Function: Decimation Technique	129
Bibliography	133
Own Publications	145
Personal Contributions	147
Acknowledgments	148

Introduction

[...] I don't know how to miniaturize a computer on a small scale in a practice way, but I do now that computing machines are very large; they fill rooms. Why can't we make them very small, make them of little wires, little elements and by little, I mean little. [...]

[...] But there is plenty of room to make them smaller. There is nothing that I can see in the physical laws that says the computer elements cannot be made enormously smaller than they are now [...]

[...] It is not an attempt to violate any laws; it is something, in principle, that can be done; but, in practice, it has not been done because we are too big [...]

Richard P. Feynman **There is a plenty of room at the bottom**, 1959.

The idea of engineering at molecular scale has always been a dream of scientists. In his speech quoted at the beginning of this introduction, Feynman, more than fifty years ago, remarked that “there is a plenty of room at the bottom” to miniaturize our devices up to a very microscopic scale.

In the last 30 years, the silicon metal oxide semiconductor (MOS) field-effect transistor (FET) has been the foundation of integrated circuits [1]. In the 70s, integrated circuits contained thousands of MOSFETs, each having dimensions of tens of micrometres. Today's chips contain almost one billion MOSFETs, each having physical dimensions of tens of nanometres. The exponential increase of device density (Moore's Law [2]) and scaling of device dimension into the nanotechnology regime (see Fig. (1)) have resulted in the vast improvements observed in numerous electronic devices, from PCs to control systems found in airplanes.

Although substantial innovation was required to realize this rate of dimensional scaling, until recently very little has changed in the materials and design of the basic MOSFET. In the future, a variety of new materials and device structures will be required to continue MOSFET scaling [3, 4, 5, 6]. Furthermore, as silicon MOSFET technology approaches its limits [7], entirely new device structures and computational paradigms will be required to replace and improve traditional MOSFETs. These possible emerging technologies span from transistors made of silicon nanowires to devices made of nanoscale molecules.

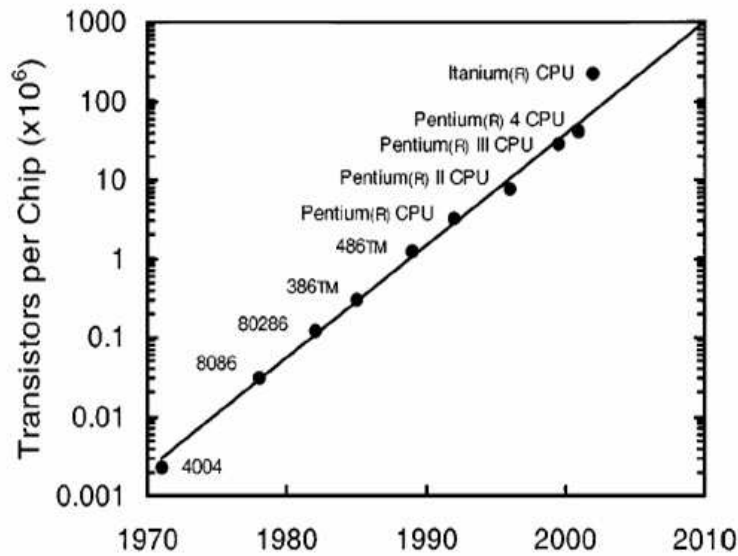


Figure 1: *The Moore's Law in a diagram: the exponential growth of the number of transistors on a single chip in the last thirty years.*

Independently the future of electronics will be based on nanoscale planar silicon MOS-FETs or an emerging technology which totally replaces the MOSFET, the electronic properties of all of these nanodevices are extremely susceptible to small perturbations in properties such as dimension, structure, roughness and defects, which means there is a significant need for precise metrology. Furthermore, the insertion of a variety of new materials into the conventional MOSFET and radically new materials and devices for potential emerging replacement technologies (for example, molecular and spin electronics) present further challenges for metrology. Although the devices and materials being considered for future MOS technologies and beyond are broad, the overarching challenges to metrology remain. The ability to measure the physical, chemical and electronic properties that control final device electrical characteristics will be crucial to the research and development of future electronic devices.

In this rush to get smaller and faster devices, molecular electronic represents the ultimate frontier. The potential for molecular electronics originates from its nanoscale dimension, the possibility of synthesizing very specific electronic properties, and the promise of fabrication through self-assembly. Although numerous molecular devices have been demonstrated, there is still significant controversy concerning the repeatability of measurements and the understanding of charge transport [8, 9, 10]. Many problems are related to the difficulties to investigate the geometry and the electronic structure of the molecule connected to the metal electrodes. The final device structure dramatically changes the intended electronic properties of the material of interest. The interaction between the electrodes and molecules is critical to understand the transport properties of the final device. Forming ohmic but non-interacting metallic contacts to molecules is a specific problem. A new set of experimental techniques, such as inelastic tunneling spectroscopy, which probes

vibrational modes of the molecules through measurement of the device current-voltage behavior, have been developed to determine which molecular species and bonds are present in the final device structure [10]. New effects can arise creating a completely new kind of electronics, such as Kondo effect [11], negative differential resistance [12] or Coulomb blockade [11]. All these new problems, techniques and effects represent a continuous challenge for researchers.

The silicon electronics has been a technological and economic engine for over thirty years. Metrology has been an important infrastructure enabling the exponential increase of device density and exponential decrease of device dimension. New nanoscale materials and devices will be required to sustain this technological revolution but the extreme sensitivity of the electronic properties of these devices to their nanoscale physical properties and the insertion of radically new materials present significant challenges for their development. The ability to measure the physical, chemical and electronic properties of these new materials and devices will become even more critical in continuing the advance of the MOS and finding technologies to extend or replace it.

Concluding, “there is a plenty of space at the bottom” and we are just scratching the surface.

Molecular Electronics: a Brief Overview

In this Chapter is given a brief introduction to some of the most important experimental techniques which are gaining popularity in the molecular electronic field. The techniques presented are not the only in existence and also for the techniques enlisted here are many variants not mentioned. However, a very detailed discussion of all methods to create molecular devices is beyond the scope of this work. The techniques described have been selected not only for their importance, but also for the relevance they have in the present work.

The setup of molecular electronic devices, despite the wide spectrum of variation that have been developed in the recent years, can be summarized in few words: an organic or inorganic molecule, or a thin layer of molecules, bridging two contacts. The geometry can be very different from one device to the other as much as the molecules used and the materials of the electrodes. Moreover a gate can or cannot be present. This has produced a wide range of possibilities for this kind of devices, nevertheless the main characteristic of the device remains the molecule (or molecules) used to create the bridge. In fact the very basic idea of molecular electronics is that the electronic properties of the bridging molecules can be used directly to create a switch, and in electronics a switch is the first step to define a logic circuit.

The first experiments for molecular electronics concerned mainly measurements of conductivity, because this is the first, the easiest and, in many respects, the most important quantity we want to know about an hypothetic molecular device. Nevertheless, in the following years, other aspects have become more and more important. The discovery of very peculiar effects related to the strong confinement of the electrons in the molecular device region, important spin-spin correlation processes and many other properties related to the quantum nature of the physics at molecular scale have started to be investigated experimentally and theoretically. Moreover another important issue has become very popular: the dissipation in these devices. It is obvious that if a current is flowing in this tiny molecular bridge a certain degradation of the flux of current must be expected.

However, the magnitude and the quality of this degradation, that we can address as a sort of “quantum resistance”, are still under investigation. Even more, the dissipation is certainly a fundamental ingredient to address the stability of electronic devices, in fact

only a complete understanding of the exchange of energy between the environment and the molecule can give an insight into the mechanisms which underlie the conduction in the device. Finally, the electrons inelastically scattered can be directly used as probes to investigate the device itself as in the Inelastic Electron Tunneling Spectroscopy (IETS). The last part of this Chapter is devoted to describe the IETS due to the relevance this technique has in the present work.

Of all the experimental setups described in this Chapter Nanopores and Molecular Break-Junction are certainly the most important for the present work. Finally a remark: every technique is offering particular advantages and drawbacks, but, so far, none of them can be viewed as a “standard model” for experimental setup and all of them are far away from being implemented on an industrial scale to yield commercial devices. Contacting and manipulating few molecules between bulk contacts on the nanometer scale in a reliable and reproducible fashion still constitutes a scientific and engineering challenge.

1.1 Molecular electronics experimental techniques

1.1.1 Break junction experiments

The use of Mechanically Controlled Break-Junctions (MCBJ) [14, 15] for contacting single molecules is a further development of single-atom contact conductance experiments [16, 17]. The gap to introduce the molecules which will form the bridge is created by elongating a metal wire by a mechanical stress. Shortly before breaking, the contact between the two halves reduces to one single atom. Further elongation yields an atomic chain of gold atoms until the wire finally breaks. The design principal of MCBJ device is simple: a thin gold film is structured, using *e*-beam lithography, on an elastic substrate. The gold film is designed to have a constriction. By underetching this constriction, a freestanding bridge is created. The sample is placed in a bending mechanism as depicted in Fig. (1.1).

The very precise control of the bending is allowed by a three point geometry. To avoid contaminations, the bending mechanism is placed in a vacuum chamber. The pushing rod (a piezoelectric element) is moved upward until the bridge breaks. The upward movement is converted, by the bending of the substrate, in a variation of the distance between the two halves of the metallic sample. The control of this movement is extremely precise, up to 0.1 Å. Now, the contacts are opened and closed repeatedly until quantized conductance values are observed, corresponding to the formation of a sharp atomic point contacts.

Then the chamber is filled with an inert gas (like argon) and a solution of the molecule (with terminal protective groups attached to the thiol groups) to be measured is applied on the opened contacts. The terminal group prevents the molecules from forming clusters and only attach in contacts with the gold forming a stable covalent bond between sulfur and the gold. The thiol group is the most popular choice because the strong covalent bond it forms with the gold atoms. After a while the solvent will evaporate and some of the molecules will loose their protection terminal group and the sulfur will chemically bind to one electrode.

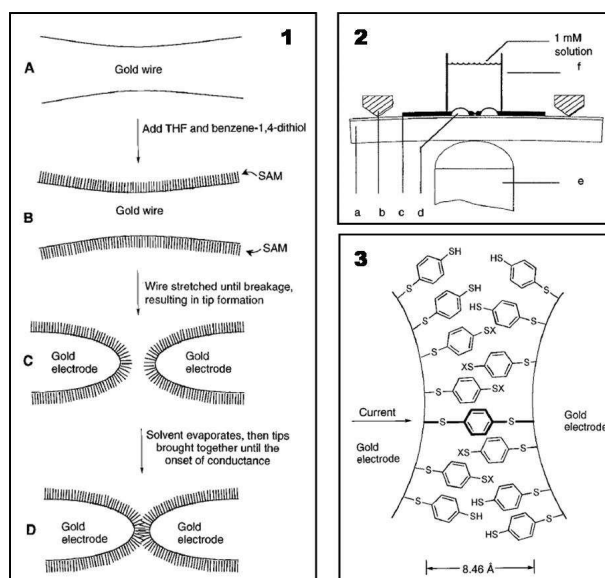


Figure 1.1: **1)** Schematic of the measurement process. (A) The gold wire of the break junction before breaking and tip formation. (B) After addition of the molecule (in this case benzene-1,4-dithiol in a tetrahydrofuran (THF) solution), layers form on the gold wire surfaces. (C) Mechanical breakage of the wire in solution produces two opposing gold contacts that are covered by a layer of molecule each. (D) After the solvent is evaporated, the gold contacts are slowly moved together until the onset of conductance is achieved. **2)** A schematic of the experimental setup with (a) the bending beam, (b) the counter support, (c) the notched gold wire, (d) the glue contacts, (e) the piezo element, (f) the glass tube containing the solution. **3)** A schematic of a benzene-1,4-dithiolate layer of molecule between proximal gold electrodes formed in a MBE. The thiolate is normally H terminated after deposition; end groups denoted as X can be either H or Au, with the Au potentially arising from a previous contacts/retraction event. These molecules remain nearly perpendicular to the Au surface, making other molecular orientations unlikely (from [13]).

To remove molecules that are not chemically bound to the gold, the junction is rinsed with a solvent. After evacuation, the bridge is slowly closed with bias voltage applied. Due to the small distance between the two electrodes, a high electric field is present, in which the molecules orient themselves toward the opposite electrode. At one point, the first molecules will reach the second electrode and chemically bind to it. This situation can be recognized by a plateau in the current. Now, current-voltage curves can be recorded. Break-junction offer the best control for single-molecules experiments [13, 18, 19, 20, 21], nevertheless the main drawback of the technique is the impossibility to introduce a gate in the device due to the large diameter of the breaking gold wire. Every gate electric field is in fact completely screened by the metal.

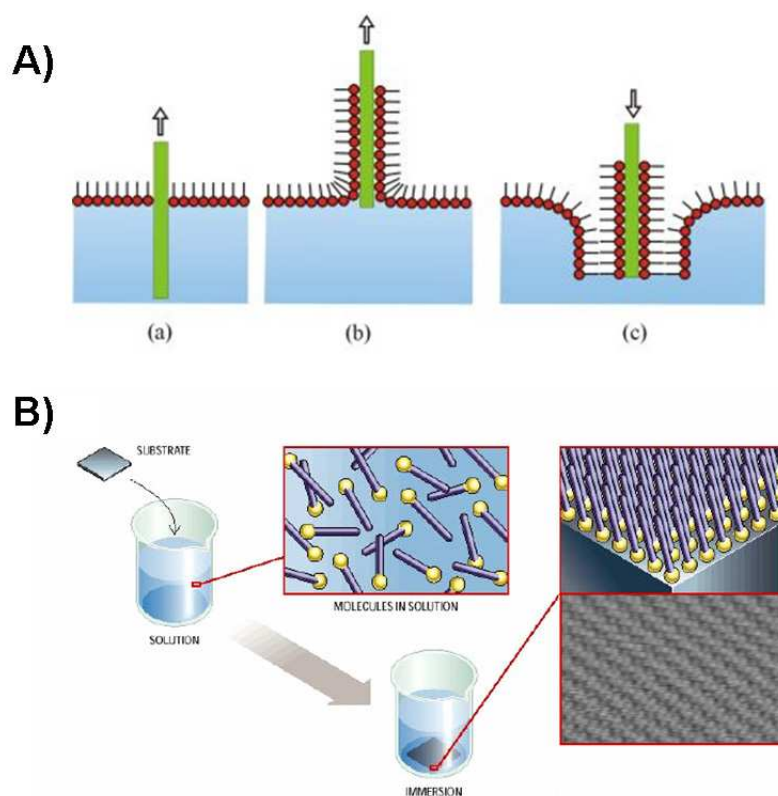


Figure 1.2: **A)** Langmuir-Blodgett (LB) films: a layer of molecules with an hydrophilic group is laying on the surface of water. The solid substrate is merged in the water (a). When the layer is compressed the molecules start to climb to the solid substrate (b). The step can be repeated to get multi-layers systems (c). **B)** A self-assembled monolayer structure (SAM) formed by molecules with a thiol group in solution with a metallic substrate. The molecules, after a while, bind to the substrate.

1.1.2 Molecular monolayer devices

The main difference between this approach and the former is that more than one molecule is used to make the device. The principal advantage relates to the simplicity to produce well structured layers. The substrate of the layer act as one of the electrode while the second is then evaporated on top, yielding a film device, or it is a Scanning Tunneling Microscope (STM) tip. The main difficulty in film devices is the deposition of the second electrode that can easily damage the monolayer. Although working devices are achieved in most cases, the actual microscopic structure of the measured device (structural integrity of the monolayer, defects) is still not clear [22]. Several devices based on sandwiching molecular films between two electrodes have been reported [23, 24, 25]. Different techniques can be applied to produce a molecular monolayer: Langmuir-Blodgett films and Self-Assembled Monolayers. Due to the simplicity of their formation these devices are very promising

possibilities for the future of molecular electronics, especially for hybrid devices which combine with more standard electronics.

Langmuir-Blodgett films (LB): Langmuir-Blodgett films consist of mono-molecular layers stacked sequentially onto a solid substrate. A solid substrate, covered by a hydrophilic material, is lowered into the water, breaking through the LB film which stays on the surface of the liquid. The molecules of the LB must contain a hydrophilic group, e.g. acid or alcohol group, and a hydrophobic group, usually an aliphatic chain, to allow film formation on the surface of the water. In water, all the molecules will then align in the same direction with the hydrophilic end at the water side. A continuous monolayer, which can later be transferred on the substrate, is formed by compression of the film using a moveable barrier. The substrate is slowly removed from the bath while at the same time the barrier is shifted to keep the monolayer intact. This way, a well-ordered monolayer of the organic molecule is formed on the surface of the substrate (see Fig. (1.2, a)). The big disadvantage of this method is that the molecules are not chemically bound to the substrate, as a hydrophilic group is required on the substrate side of the molecule.

Self-Assembled Monolayers (SAMs): Molecular self-assembly is a very well known strategy for nano-fabrication that involves designing molecules and supramolecular entities so that shape-complementarity causes them to aggregate into desired structures. Self-assembly has a number of advantages as a strategy: first, it carries out many of the most difficult steps in nano-fabrication, those involving atomic-level modification of structure, using the very highly developed techniques of synthetic chemistry. Second, it draws from the enormous wealth of examples in biology for inspiration: self-assembly is one of the most important strategies used in biology for the development of complex, functional structures. Third, it can incorporate biological structures directly as components in the final systems. Fourth, because it requires that the target structures be the thermodynamically most stable ones open to the system, it tends to produce structures that are relatively defect-free and self-healing.

Although there are countless examples of self-assembly all around us the basic rules that govern these assemblies are not understood in useful detail, and self-assembling processes cannot, in general, be designed and carried out “to order”. Many of the ideas that are crucial to the development of this area: “molecular shape”, the interplay between enthalpy and entropy, the nature of non-covalent forces that connect the particles in self-assembled molecular aggregates, are simply not yet under the control of investigators. In the typical SAM setup for molecular electronics the monolayer forms from molecules in solution on the substrate itself, due to the properties of the molecules [23]. These systems – self-assembled monolayers (SAMs) – are reasonably well understood, and increasingly useful technologically. The crucial dimension in SAMs is the thickness perpendicular to the plane of the monolayer: this dimension, and the composition along this axis, can be controlled very simply at the scale of 0.1 nm by controlling the structures of the molecules making up the monolayer. After a layer has formed, the substrate is removed from the solution (see Fig. (1.2, b)). The second electrode can then be evaporated on top of the molecular layer. Many measurements using SAM devices have been reported [24, 26]. For SAMs

the technique is simpler than LB and chemical bonds to the substrate can and have to be achieved.

1.1.3 Nanopores

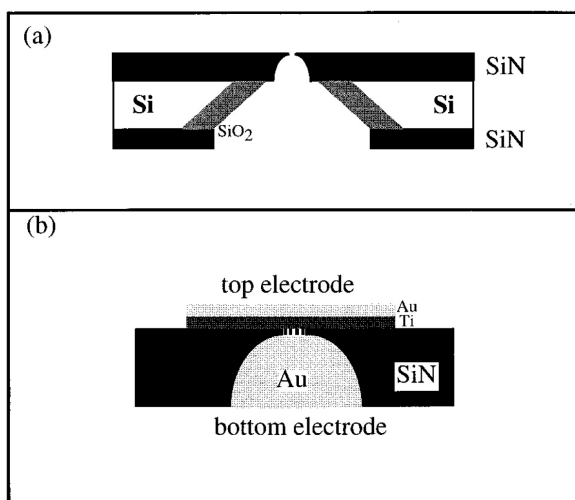


Figure 1.3: *Fabrication of the heterostructure. (a) Cross section of a silicon wafer showing the bowl-shaped pore etched in suspended SiN membrane with a diameter about 300 Å. (b) Au-Ti top electrode/self-assembled monolayer/Au bottom electrode sandwich structure in the nanopore (see [27]).*

The idea of nanopore links directly to the one of SAM. The idea is to have a small hole in which deposit a smaller number of molecules than in SAMs and LBs techniques. The self-assembling properties of the molecules and the confinement of the hole lead the system to form a well structured layer. The first measurement of conduction with nanopores was presented by Zhou and Reed [27] at the same time of their publication of break-junction experiment. The hole is etched into a freestanding silicon nitride layer by reactive ion etching. After the etching, gold is evaporated onto the hole from underneath. Then a SAM is allowed to form on the evaporated gold. Finally, titanium and gold are evaporated from above to yield the molecular device (Fig. (1.3)). The main advantage of this structure is its stability and the reduction of size if compared to more traditional monolayers devices. The big disadvantage is the deposition of the second electrode, the effects of that are still not clear as for SAMs, moreover it is not clear which is the interaction between the titanium and the molecules.

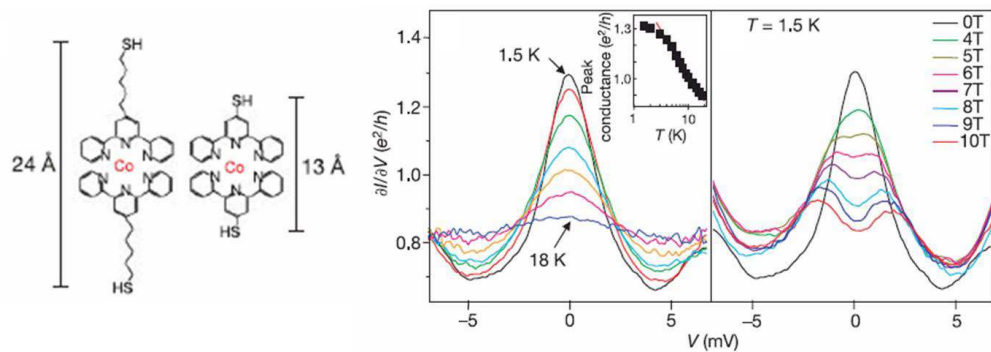


Figure 1.4: Kondo effect in a single molecule device. Experiment by J. Park *et al.* [11] using electromigration contacts. Left: molecules investigated, consisting of a Co ion trapped in a cage of benzene rings. Right: observed Kondo peak in the shorter molecule. Displayed is the differential conductance over bias voltage in V . Different traces correspond to different temperatures. The inset shows the decrease of the peak height with temperature.

1.1.4 Electromigration experiments

Devices fabricated by electromigration offer the possibility to study the influence of a gate electrode. Usually, a 10 to 15 nm wide wire is fabricated on a SiO_2 insulating layer using e -beam lithography [28]. A doped Si substrate underneath the SiO_2 can be used as a gate electrode. After adding a solution of the molecules to be investigated onto the wire, the single-molecule contact is then created by breaking the wire through electromigration: at low temperature the applied bias voltage is increased to large values until the wire breaks. This produces a gap of about 1 to 2 nanometers, across which in about 10% of the samples a molecule is found, so that the current-voltage characteristic can be recorded. Using the electromigration technique, J. Park *et al.* [11] managed to observe the Kondo effect (see Fig. (1.4)) and the Coulomb blockade effect in single molecules consisting of a cobalt ion trapped in a polypyridyl cage. For the longer, less conducting molecule, a conductance gap for small bias voltage was observed. In dependence of the gate voltage different threshold bias values were necessary until the current increased, corresponding to Coulomb blockade behavior. 2D plots of conductance in dependence of applied bias and gate voltage yielded Coulomb diamonds. For the shorter molecule, where the cobalt-ion acted as an “impurity spin” a Kondo resonance was reported: at zero bias, a peak in the difference conductance has been reported, that has a logarithmic temperature dependence with temperature between 3 K and 20 K.

As a second test, a magnetic field was applied which resulted in a split of the peak, as would be expected from Kondo physics. A second group, H. Park *et al.* [29], also observed a Kondo resonance in single molecules using electromigration techniques to contact the molecules. There are many other experiments that make use of the electromigration technique to contact single molecules [29, 30, 31].

1.1.5 Scanning tunneling microscope experiments

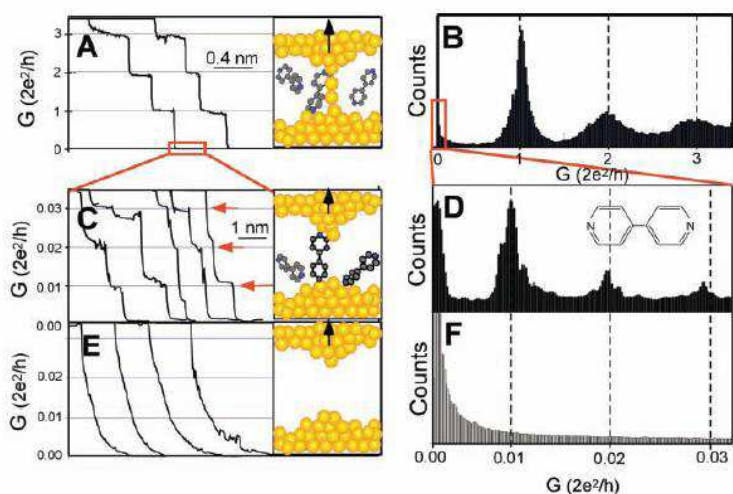


Figure 1.5: (A) Conductance of a gold contact formed between a gold STM tip and a gold substrate decreases in quantum steps near multiples of $G_0 = (2e^2/h)$ as the tip is pulled away from the substrate. (B) A corresponding conductance histogram constructed from 1000 conductance curves as shown in (A) shows well-defined peaks near $1 G_0$, $2 G_0$, and $3 G_0$ due to conductance quantization. (C) When the contact shown in (A) is completely broken, corresponding to the collapse of the last quantum step, a new series of conductance steps appears if molecules such as 4,4' bipyridine are present in the solution. These steps are due to the formation of the stable molecular junction between the tip and the substrate electrodes. (D) A conductance histogram obtained from 100 measurements as shown in (C) shows peaks near $1 \times$, $2 \times$, and $3 \times 0.01 G_0$ that are ascribed to one, two, and three molecules, respectively. (E and F) In the absence of molecules, no such steps or peaks are observed within the same conductance range, see [32].

Using monolayer film devices, it is also possible to conduct measurements on single molecules. A Scanning Tunneling Microscope (STM) tip is used as second electrode. Often films consisting of a matrix of spacer molecules plus the molecules to be measured are used. By using these smaller, insulating molecules (usually based on alkyl chains) as spacers, the molecules of interested are separated spatially from each other enhancing the probability to contact a single molecule with the STM tip. As di-thiol SAMs (with sulfur groups on both ends) are difficult to produce, the molecules can usually only be chemically bound to the substrate, the second contact then is a tunneling contact. In consequence, STM based single-molecule measurements always have strongly asymmetric coupling to the electrodes, which makes interpretation of the experimental data more complicated.

The first demonstration of a single-molecule measurement based on STM techniques was done by Bumm and Tour [33]. Here, longer molecules consisting of several benzene rings in a SAM with shorter, insulating molecules as spacers, were contacted using the STM tip. The molecules were covalently bound to the substrate via thiol groups, whereas the contact to the STM tip was a tunneling contact. Since then, many other STM based conductance measurements have been reported [23, 32, 34]. In 2003, Tao and coworkers

developed a method that allows the repeated formation of molecular junctions using a gold STM tip in fast succession [32]. The STM tip is moved into and out of contact with a gold substrate in a solution containing the sample molecules. When the tip is pulled out of contact, a stepwise decrease in the conduction is observed, (Fig. (1.5)). These steps are the usual conduction steps observed in metallic point contacts. When the tip is pulled out further, additional plateaus appear, corresponding to a resistance two orders of magnitude higher. By statistical analysis it was possible to attribute these steps to the measurement of a distinct number of molecules between the contacts.

1.2 Inelastic electron tunneling spectroscopy

IETS is an all electronic spectroscopy that has been extensively reviewed [35, 36]. By measuring currents and voltages across a metal-adsorbate-metal (M-A-M') device in a special way, one is able to extract vibrational and electronic spectroscopic information about the metals (magnons and phonons), the insulator, and the adsorbate. It has been successfully applied to problems in surface chemistry and catalysis, adhesion and corrosion, molecular vibrational and electronic spectroscopy. The motivation for tunneling studies is based on several unusual properties of the electron-molecule scattering process. Despite the complexity of the experimental setup, the molecule must be connected to two electrodes, there are some remarkable advantages (see [35]):

- Optically forbidden (IR and/or Raman) fundamental transitions may be observed. In addition, spin and dipole forbidden electronic transitions are also allowed .
- Overtone and combination bands are very weak or absent. Thus, virtually every band is due to a fundamental transition.
- Very small amounts of compound can provide a complete spectrum.
- IETS offers the opportunity of studying molecules in buried interfaces thereby providing unique insights into the effects on molecular states produced by intimate contact with metallic and insulating layers.
- IETS provides a high sensitivity method for studying chemisorption and catalysis.
- It is an all solid-state spectroscopy. In principle the sample and spectrometer could be built on a single chip. When this feature is combined with the further development of porous electrodes, IETS becomes uniquely situated for sensor applications.

The IETS is based on electron tunneling. By electron tunneling I mean the motion of electrons from one classically allowed region to another through a region where the electron is classically forbidden to exist (see Fig. (1.6)). The barrier region is one in which the potential energy, U , is greater than the total classical energy, E . If the particle moves from one allowed region to another, it must tunnel through the potential barrier. Of course,

there is no such prohibition in quantum mechanics. An electron of energy E impinging on the potential barrier from the left in Fig. (1.6) has an exponentially damped probability of penetrating the barrier a distance z . If U and E are both large (several electron volts) and d is very small (of the order of 1 nm), there is a finite probability of the incident electron emerging into the classically allowed region III.

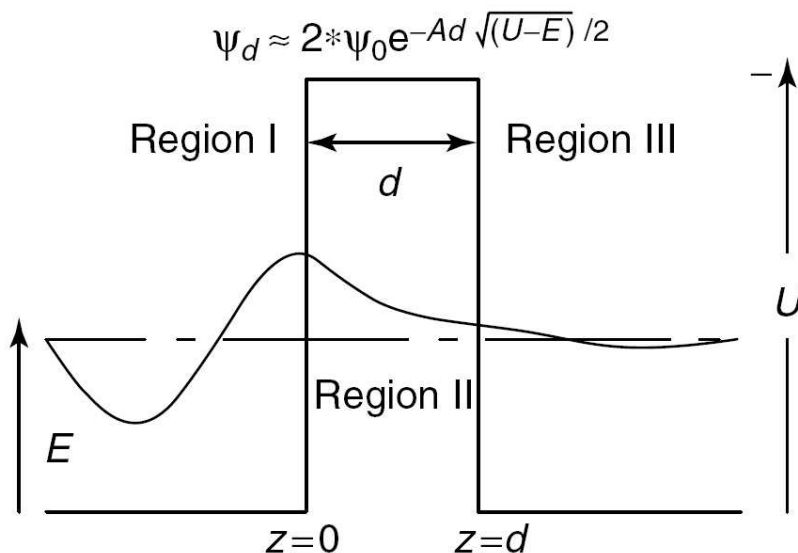


Figure 1.6: Schematic representation of the elastic tunneling process.

The tunneling can be divided as the sum of two fluxes: the first related to elastic tunneling when the electron flows from one contact to the other without any interaction with the barrier, the second is the inelastic tunneling when the electron undergoes an interaction with the degrees of freedom inside the barrier (like the modes of vibrations of the molecular region).

A schematic view of what happens for IETS is shown in Fig. (1.7, a). In the crude model, the free electron theory is used to represent the metals and the insulator plus adsorbate is treated as a vacuum space. The electron states are filled up to the Fermi energy, E_F , and the work function of the metal is given by ϕ . It is assumed that we are at very low temperature so that the occupation in the contacts follow a real step-like function. The hatched regions in Fig. (1.7, a) represents completely filled metal orbitals. The HOMO and LUMO of the molecular region are also shown in Fig. (1.7, a), as are a few schematic ground vibrational levels. The interaction between the top metal and the molecule can produce a shift in molecular energy levels and its level spacing as well as the vibrational spectrum. As the two metals and insulator are brought together, electrons flow via tunneling until the Fermi surfaces are matched. If the left-hand metal electrode is taken as the reference, the right-hand electrode develops a net charge, of sign and magnitude determined by the difference in work functions. Once the Fermi energies are matched, no net current flows and the approximate barrier height is $\phi \sim (\phi_M + \phi_{M'})/2$. In the case of metals with widely different

work functions there is an internal potential generated that can amount to millions of volts per centimeter.

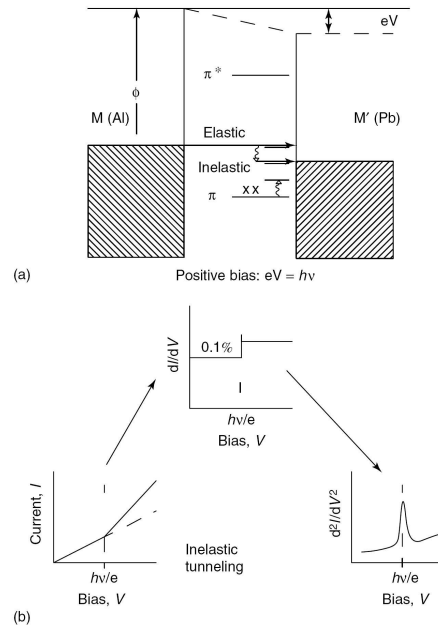


Figure 1.7: Energy diagram for an Al-Al₂O₃-anthracene-Pb tunnel diode showing elastic and inelastic tunneling processes. (a) The hatched regions represent the filled states of the top and bottom metal electrodes. The area in the center represents the anthracene coated alumina. The HOMO (π) and LUMO (π^*) orbital energies and a few vibrational levels are indicated. The case shown is where the bias energy (eV) is just sufficient to allow inelastic tunneling with excitation of the first vibrational level, $eV = hv$. Energy loss (equilibration) for the tunneling electron occurs through a cascade process in the M' electrode. (b) The I - V curve, conductance- V curve, and the IETS spectrum that would result from both elastic processes and the first inelastic channel as shown in the barrier diagram.

When a small bias is applied a tunneling current starts to flow. At low temperature the absorption of phonons is much smaller than the emission from the electrons which is the dominating process. Until the bias is smaller than the smallest vibrational frequency no scattering is allowed because after the emission of a phonon the electron will end up below the Fermi energy of the second electrode. This means that only the elastic current can pass. This elastic tunneling current is the ever-present source of the background signal with which all tunneling spectroscopists must deal. Since IETS depends on derivatives of I with respect to V (see Fig. (1.7, b)) it would first appear that the elastic current would have little effect on the IETS. Unfortunately, the number of electrons tunneling elastically is usually orders of magnitude larger than the number utilizing inelastic channels. Thus, relatively small deviations of the elastic current produce large background changes. This background is depicted as linear in Fig. (1.7, b), but can become nonlinear and even non-monotonic.

When the bias is large enough, in addition to elastic tunneling, there are other tunneling mechanisms which may contribute to the current: the inelastic current as shown in Fig. (1.7, b). The moving electronic charge interacts with the time-varying molecular vibrations to induce excitation of the molecule in the barrier with concomitant loss of energy by the electron. From an energetically point of view the applied voltage is less than $h\nu/e$, the inelastic channel is closed because the final states are already filled (Pauli principle). At $V = h\nu/e$ the inelastic channel opens. Further increases in V result in additional possible final states with an associated increase in current due to this channel. As is depicted in Fig. (1.7, b), there is a change in the slope in the I-V curve at $V = h\nu/e$. If one measures the conductance, dI/dV , the opening of the inelastic channel is signaled by a step. Plotting d^2I/dV^2 versus V produces a peak at $V = h\nu/e$. Both vibrational and electronic transitions may be observed as peaks in the d^2I/dV^2 versus V plots.

The width of the peaks in IETS depends upon the sharpness of the onset of the inelastic process, which in turn depends upon the thermal distribution of electron energies about E_F . Thus, the IETS line width depends on temperature and is about $3.5 \text{ cm}^{-1} \text{ K}^{-1}$. Because of this, vibrational IETS is most often performed below 5 K. Electronic transitions are usually much broader than vibrational transitions. In its simplest form, an IET spectrum is a plot of d^2I/dV^2 versus V . It turns out that using $(d^2I/dV^2)/(dI/dV)$ as the y-axis provides spectra having flatter baselines and is most appropriate for high bias work [37].

There are very few hard selection rules in IETS. Instead, there are some selection preferences (referred in literature as *propensity rules* [38]). In IETS we see some bands that appear in IR or Raman spectra and others that are optically forbidden. Thus, IETS is an excellent complementary vibrational spectroscopy for high symmetry molecules where many of the modes are optically forbidden.

In principle, the spectrum in IETS is usually assigned by comparison with IR, Raman, and HREELS results for monolayers of the molecule in question. However, the absence of simple selection rules means that IETS may exhibit markedly different spectra with characteristics that are difficult to predict. There have been several theoretical approaches developed to simulate IETS [39, 40, 41, 42, 43, 44, 45, 46], approaches with varying strengths and weaknesses. The theoretically most advanced ones have been applied to model systems [43] while many of the earlier ones made significant approximations in order to treat real molecules with ease.

Modeling Molecular Electronic Devices

The main aim of every theoretical transport model is of course the description of the flow of current in the device region, in our case focusing on the dissipation induced by electron-phonon interaction (vibronic coupling). In Chapter 1 some of the most popular experimental setups for molecular electronic devices were presented. The reason for that brief introduction was to show the kind of systems that must be simulated. Following those setups, in this second Chapter, a theoretical approach to model the device is discussed.

In the first part of this Chapter is shown how the device is partitioned in different regions. This partitioning is related to the way the bias drops through the entire device. First we have the proper molecular bridge connected to two leads, the leads are the interface between the molecular bridge and the bulk contacts. The contacts are bulk regions which act as two semi-infinite reservoirs of charges. The current flowing in the molecular bridge is a flux of charges going from one contact to the other. This flux is influenced by many aspects of the system under investigation. First of all, the electronic structure of the molecule and of the two leads, which is related to the geometry of the system and the material used to make the device. The interface between molecule and contacts should also define the charge transfer that occurs between the two also at zero bias and, eventually, the relaxation of the molecule when sandwiched between the two electrodes. Two other important aspects influence the total current: the bias applied, and the electron-phonon interaction which changes the distribution of electrons in the molecule and determine the power dissipated in the bridge.

In the second part of this Chapter is presented the Meir-Wingreen equation [47], for the calculation of the steady-state current including the effect of inelastic scattering. This general equation can be simplified to a complete elastic transport equation, the Landauer-Büttiker equation [48, 49], if the inelastic scattering interaction is neglected.

During this Chapter extensive use of the formalism called second quantization is made. It is a particular convenient formalism for transport problems. For the non expert reader I suggest, from the literature, a brief list of excellent sources about the topic [50, 51, 52].

2.1 The general problem of molecular conduction

All the experimental setups show very similar features: the presence of two contacts and a molecule, or a layer of molecules, which bridges them, sometimes also a gate is present. In Fig. (2.1) a schematic view of a typical molecular electronic device is shown.

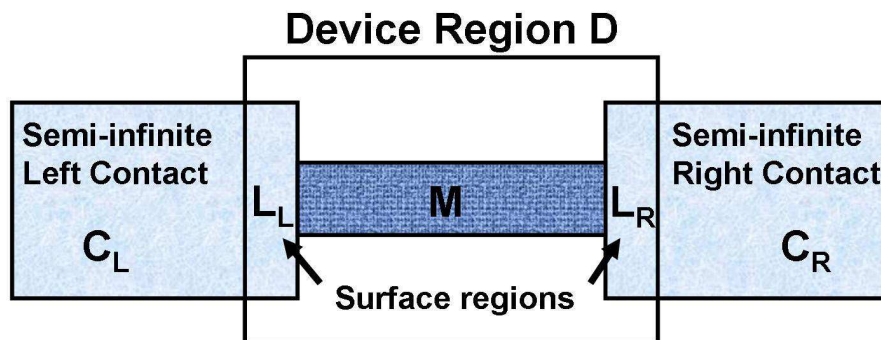


Figure 2.1: A schematic view of a typical molecular electronic device. In the picture different regions can be recognized: the molecular (M) and the surfaces or leads regions (L) which together form the device region (D). The two semi-infinite contacts (C_L and C_R) act as charge reservoirs.

To better simulate such devices, the entire system is usually split in different parts. For the simplest geometry, we need at least two electrodes, (C_L and C_R , but the formalism and the experiments can be generalized to a larger number of electrodes) and a device region (D). The contacts (C_L and C_R) represent two semi-infinite reservoirs of charge carriers. Electrons within the contacts are assumed to be in thermodynamic equilibrium and their electron distributions can be correctly described by means of two Fermi functions with a definite chemical potential (μ_L and μ_R), see Fig. (2.2). If no bias is applied the two chemical potentials are the same. The contacts are assumed to be perfect, defect-free crystalline structures, in the sense that they can always be constructed starting from a defined unit cell. Apart from this assumption, no constraint is imposed on the dimensionality, transverse size and transverse shape of them. They can be one-dimensional atomic chains, two-dimensional planar atomic strips or three-dimensional wires of arbitrary cross-section.

The device region (D) is obviously the most important part of the system. It is the region in which the main processes happen. It can be formed by every collection of atoms between the contacts. When a bias is applied the reservoirs are assumed to remain locally in thermodynamic equilibrium. This means that the only effect of the bias is to change the two chemical potentials that now have different values. All the voltage drop is instead in the device region, which is in non-equilibrium condition (see Fig. (2.2)). The main consequence of this is that both contacts try to shift the chemical potential of the device to its own level. The contact with the higher chemical potential tries to charge the device while the other contact tries to discharge it. The final effect is a net rate of electrons (or *holes*) flowing through the device from one contact to the other, that means a current. Due to the fact that the device region must include all the part of the system where there is a significant

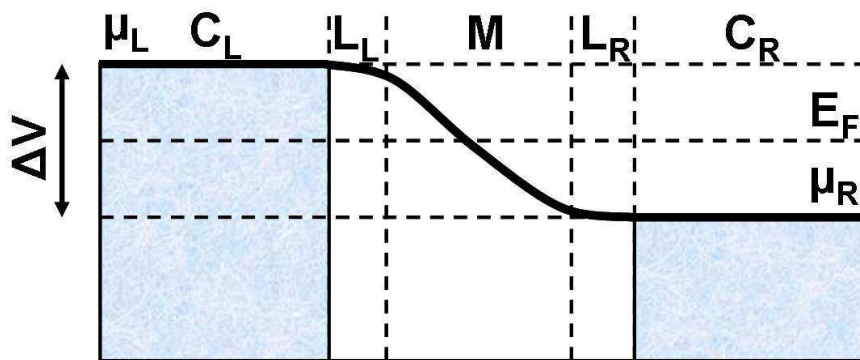


Figure 2.2: The voltage drop in the different regions when an external bias is applied. μ_L and μ_R are the two chemical potentials of the left and the right contact respectively. The drop of the bias occurs practically entirely in the molecular region and to a small extent in the lead regions also.

voltage drop it cannot reduce, usually, to only the molecular part. Some layers of the contacts must be included in the device, they are called leads. The system represented by the molecule plus the leads is often called extended molecule in the literature. The size of the leads depends mostly on the screening of the bias induced by the material of the contacts, so that different materials can result in different leads. The partitioning between device and contacts is an important issue, however, for many qualitative simulations we can effectively restrict the device region to the molecular bridge only, without large consequences.

The switching of the bias induces a current. After a first transient regime, where the current shows a clear time dependence, it reaches rapidly a steady-state. Despite the importance of the transient regime for the stability and the switching properties of an electronic device, the steady state regime is the only one investigated in the present work, also because is the one which is usually measured in experiments.

Theoretically the first challenge is to map the open boundary conditions represented by the contacts into the finite size device region. The problem is solved defining two potentials, called *self-energies*, which describe the incoming and outgoing of charges to and from the device. This simplification allows to reduce the dimensionality of our system. Instead of including the entire semi-infinite contacts in the simulated model I need just the device region and some chunks of the two contacts. From these chunks the self-energies can be computed (see Chapter 5 and Appendix B for a complete description of the evaluation of the self-energies). They are non local, non hermitian, energy dependent potentials. The non hermiticity is the fundamental property of these potentials. Including them in the Schrödinger equation we define for the device region a new set of eigenvalues and eigenstates. The eigenvalues are complex numbers, where the real part is the energy of the level while the imaginary part is the inverse of a lifetime. The lifetime takes into account the time spent by the charge in the device, before it is absorbed by the contacts.

The eigenstates represent a set of transmission states, connected through the self-energies to the external environment; they are called *scattering states*. Each of these scattering states is carrying a finite amount of current due to its occupancy. In case of molecular devices

these scattering states give a simple explanation of the strong non-linearity which is normally observed in current-voltage characteristics. When in fact one of these states enters in the energy window between the two chemical potentials of the contacts another channel for the current is switched on and more current can flow. The knowledge of scattering states completely covers the problem of describing quantum conductance in the case of elastic transport, that means when inelastic scattering processes are not relevant.

In case scattering processes (e.g. electron-phonon) are present the problem is complicated by the fact that emission or absorption of phonons can change the channel in which one charge propagates and scatters it into another channel. The calculation of scattering states can be achieved by several techniques, such as transfer matrix (TM) and Green's function (GF) approaches [53, 54]. Although the computational cost of the TM method is generally smaller with respect to the GF technique, the latter approach is more powerful. In fact it can be extended and generalized to a statistical Non-Equilibrium Green's Function (NEGF) theory [50, 55] accounting for the correct population of the states with the inclusion of scattering mechanisms (electron-electron, electron-phonon, etc). A more detailed treatment of the NEGF method is presented in Chapter 3.

2.2 The Hamiltonian of the system

The general Hamiltonian for the entire system must consider the presence of the device and the contacts regions and, also, of the phonons in the molecule which are connected to an external bath in thermodynamic equilibrium. The external bath of phonons represents the thermal vibrations of the contacts. With this in mind it is possible to write the Hamiltonian of the entire system, using second quantization formalism:

$$\hat{H} = \hat{H}_D + \hat{V}_{DC} + \hat{H}_C \quad (2.1)$$

where:

$$\hat{H}_D = \sum_{i=1}^N \varepsilon_i \hat{d}_i^\dagger \hat{d}_i + \sum_{\alpha} \omega_{\alpha} \hat{a}_{\alpha}^\dagger \hat{a}_{\alpha} + \sum_{i,j;\alpha} M_{ij}^{\alpha} \hat{Q}_{\alpha}^a \hat{d}_i^\dagger \hat{d}_j \quad (2.2)$$

$$\hat{H}_C = \sum_{k \in L,R} \varepsilon_k \hat{c}_k^\dagger \hat{c}_k + \sum_{\beta=L,R} \omega_{\beta} \hat{b}_{\beta}^\dagger \hat{b}_{\beta} \quad (2.3)$$

$$\hat{V}_{DC} = \sum_{i;k \in L,R} \left(V_{ki} \hat{c}_k^\dagger \hat{d}_i + V_{ki}^* \hat{d}_i^\dagger \hat{c}_k \right) + \sum_{\alpha;\beta=L,R} U_{\alpha\beta} \hat{Q}_{\alpha}^a \hat{Q}_{\beta}^b \quad (2.4)$$

Eqn. (2.1) is the sum of three terms: the contributions to the Hamiltonian of the device, \hat{H}_D , of the contacts, \hat{H}_C , and the coupling between the two, \hat{V}_{DC} . In Eqn. (2.2), Eqn. (2.3) and Eqn. (2.4), \hat{a} (\hat{a}^\dagger) and \hat{b} (\hat{b}^\dagger) are annihilation (creation) operators for the phonons in the device and in the external bath respectively. The \hat{d} (\hat{d}^\dagger) and \hat{c} (\hat{c}^\dagger) are similar operators for electrons in the device and in the contacts. The creation and annihilation operators satisfy

the usual commutation rules:

$$[\hat{a}_i, \hat{a}_j^\dagger] = \delta_{ij} \quad (2.5)$$

$$[\hat{c}_i, \hat{c}_j^\dagger]_+ = \delta_{ij} \quad (2.6)$$

where the first relation is for boson operators and the second, the anticommutation, is for fermion operators. Finally, Q_α^a and Q_β^b are vibration coordinate operators:

$$\hat{Q}_\alpha^a = \hat{a}_\alpha + \hat{a}_\alpha^\dagger \quad (2.7)$$

$$\hat{Q}_\beta^b = \hat{b}_\beta + \hat{b}_\beta^\dagger \quad (2.8)$$

In the equation ε_i is the energy state of the device central region, ω_α (ω_β) are the energies of phonons in (and out) of the device, M_{ij}^α is the electron-phonon coupling for the α^{th} mode of vibration, ε_k is the energy of one electron in the contacts, V_{ki} is the contact-device coupling and finally $U_{\alpha\beta}$ is the phonon-phonon coupling between phonon in the device and in the external bath. Eqn. (2.2) is the sum of three terms related to the electronic structure, the phonon population and the interaction between phonon and electrons in the device. Eqn. (2.3) is the same for the two contacts, but because the contacts are in equilibrium, there is no electron-phonon term here. Finally, the last equation, (2.4), describes the coupling between contacts and device (first term) and the coupling between phonons in the bath and in the device (second term).

The model is characterized by other parameters which are fundamental for the evaluation of the current. These quantities are:

$$\Gamma_i^{L,R} = 2\pi \sum_{ij;k \in L,R} |V_{ik}|^2 \delta(\varepsilon_i - \varepsilon_k) \quad (2.9)$$

it represents the molecule-contact coupling by its effect on the lifetime broadening on a molecular level i and,

$$\gamma_\alpha^{L,R} = \sum_{\alpha;\beta \in L,R} |U_{\alpha\beta}|^2 \delta(\omega_\alpha - \omega_\beta) \quad (2.10)$$

is similarly the lifetime broadening induced by the relaxation of phonons of the device in the external bath. The central quantity in the electron-phonon interaction is obviously the vibronic coupling M_{ij}^α .

In the formulation implemented in my code the last term of Eqn. (2.4) is neglected. The phonon population is assumed to be in perfect equilibrium with the environment. This means that all the $U_{\alpha\beta}$ coefficients are zero and that there is no relaxation of the phonons from the device region into the contacts. This approximation reduces the applicability of the code to low temperature simulations only, because relaxation processes are particularly important at higher temperature. Nevertheless many experiments in molecular electronics

are performed at liquid helium temperature (4.2 K); however, an extension of the formalism including electron-phonon relaxation has been implemented recently, see [56].

2.3 From the Hamiltonian to the current: Meir-Wingreen equation

Following the approach of Caroli *et al.* [57] it is possible to relate the Hamiltonian of Eqn. (2.1) to the current. From the continuity equation it is possible to define the current flowing through the left electrode:

$$I_L = -e\langle\dot{N}_L\rangle = -\frac{ie}{\hbar}\langle[\hat{H}, \hat{N}_L]\rangle \quad (2.11)$$

where \hat{H} is the Hamiltonian of the system and \hat{N}_L is the number operator for the device which couples with the left electrode only. It is defined as,

$$\hat{N}_L = \sum_k \hat{d}_k^\dagger \hat{d}_k \quad (2.12)$$

The only term in the Hamiltonian which does not commute with the number operator is the interaction term between the device and the left contact (first term in Eqn. (2.4)). After solving Eqn. (2.11) we get

$$I_L = \frac{2ie}{\hbar} \sum_{i,k \in L} \left(V_{ki} \langle \hat{c}_k^\dagger \hat{d}_i \rangle - V_{ki}^* \langle \hat{d}_i^\dagger \hat{c}_k \rangle \right) \quad (2.13)$$

where the factor 2 comes from the spin degeneracy. If we analyze in more details Eqn. (2.13) we find that the total current through the left interface is the difference between two fluxes: the outgoing, $\langle \hat{c}_k^\dagger \hat{d}_i \rangle$, and the incoming, $\langle \hat{d}_i^\dagger \hat{c}_k \rangle$, electrons. The direction of the flux of charges can be easily checked considering the kind of operators involved, i.e., for the incoming flux $\langle \hat{d}_i^\dagger \hat{c}_k \rangle$ we have that one electron is annihilated in the left contact, \hat{c}_k , and one is created in the device, \hat{d}_i^\dagger . We can reformulate Eqn. 2.13 and terms like $\langle \hat{d}_i^\dagger \hat{c}_k \rangle$ by introducing the so called *lesser* Green's function, which is a time dependent quantity, $G_{ik}^<(t, t')$ defined as

$$G_{ik}^<(t, t') = i \langle \hat{c}_k^\dagger \hat{d}_i \rangle e^{-i\frac{E}{\hbar}(t-t')} \quad (2.14)$$

The $G_{ik}^<$ depends only on the difference of t and t' because we are computing the steady-state current. We can define $t - t' = \tau$ and Fourier transform the function $G_{ik}^<$:

$$G_{ik}^<(\tau) = \int_{-\infty}^{+\infty} \frac{dE}{2\pi} G_{ik}^<(E) e^{i\frac{E}{\hbar}\tau}$$

$$G_{ik}^<(E) = \int_{-\infty}^{+\infty} d\tau G_{ik}^<(\tau) e^{-i\frac{E}{\hbar}\tau} \quad (2.15)$$

$$(2.16)$$

The $G_{ik}^<$, apart from a phase factor, represents the correlation, in energy or in time, between one electron in the state i of the device and another one in the state k of the left contact. The two fluxes of the current are related to these correlation functions as follows:

$$\langle \hat{c}_k^\dagger \hat{d}_i \rangle = -iG_{ik}^<(0) = -i \int_{-\infty}^{+\infty} \frac{dE}{2\pi} G_{ik}^<(E) \quad (2.17)$$

$$\langle \hat{d}_i^\dagger \hat{c}_k \rangle = -iG_{ki}^<(0) = -i \int_{-\infty}^{+\infty} \frac{dE}{2\pi} G_{ki}^<(E). \quad (2.18)$$

Substituting the latter relations in Eqn. (2.13) for the current we get,

$$I_L = \frac{2e}{\hbar} \sum_{i,k \in L} \int_{-\infty}^{\infty} \frac{dE}{2\pi} [V_{ki} G_{ik}^<(E) - V_{ki}^* G_{ki}^<(E)] \quad (2.19)$$

The latter formula permits to introduce the Green's function formalism in the transport calculations. The main drawback of Eqn. (2.19) is that the quantities $G_{ik}^<$ and $G_{ki}^<$ depend on operators which apply both to the device region, \hat{d}_i^\dagger and \hat{d}_i , and the left contact, \hat{c}_k and \hat{c}_k^\dagger . What would be more desirable for the calculation is the possibility to decompose the $G^<$ functions in combination of terms which depend on operators in only one part of the system. This can be done using the so called Dyson's equation. A rigorous derivation of the Dyson's equation is not given here, but in Chapter 3. In order to apply the Dyson's equation we must first define two new propagators, the *retarded* and *advanced* propagators, G^r and G^a :

$$G_{im}^r(\tau) = -i\theta(\tau) \langle [\hat{d}_i, \hat{d}_m^\dagger]_+ \rangle e^{-i\frac{E}{\hbar}\tau} \quad (2.20)$$

$$G_{im}^a(\tau) = i\theta(-\tau) \langle [\hat{d}_i, \hat{d}_m^\dagger]_+ \rangle e^{i\frac{E}{\hbar}\tau} \quad (2.21)$$

The retarded function represents a dynamic propagators of one particle from state i to state m , while the advanced propagator describes the propagation of a charge vacancy, or a *hole*, from state i to state m . The retarded, advanced and lesser Green's functions are related by

the following equations, see [57, 47]:

$$G_{ik}^<(E) = \sum_m V_{km}^* [G_{im}^r(E) g_{kk}^<(E) + G_{im}^<(E) g_{kk}^a(E)] \quad (2.22)$$

$$G_{ki}^<(E) = \sum_m V_{km} [g_{kk}^r(E) G_{mi}^<(E) + g_{kk}^<(E) G_{mi}^a(E)]. \quad (2.23)$$

where capital letters were used for propagators which operate on the device region only and small letters for propagators which operate on the left contact. In these last relations we can see that, apart for the V_{km} coefficient which couples both device and contact, all the propagators depend on only one part of the system. Inserting Eqs. (2.22) and (2.23) in the current expression and interchanging the indices m and i in the last term we obtain

$$I_L = \frac{2e}{\hbar} \sum_{i,m;k \in L} \int_{-\infty}^{\infty} \frac{dE}{2\pi} V_{ki} V_{km}^* [g_{kk}^< \{G_{im}^r - G_{im}^a\} + G_{im}^< \{g_{kk}^r - g_{kk}^a\}]. \quad (2.24)$$

Because the contacts are free of any interaction their Green's functions assume a very simple form:

$$g_{kk}^< = 2\pi i n_L \delta(E - \varepsilon_k) \quad (2.25)$$

where n_L is the Fermi distribution function of the left contact, and

$$g_{kk}^a - g_{kk}^r = 2\pi i \delta(E - \varepsilon_k). \quad (2.26)$$

It is possible to use a generalization of Γ_i^L (Eqn. (2.9)) to put all the reference about the contact-device interface in one function,

$$\Gamma_{mi}^L = 2\pi \sum_{k \in L} V_{ki} V_{km}^* \delta(E - \varepsilon_k) \quad (2.27)$$

Substituting Eqn. (2.25), Eqn. (2.26) and Eqn. (2.27) in the current formula we get,

$$I_L = \frac{2ie}{h} \int_{-\infty}^{+\infty} dE \sum_{i,m} \Gamma_{mi}^L [n_L (G_{im}^r - G_{im}^a) + G_{im}^<] \quad (2.28)$$

which in matrix notation becomes

$$I_L = \frac{2ie}{h} \int_{-\infty}^{+\infty} Tr[\Gamma_L n_L (\mathbf{G}^r - \mathbf{G}^a) + \Gamma_L \mathbf{G}^<] dE. \quad (2.29)$$

The total current is the difference between the charges entering through the left contact and leaving through the right one

$$I = \frac{1}{2} (I_L - I_R) \quad (2.30)$$

so we get finally for the current between the left and right junctions

$$I = \frac{ie}{h} \int_{-\infty}^{+\infty} Tr[(n_L \Gamma_L - n_R \Gamma_R)(\mathbf{G}^r - \mathbf{G}^a) + (\Gamma_L - \Gamma_R)\mathbf{G}^<]dE. \quad (2.31)$$

In a steady state the flux between the left junction must be equal in magnitude and just opposite in sign: $I_L = -I_R$. This means that the total current is just equal to the left current. Moreover, we can define two new quantities which represents the injection (extraction) of charges through the left contact

$$\Sigma_L^< = in_L \Gamma_L \quad (2.32)$$

$$\Sigma_L^> = -i(1 - n_L) \Gamma_L \quad (2.33)$$

Substituting the former in the current equation and using the identity (see Chapter 3) $\mathbf{G}^> - \mathbf{G}^< = \mathbf{G}^r - \mathbf{G}^a$, we get, after some manipulations, the Meir-Wingreen equation

$$I = \frac{2e}{h} \int_{-\infty}^{+\infty} Tr[\Sigma_L^< \mathbf{G}^> - \Sigma_L^> \mathbf{G}^<]dE. \quad (2.34)$$

Further simplifications can be done to the Meir-Wingreen equation if there is no scattering in the device region, in that case the formula of the current reduces to the famous Landauer-Büttiker equation. First of all, without scattering, we have the following, see [53],

$$\mathbf{G}^< = in_L \mathbf{G}^r \Gamma_L \mathbf{G}^a + in_R \mathbf{G}^r \Gamma_R \mathbf{G}^a \quad (2.35)$$

$$\mathbf{G}^r - \mathbf{G}^a = -i\mathbf{G}^r (\Gamma_L + \Gamma_R) \mathbf{G}^a \quad (2.36)$$

and substituting them in the Meir-Wingreen equation,

$$I = \frac{2e}{h} \int_{-\infty}^{+\infty} Tr[\Gamma_L \mathbf{G}^r \Gamma_R \mathbf{G}^a] (n_L - n_R) dE. \quad (2.37)$$

In the Landauer-Büttiker equation the current is split in two parts: a transmission factor which depends on the coupling with the contacts and the propagators and an occupation factor which depends on the distribution of electrons in the contacts only. In other words, in elastic transport the occupation is dominated by the contacts and the dynamics mostly by the device. In the inelastic case, described by Meir-Wingreen, the current is just the difference between two fluxes (in and out of the device region), where the occupation information and the dynamics information are strongly correlated due to the scattering.

2.4 Lifetimes of interest

The equation displayed in (2.34) is the basis of the non-equilibrium evaluation of the current. However, despite the Meir-Wingreen evaluates a steady state current, time has still a central role.

The Hamiltonian and the Meir-Wingreen formulas are in fact related to many parameters which are connected to the lifetime of all the processes involved in transport through scattering and some energy parameters. These lifetimes are usually very different in timescale and so the effect of one process on the full transport can change dramatically depending on the system under investigation. The final result is that the effect of electron-phonon interaction in molecular conduction can produce a large set of different behaviors observed experimentally.

The first important energy parameter is ΔE , the energy difference between the Fermi energy of the electrode and the closest molecular orbital (the highest occupied molecular orbital (HOMO) or the lowest unoccupied molecular orbital (LUMO)). The second parameter is Γ , the broadening of molecular orbital levels induced by the coupling with the contacts. If the device behaves like a molecular chain, there is another important value, the bandwidth V_B of the “conduction band” of the chain. Finally, the energy value $k_B T$ (where k_B is the Boltzmann constant and T is the absolute temperature) is quite important giving the thermal effects to the electronic and phonon populations.

All these energy parameters are related to some time constants which are fundamental for the transport. First of all there is the transmission time (\hbar/Γ_k) which is the time an electron in the state k spends in the device. Second, we have the relaxation time for phonons (\hbar/γ_α) which is the time needed by a phonon in the device to relax in the thermal bath into the contacts. This contribution is neglected due to the fact that the system is constrained to be always in thermal equilibrium with the bath. Finally \hbar/V_B is the lifetime spent by an electron in one molecular site if the device behaves like a wire.

Another important time scale, and that is less obvious, is the so called dephasing time (τ) which describes the time needed by the modes of vibration to destroy completely the phase coherence of the electron. When $\tau \ll \hbar/\Gamma_k$ then the transport reduces to a collection of hopping from one site of the device to the other. On the other hand if the dephasing does not occur, the transport can be treated using elastic transport and adding the electron-phonon contribution as a perturbation.

The relation between all these energy parameters and time scales defines which model is more appropriate for the system under investigation. The comparison between dephasing time and transmission time decides if the transport is fundamentally an elastic coherent tunneling or it is more a collection of jumps. When either ΔE or Γ_k are much larger compared to the electron-phonon interaction the transport becomes fundamentally elastic (especially if $\Delta E \approx 0$, that means at resonance). In an intermediate case we can use a perturbation correction to introduce the inelastic part of the current induced by the device vibrations. If instead Γ_k is small (weak coupling regime) the device behaves fundamentally as a dot and also if the electron-phonon coupling is small there is time for the formation of polaron-like states inside the device. The transmission is basically a hopping between the device and the two contacts assisted by vibrations. These different cases can be easily

tested by a comparison between the different quantities,

$$\left| \frac{M^\alpha}{\sqrt{(\Delta E)^2 + (\Gamma_k/2)^2}} \right| = \Delta. \quad (2.38)$$

The two limits ($\Delta \ll 1$ and $\Delta \gg 1$) are called strong and weak electron-molecule coupling regime respectively. In the present work we investigate the first case only.

The discussion of course is not confined to only these parameters, that anyway remain the most important. Other aspects can play a fundamental role. One for all is the possibility that strong many body effects can change the picture. When in fact a charge enters the device there is a distortion. If the transmission time is long enough and the distortion is localized, this creates a quasi-particle state, a polaron, which propagates in the system. The different nature of the polaron, basically an electron dressed by a collection of phonons, can change dramatically the conduction. Moreover, the change induced in the device can change the time and energy scale previously described changing eventually the type of conduction.

Non-Equilibrium Green's Functions

The main result of Chapter 2 is the Meir-Wingreen equation (Eqn. (2.34)), which generalizes the Landauer-Büttiker equation for elastic transport. The Landauer formula is in fact contained in the Meir-Wingreen as a special case, when scattering processes are neglected. We can expect that Landauer is a good approximation of transport for short devices, strongly bound to the contacts, at low temperature. In these conditions, in fact, the probability that scattering processes occur is reduced. However, also in that case, inelastic scattering can play an important role. In Chapter 2, for the evaluation of the current, a collection of propagators were introduced, related by a set of so called Dyson's equations. These propagators are related to the statistical population of electrons in the system like the lesser ($G^<(E)$) Green's functions or to their dynamics like retarded ($G^r(E)$) and advanced ($G^a(E)$) propagators.

Their evaluation requires the Non Equilibrium Green's Function (NEGF) formalism. NEGF methods represent the state of the art for molecular electronics transport calculations. This is based on two facts: first, the open boundary conditions of the problem (the connection between the device and the semi-infinite contacts) can be easily handled in the calculations. Second, scattering processes can be included in the formalism following a general and systematic way based on a perturbation expansion of the Green's functions. The NEGF formalism relies on the works of Kadanoff, Baym and Keldysh [55, 58] mainly.

Many body calculations with NEGF are often done for simulating the behavior of systems at zero temperature. Of course, real experiments are never performed at zero temperature, although, in molecular electronics, many of them are often at low temperature. However, many quantities are not very sensitive to temperature and the effect of the latter can be included as a perturbation to a full zero temperature approach. Furthermore, the zero temperature property of a system is an important conceptual quantity, the ground state of an interacting system. A system is often described as its ground state plus its excitations, and the ground state may be deduced from a zero temperature calculation.

The starting point of every Green's function calculation is the Hamiltonian of the problem \hat{H} . It is presumed that one is trying to solve a Hamiltonian which cannot be solved

exactly. The usual approach is to set

$$\hat{H} = \hat{H}_0 + \hat{V} \quad (3.1)$$

where \hat{H}_0 is a Hamiltonian which may be solved exactly. In our approach the \hat{H}_0 can be split in the sum of three contributions:

$$\hat{H}_0 = \hat{H}'_0 + \hat{\Sigma}_L + \hat{\Sigma}_R \quad (3.2)$$

Where the first term is a single particle Hamiltonian for the device region represented by a Density Functional Theory (DFT) Hamiltonian, the description of the particular DFT method applied in our case is the topic of Chapter 4. The other two terms ($\hat{\Sigma}_{L,R}$) are the contributions from the open boundary conditions (the way of computing them is described in Chapter 5 and Appendix B). The last term \hat{V} represents all the remaining parts of \hat{H} , in our case the effects of the electron-phonon interaction.

3.1 Three representations

In this brief paragraph the three most common representations for operators and wave functions are presented. They are the Schrödinger, the Heisenberg and the interaction representation. The paragraph is just a short refresh, for more details the reader is referred to other books which fully treat the topic [52, 51]. All the operators are marked by a hat symbol (Schrödinger and Heisenberg representations), except interaction representation for which a tilde is used. From now and through all this work, apart from a few sections, atomic units will be used for which $\hbar = m_e = e = 1$ (see Appendix A).

3.1.1 Schrödinger representation

Elementary quantum mechanics is usually presented in Schrödinger representation, which is based on the formula (in atomic units):

$$i \frac{\partial \psi(t)}{\partial t} = \hat{H} \psi(t) \quad (3.3)$$

which has the formal operator solution:

$$\psi(t) = e^{-i\hat{H}t} \psi(0) \quad (3.4)$$

The use of this formula requires two assumptions:

1. The wave functions $\psi(t)$ are time dependent, even if this time dependence is a simple factor of $\exp(-iEt)$.
 2. Operators, such as the Hamiltonian \hat{H} , are independent of time.
-

3.1.2 Heisenberg representation

It is possible to solve quantum mechanical problems in another way which gives exactly the same answers. The Heisenberg representation has the following properties:

1. The wave functions are independent of time.
2. The operators are time dependent, and this dependence is given by,

$$\hat{O}(t) = e^{i\hat{H}t} \hat{O}(0) e^{-i\hat{H}t} \quad (3.5)$$

or, equivalently, one is trying to solve the equation of motion which is derived from a time derivative:

$$i \frac{\partial \hat{O}(t)}{\partial t} = [\hat{O}(t), \hat{H}]. \quad (3.6)$$

3.1.3 Interaction representation

The interaction representation is the third way of recasting all quantum mechanics. Here both the wave functions and the operators are time dependent. The Hamiltonian is separated in two parts,

$$\hat{H} = \hat{H}_0 + \hat{V} \quad (3.7)$$

where \hat{H}_0 is the unperturbed (easy) part, while the \hat{V} contains the interactions. In interaction representation,

1. Operators have a time dependence

$$\tilde{O}(t) = e^{i\hat{H}_0 t} \hat{O} e^{-i\hat{H}_0 t}. \quad (3.8)$$

2. Wave functions, $\tilde{\psi}$ have a time dependence

$$\tilde{\psi}(t) = e^{i\hat{H}_0 t} e^{-i\hat{H}t} \psi(0) = e^{-i\hat{V}t} \psi(0) = \hat{U}(t) \psi(0). \quad (3.9)$$

It is assumed that $[\hat{H}_0, \hat{V}] \neq 0$. The main result of this division is that the time dependence of the wave functions is related to the \hat{V} only, the complicate part, while all the operators depend on the unperturbed \hat{H}_0 . It is important to note that \hat{H}_0 is the same in Schrödinger and interaction representations.

The operator $\hat{U}(t)$, in Eqn. (3.9), reduces to unity for $t = 0$. It can be represented as a series expanding the exponential operators. We define first an operator \hat{T} called time-ordering operator particular useful in this case:

$$\hat{T}[\tilde{A}(t_1)\tilde{B}(t_2)] = \theta(t_1 - t_2)\tilde{A}(t_1)\tilde{B}(t_2) \pm \theta(t_2 - t_1)\tilde{B}(t_2)\tilde{A}(t_1) \quad (3.10)$$

where θ is the usual step function and the upper (lower) sign is for Boson (Fermion) operators. The function of \hat{T} is to time order the operators following their statistic (symmetric or antisymmetric). The operator \hat{U} can be expanded as

$$\hat{U}(t) = 1 + \sum_{n=1}^{\infty} \frac{(-i)^n}{n!} \int_0^t dt_1 \int_0^{t_1} dt_2 \dots \int_0^{t_{n-1}} dt_n \hat{T}[\tilde{V}(t_1)\tilde{V}(t_2)\dots\tilde{V}(t_n)] \quad (3.11)$$

$$\hat{U}(t) = \hat{T} \exp \left[-i \int_0^t dt_1 \tilde{V}(t_1) \right] \quad (3.12)$$

where the last form is a short way to represent the infinite series.

3.2 S-Matrix

We define a new operator called *S*-Matrix, $\hat{S}(t, t')$, which propagates the wave function $\tilde{\psi}(t')$ in time:

$$\tilde{\psi}(t) = \hat{S}(t, t') \tilde{\psi}(t') = \hat{S}(t, t') \hat{U}(t') \tilde{\psi}(0). \quad (3.13)$$

This leads to the conclusion that the operator $\hat{S}(t, t')$ has the following formula:

$$\hat{S}(t, t') = \hat{U}(t) \hat{U}^\dagger(t') \quad (3.14)$$

From the previous section and Eqn. (3.14) we can define a list of properties for the \hat{S} operator:

1. $\hat{S}(t, t) = 1$
2. $\hat{S}^\dagger(t, t') = \hat{S}(t', t)$
3. $\hat{S}(t, t') \hat{S}(t', t'') = \hat{S}(t, t'')$

Furthermore, from the properties of the $\hat{U}(t)$ operator it is possible to define a simple exponential form for the \hat{S} operator, similar to the expansion for $\hat{U}(t)$:

$$\hat{S}(t, t') = \hat{T} \exp \left[-i \int_{t'}^t dt_1 \tilde{V}(t_1) \right] \quad (3.15)$$

The wave function $\tilde{\psi}(0) \equiv \psi(0)$ is equivalent in both interaction and Heisenberg form and it represents the ground state at time zero. The main problem of this formulation is that we do not know this function because we cannot solve the exact Hamiltonian \hat{H} , even for its lowest eigenvalue and eigenvector. In order to overcome this problem we can try to connect the exact ground state of \hat{H} with the ground state of \hat{H}_0 , ϕ_0 . The relationship between the

two ground states $\tilde{\psi}(0)$ and ϕ_0 at zero temperature was established by Gell-Mann and Low [59]:

$$\tilde{\psi}(0) = \hat{S}(0, -\infty)\phi_0 \quad (3.16)$$

Thus we are really asserting that $\tilde{\psi}(t)$ is equal to ϕ_0 for $(t \rightarrow -\infty)$. The traditional argument is that one starts in the dim past with a wave function ϕ_0 which does not contain the effects of the interaction \tilde{V} . The operator \hat{S} brings this wave function adiabatically up to the present $t = 0$. The wave function $\tilde{\psi}(t)$ for $(t \rightarrow +\infty)$ is related to the non interacting ground state by just an arbitrary phase factor $\exp(iL)$:

$$\tilde{\psi}(\infty) = \hat{S}(\infty, -\infty)\phi_0 = e^{iL}\phi_0. \quad (3.17)$$

3.3 Equilibrium Green's functions

In this work we are interested in the propagation of two particles only: electrons and phonons. So we will focus our attention to the Green's functions for them. They represent the two typical cases (Fermionic and Bosonic particles) of propagators because the basic method used for computing them can be applied, more or less, for all other particles or excitations. At zero temperature and for steady state (important for the time dependence) the electron Green's function is defined as follows:

$$G(\lambda, t - t') = -i\langle |\hat{T}[\hat{c}_\lambda(t)\hat{c}_\lambda^\dagger(t')]| \rangle \quad (3.18)$$

where λ is the set of quantum numbers for the problem of interest. The \hat{c} (\hat{c}^\dagger) are the usual annihilation (creation) operators.

At zero temperature the state $|\rangle$ must be the ground state. If we have chosen the Hamiltonian of the problem to be \hat{H} , then $|\rangle$ is the ground state of \hat{H} . The problem arises because the exact ground state of \hat{H} is not known. The ground state $|\rangle$ is independent of time and the creation and annihilation operators are in Heisenberg representation.

For $t > t'$ we have, using the \hat{T} operator:

$$G(\lambda, t > t') = -i\langle |\hat{c}_\lambda(t)\hat{c}_\lambda^\dagger(t')| \rangle \quad (3.19)$$

Here one takes the real ground state, and at a time t' one creates an excitation λ . At a later time t one destroys the same excitation. If λ is an eigenstate of \hat{H} then this state would propagate with a simple exponential time dependence:

$$G(\lambda, t > t') = -ie^{-i(t-t')(\epsilon_\lambda - \epsilon_0)} \quad (3.20)$$

For the other time arrangement, $t < t'$, we have that, on the contrary, a particle is *removed* from the system. So the Green's function describes the propagation of a *hole*:

$$G(\lambda, t < t') = i\langle |\hat{c}_\lambda^\dagger(t)\hat{c}_\lambda(t')| \rangle \quad (3.21)$$

So for $t > t'$ the Green's function is related to the retarded Green's function and for $t < t'$ to the advanced propagator.

The problem in evaluating the Green's function arises because both the ground state and the operators depend on the full Hamiltonian. The idea is to isolate the effect of the \hat{V} operator, so to say of the interaction part. This can be done switching into the interaction representation. Substituting Eqn. (3.16) in the Green's function equation and after some manipulation, we get the following:

$$G(\lambda, t - t') = \frac{-i \langle \phi_0 | \hat{T} [\tilde{c}_\lambda(t) \tilde{c}_\lambda^\dagger(t') \hat{S}(\infty, -\infty)] | \phi_0 \rangle}{\langle \phi_0 | \hat{S}(\infty, -\infty) | \phi_0 \rangle} \quad (3.22)$$

The advantage of this representation is that now all the information about the interaction is in the \hat{S} operator. On the other hand the creation and annihilation operators and the ground state are the not-interacting ones and do not contain any information about \tilde{V} . The \hat{T} operator automatically handle the right sorting of all the operators between the square brackets splitting the S -matrix in the proper way, following the properties of the \hat{S} operator enlisted in the previous section.

A Green's function can also be defined for the special case where the interactions $\tilde{V} = 0$ and hence the \hat{S} -matrix is unity. This Green's function plays a special role in the formalism, and we designate it by G_0 :

$$G_0(\lambda, t - t') = -i \langle \phi_0 | \hat{T} [\tilde{c}_\lambda(t) \tilde{c}_\lambda^\dagger(t')] | \phi_0 \rangle \quad (3.23)$$

G_0 is often called the unperturbed Green's function.

3.4 Wick's theorem

The Green's function is evaluated by expanding the S -matrix in a series (Eqn. 3.15) such as:

$$G(\lambda, t - t') = \sum_{n=0}^{\infty} \frac{(-i)^{n+1}}{n!} \int_{-\infty}^{+\infty} dt_1 \dots \int_{-\infty}^{+\infty} dt_n \frac{\langle \phi_0 | \hat{T} [\tilde{c}_\lambda(t) \tilde{V}(t_1) \tilde{V}(t_2) \dots \tilde{V}(t_n) \tilde{c}_\lambda^\dagger(t')] | \phi_0 \rangle}{\langle \phi_0 | \hat{S}(\infty, -\infty) | \phi_0 \rangle} \quad (3.24)$$

Let us, for the moment, ignore the denominator. We are more interested how evaluate time-ordered brackets like:

$$\langle \phi_0 | \hat{T} [\tilde{c}_\lambda(t) \tilde{V}(t_1) \tilde{V}(t_2) \dots \tilde{V}(t_n) \tilde{c}_\lambda^\dagger(t')] | \phi_0 \rangle \quad (3.25)$$

Our interaction is represented by the electron-phonon operator like the last term in Eqn. (2.2) in Chapter 2. This means that our brackets contain simultaneously operators for phonons (\tilde{Q}_α) and for electrons ($\tilde{c}_\lambda, \tilde{c}_\lambda^\dagger$). This is not a problem, it is possible to separate them

because they commute. Taking, for example, a term like the following,

$$\langle \phi_0 | \hat{T} [\tilde{c}_\lambda(t) \tilde{c}_{\lambda_1}^\dagger(t_1) \tilde{Q}_\alpha(t_1) \tilde{c}_{\lambda_2}(t_2) \tilde{c}_{\lambda_3}^\dagger(t_3) \tilde{Q}_\beta(t_2)] | \phi_0 \rangle \quad (3.26)$$

It can be separated as a product of terms which contain only operators of one type:

$$\langle \phi_0 | \hat{T} [\tilde{c}_\lambda(t) \tilde{c}_{\lambda_1}^\dagger(t_1) \tilde{c}_{\lambda_2}(t_2) \tilde{c}_{\lambda_3}^\dagger(t_3)] | \phi_0 \rangle \langle \phi_0 | \hat{T} [\tilde{Q}_\alpha(t_1) \tilde{Q}_\beta(t_2)] | \phi_0 \rangle \quad (3.27)$$

In the rest of the paragraph the terms for electron operators are the only ones considered due to the fact that the brackets with phonon operators behave exactly in the same manner except for the effect of the \hat{T} operator (see Eqn. (3.10)).

In the electron factor of the time ordered bracket there are two creation and two annihilation operators. It is rather complicate to evaluate this bracket. In order to solve the problem we can notice at first that all brackets like Eqn. (3.27) always contain the same number of creation and annihilation operators. Thus one is always trying to evaluate the product of n creation operators and n annihilation operators averaged by the non interacting ground state $|\phi_0\rangle$. The effect of a creation operator $c_{\lambda_p}^\dagger(t)$ is to put an electron into the state λ_p . In order to bring back the system into the non interacting ground state one of the annihilation operators $c_{\lambda_p}(t)$ must destroy the state λ_p before the bra $\langle \phi_0 |$. For example, the four operator term discussed before equals zero unless $\lambda = \lambda_1$ and $\lambda_2 = \lambda_3$ or unless $\lambda = \lambda_3$ and $\lambda_1 = \lambda_2$. Another important help comes from *Wick's theorem*. It states that a time-ordered product of operators can be split in a sum of products of brackets which contain only a pair of operators (pairing). Of all the possible arrangements in pairings only few are not zero. Applying the theorem to the bracket in Eqn. (3.27) we obtain the following,

$$\begin{aligned} & \langle \phi_0 | \hat{T} [\tilde{c}_\lambda(t) \tilde{c}_{\lambda_1}^\dagger(t_1) \tilde{Q}_\alpha(t_1) \tilde{c}_{\lambda_2}(t_2) \tilde{c}_{\lambda_3}^\dagger(t_3) \tilde{Q}_\beta(t_2)] | \phi_0 \rangle = \\ & = \delta_{\lambda \lambda_1} \delta_{\lambda_2 \lambda_3} \delta_{\alpha \beta} \langle \phi_0 | \hat{T} [\tilde{c}_\lambda(t) \tilde{c}_{\lambda_1}^\dagger(t_1)] | \phi_0 \rangle \langle \phi_0 | \hat{T} [\tilde{c}_{\lambda_2}(t_2) \tilde{c}_{\lambda_3}^\dagger(t_3)] | \phi_0 \rangle \times \\ & \times \langle \phi_0 | \hat{T} [\tilde{Q}_\alpha(t_1) \tilde{Q}_\beta(t_2)] | \phi_0 \rangle - \delta_{\lambda \lambda_3} \delta_{\lambda_2 \lambda_1} \delta_{\alpha \beta} \langle \phi_0 | \hat{T} [\tilde{c}_\lambda(t) \tilde{c}_{\lambda_3}^\dagger(t_3)] | \phi_0 \rangle \times \\ & \times \langle \phi_0 | \hat{T} [\tilde{c}_{\lambda_2}(t_2) \tilde{c}_{\lambda_1}^\dagger(t_1)] | \phi_0 \rangle \langle \phi_0 | \hat{T} [\tilde{Q}_\alpha(t_1) \tilde{Q}_\beta(t_2)] | \phi_0 \rangle \end{aligned} \quad (3.28)$$

Note that there is a time-ordering operator \hat{T} in each pairing bracket. For 3 creation and annihilation operators there are six possible pairings; for n operators there are $n!$ possible pairings.

A few simple rules should be kept in mind when making these pairings. The first is that a sign change occurs (only for Fermion operators) each time the position of two neighboring operators are interchanged.

The second rule is a method of treating the “time ordering” of two operators which occur at the same time, such as

$$\langle \phi_0 | \hat{T} [\tilde{c}_\lambda^\dagger(t) \tilde{c}_{\lambda_1}(t)] | \phi_0 \rangle \quad (3.29)$$

In these cases the annihilation operator always goes to the right,

$$= \delta_{\lambda\lambda_1} \langle \phi_0 | \tilde{c}_\lambda^\dagger(t) \tilde{c}_{\lambda_1}(t) | \phi_0 \rangle = \delta_{\lambda\lambda_1} n_F \quad (3.30)$$

where n_F is just the average occupation probability for electrons the λ state and it is independent of time. When two electron operators have different time arguments in a pairing, we put the creation operator to the right:

$$\langle \phi_0 | \hat{T} [\tilde{c}_\lambda^\dagger(t) \tilde{c}_{\lambda_1}(t_1)] | \phi_0 \rangle = \delta_{\lambda\lambda_1} \langle \phi_0 | \hat{T} [\tilde{c}_\lambda(t) \tilde{c}_{\lambda_1}^\dagger(t_1)] | \phi_0 \rangle \quad (3.31)$$

This term can be immediately identified as the unperturbed Green's function $iG_0(\lambda, t - t_1)$. Our previous examples (Eqn. (3.27)) can also be written in terms of Green's functions:

$$\begin{aligned} & \langle \phi_0 | \hat{T} [\tilde{c}_\lambda(t) \tilde{c}_{\lambda_1}^\dagger(t_1) \tilde{Q}_\alpha(t_1) \tilde{c}_{\lambda_2}(t_2) \tilde{c}_{\lambda_3}^\dagger(t_3) \tilde{Q}_\beta(t_2)] | \phi_0 \rangle \\ &= \delta_{\lambda\lambda_1} \delta_{\lambda_2\lambda_3} \delta_{\alpha\beta} iG_0(\lambda, t - t_1) iG_0(\lambda_2, t_2 - t_3) D_0^\alpha(t_1 - t_2) + \\ &- \delta_{\lambda\lambda_3} \delta_{\lambda_2\lambda_1} \delta_{\alpha\beta} iG_0(\lambda, t - t_3) iG_0(\lambda_2, t_2 - t_1) D_0^\alpha(t_1 - t_2) \end{aligned} \quad (3.32)$$

where D_0 is the analogous of the unperturbed propagator for phonons. In summary, *Wick's theorem* tells us that a time-ordering bracket may be evaluated by expanding it into all possible pairings and that each of these pairings will be an unperturbed propagators or a number operator n_F . In this way we can rewrite all the terms in the perturbation expansion of G as terms which depend only on the unperturbed propagators and equilibrium occupation probabilities.

3.5 Feynman's diagrams

Feynman introduced the idea of representing the kind of terms in Eqn. (3.32) by diagrams. These diagrams, are extremely useful for providing an insight into the physical process which these terms represent. They can be drawn both for the Green's function depending on time $G(\lambda, t)$ as well as for functions which are Fourier-transformed and depend on energy $G(\lambda, E)$.

The diagrams in the time space are drawn by representing the electron Green's function G_0 by a solid line which goes from t' to t , as shown in Fig. (3.1). An arrow is often included to represent the time direction. The phonon Green's function D_0^α is represented by a wiggly line. Usually double lines are used to represent the full propagators and single lines for unperturbed propagators. The phonon propagator have not a directional arrow because the \tilde{Q}_α operator for phonons is a linear combination of both annihilation and creation operators. This mean that a phonon propagator represents simultaneously an emission (forward arrow) and an absorption (backward arrow). The factor n_F is represented as a closed loop in time.

By using these pictorial elements, we can construct the diagrams for all the terms like

$$\begin{array}{c}
 \begin{array}{ccc}
 \xrightarrow[t']{\lambda} & \xrightarrow[t]{\lambda} & = G_0(\lambda; t - t') \\
 \text{---} & \text{---} & \\
 \end{array} \\
 \\
 \begin{array}{ccc}
 \text{---} & \text{---} & = D_0^\alpha(t - t') \\
 \text{---} & \text{---} & \\
 \end{array} \\
 \\
 \begin{array}{ccc}
 \text{---} & \text{---} & = n_F \\
 \text{---} & \text{---} & \\
 \end{array} \\
 \text{t } \lambda
 \end{array}$$

Figure 3.1: Diagrams for the three basic quantities: the unperturbed propagator for electrons (solid line) and for phonons (wiggly line) and the closed loop for the electron distribution n_F (Fermi function).

Eqn. (3.32) in our expansion of the full propagators (Eqn. (3.24)). For example, for the second order term, expanded with *Wick's theorem*, we get six contributions. These six terms are shown in Fig. (3.2) in their diagram representations.

In Fig. (3.2) diagrams like (c), (d), and (e) are usually zero. In fact in solid state of physics, for periodic systems, such kind of contributions represent a translation of the crystal or a permanent strain, and neither of these is meant to be in Hamiltonian. Despite that for molecular electronics, for which the region with electron-phonon interaction is only the device region and the system is not invariant after a translation, terms like those give a non vanishing contribution (see [60]). However, the two terms of primary interest remain (a) and (b). They look alike except for the labeling of the integration variables so they give the same contribution.

Finally the terms (d) and (f) show an interesting characteristic: the diagrams are formed by two distinct parts, they are *disconnected diagrams*. There is a relevant theorem, called *Linked Cluster Theorem*, which states that the denominator of the formula of the Green's function, in Eqn. (3.22), $\langle \phi_0 | S(t, t') | \phi_0 \rangle$, cancels with all the disconnected contribution in the numerator. This means that of all the diagrams we must take care of only those terms which produce connected diagrams. This is an important simplification of the Green's function expansion: not only it reduces the number of terms we must evaluate for every order, but also delete some of the most problematic terms from the series, in fact the disconnected diagrams are often affected by upsetting divergencies.

The evaluation of diagrams is really useful and very simple, much simpler than taking care of the analytic counterpart. Moreover there is a dual relationship between all the non zero pairings of terms in the series of the full propagator and the diagrams set. In principle

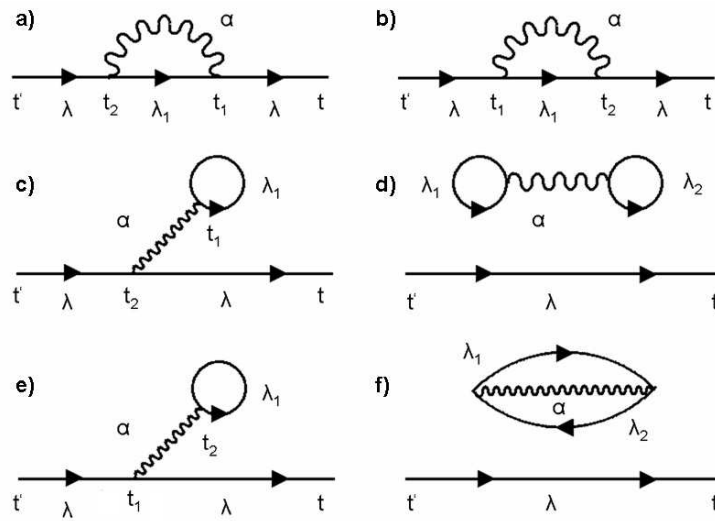


Figure 3.2: The six non null contributions for the second order expansion of the full propagator, in diagram form.

to evaluate the Green's function one should expand the S -matrix, decide which terms are connected and which are zero, and finally obtain the steady state Green's function by a Fourier transform of the sum of the relevant diagrams. But this laborious procedure can be avoided because the diagrams can be written down directly by following few simple rules. These rules are enlisted here for a n order diagram:

1. Draw n wiggly parallel lines and two external dots;
2. Join all wiggly lines and external dots with solid lines and define on these solid lines a direction with an arrow. Join them in all linked distinct topological way;
3. For every wiggly line: from each vertex point one solid line must enter and one must leave;
4. The external dots are connected to only one solid line; for one of the dot it must be an entering line and for the other a leaving line.

Once we have all the distinct linked diagrams they can be translated in analytic form with another simple set of rules:

1. If there are many modes of vibration the diagram must be preceded by a sum over all the modes for every wiggly line;
2. For each solid line, introduce an electron free propagator, G_0 ;
3. For each wiggly line insert a free phonon propagator, D_0^α and multiply for the proper electron-phonon coupling $M_{\lambda\lambda_1}^\alpha$ for every vertex of the wiggly line;

4. Conserve energy and quantum numbers at each vertex. Thus both electron lines and phonon lines have their variables labeled to conform with this rule.
5. Sum (or integrate) over internal degrees of freedom: quantum number, energy, and so on. All labels are internal except the two connected to the fixed external dots;
6. Finally, multiply the result by the factor:

$$P = \frac{(i)^m}{(2\pi)^{4m}} (-1)^F (2S + 1)^F \quad (3.33)$$

where F is the number of closed fermion loops and S is the spin index (usually for electrons $(2S + 1) = 2$). The index m is chosen as follows:

- For electron diagrams, m is the number of internal phonon wiggly lines.
- For phonon diagrams, m is one-half the number of vertices.

3.6 Dyson's equation

Up to now the formalism shows how to describe the full many-body Green's function in a series of terms (via the *Wick's theorem*) which depend on unperturbed propagators only. The zero order Green's functions are supposed to be known exactly because they depend on the \hat{H}_0 part of the Hamiltonian.

Moreover the technique of diagrams, introduced in the previous section, permits to simplify dramatically the evaluation of the series. The diagrams in fact can be drawn following very simple rules and represent a straightforward picture to understand the kind of contribution that every term gives to the final sum in a physical sense. On top of that from the connectivity of the diagrams we can see immediately which diagrams give a final contribution to the sum and which instead cancel with the denominator (*Linked Cluster Theorem*). It is possible now to reformulate the entire many body Green's function in a very nice formula called Dyson's equation. The presentation of the Dyson's equation and of the so called self-energy in the present work is not rigorous and I refer the interested reader to other books [50, 51, 52, 53].

First of all, from the drawing rules for diagrams, we know that every diagram has a pair of external propagators which connect the wiggly lines with the external dots. Let's consider two external electron propagators the variables of which are not summed and integrated. These two propagators are linked by a complicate series of other electron and phonon propagators. This means that we can rewrite the series for the full propagator (Eqn. (3.24)) as shown in Fig. (3.3, a). The labels are in energy after a Fourier transform.

The new formulation shows that the perturbation theory for the Green's function can be written as:

$$G(\lambda, E) = G_0(\lambda, E) + G_0(\lambda, E) \tilde{\Sigma}_{ph}(E) G_0(\lambda, E) \quad (3.34)$$

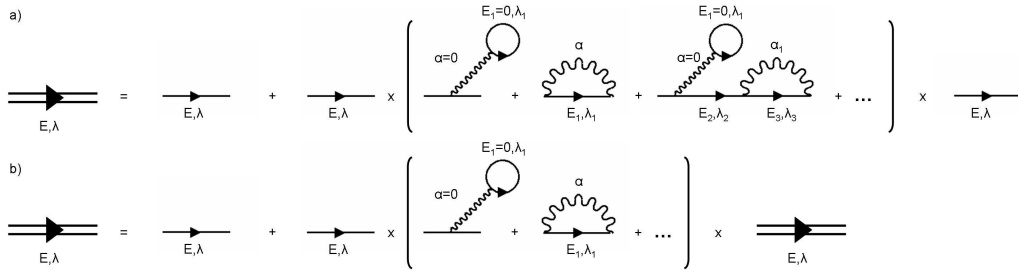


Figure 3.3: The diagrammatic representations of Eqn. (3.34) and Eqn. (3.35).

where $\tilde{\Sigma}_{ph}$ represents all the contributions between square brackets in Fig. (3.3, a). $\tilde{\Sigma}_{ph}$ can be rearranged in a nicer way. First of all we can define two classes of diagrams: the first class is represented by the so called reducible diagrams. A reducible diagram is a diagram that can be split in other two more elementary diagrams just removing one electron propagator (a solid line). An example of a reducible contribution is represented by the third diagram inside the bracket in Fig. (3.3, a). All diagrams which are not reducible are called irreducible (see for example the first two diagrams in the same figure). The sum over square brackets for $\tilde{\Sigma}_{ph}$ can be rearranged tacking only the irreducible diagrams into account. If we do so the Fourier transform for the full Green's function becomes:

$$G(\lambda, E) = G_0(\lambda, E) + G_0(\lambda, E)\Sigma_{ph}(E)G(\lambda, E) \quad (3.35)$$

The difference between Eqn. (3.34) and Eqn. (3.35) is that now Σ_{ph} contains only the irreducible diagrams. This equation is called *Dyson's equation*. In diagram form it looks like in Fig. (3.3, b). Eqn. (3.35) can be rearranged as follows

$$G(\lambda, E) = (G_0^{-1}(\lambda, E) - \Sigma_{ph}(E))^{-1}. \quad (3.36)$$

The Dyson's equation is the fundamental equation for the solution of the propagator as much as the Meir-Wingreen equation is for the current. It states that the exact Green's function is obtained from Eqn. (3.35) by just calculating the self-energy Σ_{ph} . The self-energy is a summation of an infinite number of distinct diagrams. This method is only useful if we can approximate Σ_{ph} by the lowest few irreducible terms. $\Sigma_{ph}(E)$ is a sort of potential that includes all the effects of the phonons over the propagation of the electrons. Except in a few rare cases, it is impossible to get Σ_{ph} exactly, and one must be content with an approximate result.

If the approximate result is not a very good approximation, one should not try to solve the problem in this fashion, in fact the evaluation cost for the irreducible diagrams increases very quickly. Basically one should realize that Dyson's equation is useful only in weak coupling theory, where the perturbation is sufficiently weak that an adequate approximation is obtained with a few terms in $\Sigma_{ph}(E)$. An important issue is the convergence of Eqn. (3.36) which depends fundamentally on the shape of the self-energy. The presence of

poles in the Green's function tell us that this argument is a very delicate one and that the behavior of the Green's function obtained via perturbation expansion is not easy. A way to avoid bad divergences relies on the so called renormalization technique which is beyond the scope of this work (see [51]).

One aspect of this result deserves a special mention. The self-energy has real and imaginary parts which switches sign depending on whether $E > \mu$ or $E < \mu$ where μ is the chemical potential of the system. The same happens if we compute a self-energy for the phonon propagators:

$$\begin{aligned} \text{Im}(\Sigma_{ph}(E)) &< 0 & E > \mu \\ \text{Im}(\Sigma_{ph}(E)) &> 0 & E < \mu \end{aligned} \quad (3.37)$$

For the phonon propagator we can find another Dyson's equation with a different self-energy, $\Pi(E)$, which is sometimes called polarization operator. This name is quite descriptive, since the self-energy effects arise from the phonons causing polarization in the medium. In our methodology the self-energy of the phonon is neglected.

The real and imaginary parts of the self-energies $\Sigma_{ph}(E)$ and $\Pi(E)$ each have interpretations. The imaginary part $\text{Im}(\Sigma_{ph}(E))$ and $\text{Im}(\Pi(E))$ are interpreted as causing the damping of the particle motion. They are related to the finite mean free path of the excitation or to the energy uncertainty. The real parts are actual energy shifts of the excitation, which may also change its dynamical motion. The excitation may alter its effective mass or group velocity because of the self-energy contributions.

3.7 Time-loop S-matrix: NEGF

The formulation of the previous section has been done for the Equilibrium Green's function in which the system is supposed to remain in the equilibrium ground state at the beginning and at the end of the process (that means, the system starts in the ground state for $t = -\infty$ and returns in the same state for $t = +\infty$).

Under this assumption, all the interaction processes included in the self-energy cannot represent real transition of the system because it is forced to go back to the ground state, they are usually called virtual processes. This formalism is all we need to compute the Landauer-Büttiker equation for transport. In the other cases we must move into the Non-equilibrium formalism. Fortunately for us the machinery developed for the equilibrium case remains practically intact. This means that the Green's function machinery can be applied, after some generalizations, also for transport problems in which scattering processes are present.

The S-matrix we have defined in Eqn. (3.15) depends on real time taken over the interval $(-\infty, +\infty)$. Now, assuming that also for a real interacting system we can assume the adiabatic switching on of the interaction part of the Hamiltonian \hat{V} , the system is in its ground state for $t \rightarrow -\infty$. The problem is that this is not true for $t \rightarrow +\infty$ and the state for

that must be defined carefully.

Schwinger suggested another method of handling the asymptotic limit $t \rightarrow +\infty$. He proposed that the time integral in the S -matrix should have two pieces: one going from $(-\infty, \tau)$ while the second going from $(\tau, -\infty)$. Finally, we take the limit $\tau \rightarrow +\infty$. The integration is a time loop which starts and ends at $t = -\infty$. The new Green's function for non equilibrium system is defined over this new loop time variable and retains all the properties and satisfies all the theorems of the equilibrium propagators discussed before (see Fig. (3.4)).

Now we can define four different Green's functions over the time loop axis, depending on which branch the annihilation and creation operators are defined. If we manage also the phonon operators we have then to handle about eight different Green's functions. Fortunately, there are some relations between these different propagators so that we need to compute only two of them for the electrons and two for the phonons. In the case of equilibrium Green's function a further relation reduces the number of independent propagators to one for the electrons and one for the phonons (see [61]).

Limiting to the case of electrons, the reason why there are four different propagators is related to the S -matrix in the contour time:

$$\hat{S}(-\infty, -\infty) = \hat{T}_{C_t} \exp \left[-i \int_{C_t} dt_1 \tilde{V}(t_1) \right] \quad (3.38)$$

The integration path is the time-loop shown in Fig. (3.4). The variable t_1 goes $(-\infty, \tau)$ and then $(\tau, -\infty)$. The operator \hat{T}_{C_t} orders along the entire loop, with earliest values t_1 in C_t^+ occurring first. In expanding the S -matrix, we will encounter Green's functions of the form:

$$G(\lambda, t_1 - t_2) = -i \langle | \hat{T}_{C_t} [\tilde{c}_\lambda(t_1) \tilde{c}_\lambda^\dagger(t_2)] | \rangle \quad (3.39)$$

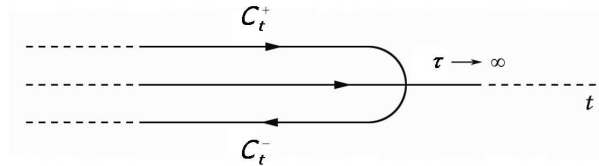


Figure 3.4: The complex time contour for the NEGF formalism. The upper (time ordered) and lower (anti-time ordered) branches are denoted with C_t^+ and C_t^- respectively.

Depending where the two operators are positioned over the contour we can define the four possibilities

1. Both on the upper branch C_t^+ : time ordered Green's function G^t .
2. Both on the lower branch C_t^- : anti-time ordered Green's function $G^{\bar{t}}$.
3. The annihilation operator on the upper branch and the the creation operator on the lower branch: greater Green's function $G^>$.

4. The annihilation operator on the lower branch and the the creation operator on the upper branch: lesser Green's function $G^<$.

The analytic formulation of these four propagators is the following:

$$G^>(t_1, t_2) = -i\langle |\tilde{c}_\lambda(t_1)\tilde{c}_\lambda^\dagger(t_2)| \rangle \quad (3.40)$$

$$G^<(t_1, t_2) = i\langle |\tilde{c}_\lambda(t_2)\tilde{c}_\lambda^\dagger(t_1)| \rangle \quad (3.41)$$

$$G^t(t_1, t_2) = \theta(t_1 - t_2)G^> + \theta(t_2 - t_1)G^< \quad (3.42)$$

$$G^{\bar{t}}(t_1, t_2) = \theta(t_2 - t_1)G^> + \theta(t_1 - t_2)G^< \quad (3.43)$$

$$G^r(t_1, t_2) = G^t - G^< = G^> - G^{\bar{t}} \quad (3.44)$$

$$G^a(t_1, t_2) = G^t - G^> = G^< - G^{\bar{t}} \quad (3.45)$$

where we have added two more propagators, the retarded (G^r) and advanced (G^a), obtained as a linear combination of the previous four. They are particular important for their analytical properties, the retarded propagator has poles only in the lower half of the complex plane, whilst the advanced in the upper part. Moreover, it can be easily demonstrate two fundamental identities between the lesser, greater, retarded and advanced propagators:

$$G^>(E) - G^<(E) = G^r(E) - G^a(E) \quad (3.46)$$

$$G^a(E) = (G^r(E))^\dagger. \quad (3.47)$$

Just to give an example we write the unperturbed propagators for a free electron in time domain and, after a Fourier transform, in energy domain:

$$G_0^>(\lambda; t, 0) = -i(1 - n_F)e^{-i\varepsilon_\lambda t} \rightarrow -2\pi i(1 - n_F)\delta(E - \varepsilon_\lambda) \quad (3.48)$$

$$G_0^<(\lambda; t, 0) = in_F e^{-i\varepsilon_\lambda t} \rightarrow 2\pi i n_F \delta(E - \varepsilon_\lambda) \quad (3.49)$$

$$G_0^t(\lambda; t, 0) = -i[\theta(t) - n_F]e^{-i\varepsilon_\lambda t} \rightarrow \frac{1}{E - \varepsilon_\lambda + i\delta_\lambda} \quad (3.50)$$

$$G_0^{\bar{t}}(\lambda; t, 0) = -i[\theta(-t) - n_F]e^{-i\varepsilon_\lambda t} \rightarrow \frac{-1}{E - \varepsilon_\lambda - i\delta_\lambda} \quad (3.51)$$

$$G_0^r(\lambda; t, 0) = -i\theta(t)e^{-i\varepsilon_\lambda t} \rightarrow \frac{1}{E - \varepsilon_\lambda + i\delta} \quad (3.52)$$

$$G_0^a(\lambda; t, 0) = i\theta(-t)e^{-i\varepsilon_\lambda t} \rightarrow \frac{1}{E - \varepsilon_\lambda - i\delta} \quad (3.53)$$

where δ and δ_λ are infinitesimal quantity, δ is always positive while δ_λ is negative for occupied states and positive for unoccupied states.

The same rules apply for phonon propagators:

$$D_{\alpha}^{>}(t_1, t_2) = -i\langle|\tilde{Q}_{\alpha}(t_1)\tilde{Q}_{\alpha}(t_2)|\rangle \quad (3.54)$$

$$D_{\alpha}^{<}(t_1, t_2) = -i\langle|\tilde{Q}_{\alpha}(t_2)\tilde{Q}_{\alpha}(t_1)|\rangle \quad (3.55)$$

$$D_{\alpha}^t(t_1, t_2) = \theta(t_1 - t_2)D_{\alpha}^{>} + \theta(t_2 - t_1)D_{\alpha}^{<} \quad (3.56)$$

$$D_{\alpha}^{\bar{t}}(t_1, t_2) = \theta(t_2 - t_1)D_{\alpha}^{>} + \theta(t_1 - t_2)D_{\alpha}^{<} \quad (3.57)$$

$$D_{\alpha}^r(t_1, t_2) = D_{\alpha}^t - D_{\alpha}^{<} = \theta(t_1 - t_2)[D_{\alpha}^{>} - D_{\alpha}^{<}] \quad (3.58)$$

$$D_{\alpha}^a(t_1, t_2) = D_{\alpha}^t - D_{\alpha}^{>} = -\theta(t_2 - t_1)[D_{\alpha}^{>} - D_{\alpha}^{<}] \quad (3.59)$$

For the free phonon propagators we get,

$$\begin{aligned} D_0^{>}(\alpha; t, 0) &= -i[(N_{\alpha} + 1)e^{-i\omega_{\alpha}t} + N_{\alpha}e^{i\omega_{\alpha}t}] \\ &\rightarrow -2\pi i[(N_{\alpha} + 1)\delta(E - \omega_{\alpha}) + N_{\alpha}\delta(E + \omega_{\alpha})] \end{aligned} \quad (3.60)$$

$$\begin{aligned} D_0^{<}(\alpha; t, 0) &= -i[(N_{\alpha} + 1)e^{i\omega_{\alpha}t} + N_{\alpha}e^{-i\omega_{\alpha}t}] \\ &\rightarrow -2\pi i[(N_{\alpha} + 1)\delta(E + \omega_{\alpha}) + N_{\alpha}\delta(E - \omega_{\alpha})] \end{aligned} \quad (3.61)$$

$$D_0^r(\alpha; t, 0) = -2\theta(t)\sin(\omega_{\alpha}t) \rightarrow \frac{2\omega_{\alpha}}{E^2 - \omega_{\alpha}^2 + i\delta} \quad (3.62)$$

$$D_0^a(\alpha; t, 0) = -2\theta(-t)\sin(\omega_{\alpha}t) \rightarrow \frac{2\omega_{\alpha}}{E^2 - \omega_{\alpha}^2 - i\delta} \quad (3.63)$$

The phonon Green's functions in equilibrium are expressed in terms of the phonon occupation number N_{α} , which equals to a Bose-Einstein distribution in thermal equilibrium at finite temperature.

3.7.1 Dyson's equations for NEGF

Keldysh was the first to reformulate the NEGF formalism in a matrix notation which preserves the intuitive picture of the loop time contour, but, at the same time, results to be a better tool to handle the many propagators. The advantage of the matrix notation is that we can reformulate all the propagators in one matrix 2×2 and we can extract all the properties of the different propagators just by the usual matrix algebra:

$$\mathbf{G} = \begin{pmatrix} G^t & -G^{<} \\ G^{>} & -G^{\bar{t}} \end{pmatrix} \quad (3.64)$$

where \mathbf{G} satisfies the Dyson's equation

$$\mathbf{G} = \mathbf{G}_0 + \mathbf{G}_0 \Sigma_{ph} \mathbf{G}. \quad (3.65)$$

This matrix notation, as already suggested by Eqn. (3.65), can be extended to all the other quantities, like self-energies and so on. Applying a rotation in the Keldysh space, it is possible to get another particularly useful matrix representation in which, instead of the time ordered and anti-time ordered propagators, the retarded and advanced propagators appear:

$$\mathbf{G}' = \begin{pmatrix} G^r & G^> + G^< \\ 0 & G^a \end{pmatrix}. \quad (3.66)$$

Using the Dyson's equation in Eqn. (3.65) we get the Dyson's equations for the retarded, advanced and lesser and greater quantities:

$$G^{r,a} = G_0^{r,a} + G_0^{r,a} \Sigma^{r,a} G^{r,a} \quad (3.67)$$

$$G^{<, >} = [1 + G^r \Sigma^r] G_0^{<, >} [1 + G^a \Sigma^a] + G_0^r \Sigma_{ph}^{<, >} G^a \quad (3.68)$$

Iterating the matrix representation we can obtain the formula for operators X which depends on two or more operators ($X = AB$ or $X = ABC$). A summary of the results, using the so called *Langreth rules* [61], is presented in Table (3.1).

Contour time	Real time
$X = \int_{C_t} AB$	$X^< = \int_t [A^r B^< + A^< B^a]$ $X^r = \int_t A^r B^r$
$Y = \int_{C_t} ABC$	$Y^< = \int_t [A^r B^r C^< + A^r B^< C^a + A^< B^a C^a]$ $Y^r = \int_t [A^r B^r C^r]$
$X(t, t') = A(t, t')B(t, t')$	$X^<(t, t') = A^<(t, t')B^<(t, t')$ $X^r(t, t') = A^<(t, t')B^r(t, t') + A^r(t, t')B^<(t, t') + A^r(t, t')B^r(t, t')$
$Y(t, t') = A(t, t')B(t', t)$	$Y^<(t, t') = A^<(t, t')B^>(t', t)$ $Y^r(t, t') = A^<(t, t')B^a(t, t') + A^r(t, t')B^<(t', t)$

Table 3.1: *Langreth rules for analytical continuation of propagators and self-energies from the contour time back to real time. The rules for advanced and greater quantities can be obtained starting from the one for retarded and lesser, just exchanging all F^r with F^a and all $F^<$ with $F^>$ and viceversa.*

Density Functional Based Tight-Binding

In Chapter 3 was shown that a full Non-Equilibrium Green's Function (NEGF) formalism can be developed via a perturbation approach starting from zero order building blocks. The zero order Green's functions, both for phonons and electrons, are supposed to be exactly solvable. This assumption comes from the fact that the Hamiltonian \hat{H} can be partitioned into two parts, \hat{H}_0 and \hat{V} . \hat{H}_0 is a reasonable approximation of the full Hamiltonian that can be solved exactly and that contain both a single particle Hamiltonian \hat{H}'_0 and two other terms for the open boundary conditions.

In many NEGF calculations for molecular transport simulations the starting point is a Density Functional Theory (DFT) calculation. In fact, despite some important drawbacks of the method, DFT is still the best compromise between complexity and accuracy for molecular electronic simulations. The main advantage of DFT compared to other ab-initio methods, is the possibility to include a large number of atoms from the contacts for the extended molecule regions and to handle the open boundary conditions. Moreover, the electron-electron correlation can be included immediately via an exchange-correlation functional without any other effort at the Green's function level. However, it is well known that the correlation included in DFT, especially at the lowest level of approximation, the so called Local Density Approximation (LDA), gives a poor description of the electronic mutual interaction. This leads, in many cases of interest, to a weak evaluation of the electronic spectrum of the molecule and to quantitative and sometimes qualitative errors in the current calculated, compared to experiments. One dramatic example is represented by the underestimation of the energy gap between the Highest Occupied Molecular Orbital (HOMO) and the Lowest Unoccupied Molecular Orbital (LUMO) which produces an overestimation of the magnitude of the current (sometimes of a couple of orders of magnitude). At the end of the present Chapter these problems will be addressed in a more specific way.

The present work is based on a code the development of which started in the early 1990, a DFT based Tight-Binding called DFTB. Recently, a new version of the code used in this work, not specifically for transport, has been released under the name DFTB+ (see at the website <http://www.dftb-plus.info>). However, several other implementations of DFTB exist. The description of DFTB is briefly treated in this Chapter, nevertheless, we refer the

interested reader to the wide literature about the method of DFTB [62, 63, 64] and more in general DFT [65, 66] for a more comprehensive documentation.

4.1 DFT and Kohn-Sham formulation

Compared to other methods, DFT recasts the problem of calculating the electronic structure of a system in terms of the electronic density. The spin-free density in terms of the wave function can be formally defined as follows:

$$n(\mathbf{r}) = N \int \Psi^*(\mathbf{r}, \mathbf{r}_2, \dots, \mathbf{r}_N) \Psi(\mathbf{r}, \mathbf{r}_2, \dots, \mathbf{r}_N) d\mathbf{r}_2 \dots d\mathbf{r}_N \quad (4.1)$$

where $\Psi(\{\mathbf{r}_i\})$ is the multi-particle wave function. The concept of employing the electron density in an energy functional dates back to Thomas-Fermi theory [67, 68]. The very foundation of DFT are two rigorous statements. The first is a lemma linking the density and the potential of a Hamiltonian. The second is a theorem about the existence of a universal functional of the electron density, universal in the sense that does not depend on the external potential. This functional can be minimized, with a contribution which comes from the external potential, in a variational sense. The minimum is achieved for the ground states density and gives the ground state energy.

Lemma (*Basic Lemma of Hohenberg-Kohn*) *The ground state density $n(\mathbf{r})$ of a bound system of a fixed number of interacting electrons in an external potential $V_{ext}(\mathbf{r})$ determines this potential uniquely (to within an additive constant).*

The very first step for the study of molecules and solids is the calculation of the total energy of a given arrangement of atoms; eventually, we want to find, within suitable boundary conditions, the atomic arrangement that is lowest in total energy and hence the most stable. Besides contributions from the internuclear interactions, this task requires knowledge of the energy of the electronic system. The energy of the system is related to the wave function and so to the Schrödinger equation. The lowest eigenvalue represents the ground state of the system. For a physical system the problem can be rearranged starting from the density of electrons. From the *Lemma* we know that the density fixes the external potential and, therefore, the Hamiltonian. On the other hand the Hamiltonian defines completely the spectrum of wave functions. This means that there is a fundamental connection between the electron density and the ground state of the system, $\Psi_0(\{\mathbf{r}_i\})$. Hence, the latter is strictly a functional of $n(\mathbf{r})$, albeit not a trivial one. This means that the energy of the system can be expressed as a pure functional of the density:

$$E[n] = \int V_{ext}(\mathbf{r})n(\mathbf{r})d\mathbf{r} + F[n] \quad (4.2)$$

The functional is split in two parts: the first term depends only on the external potential and the density, the second contains all the information about the kinetic and Coulomb interaction between the electrons. The functional $F[n]$ is universal in the sense that it does not

refer to an external potential. A minimization step, in the space of all densities for which the functional $F[n]$ is defined, is required to find the density n_{GS} of the system and so the ground state energy. This variational principle is supported by the following theorem.

Theorem (*Hohenberg-Kohn variational principle*) *For all densities the functional $E[n]$ has a minimum, which it assumes at the ground state density n_{GS} .*

$$\min(E[n]) = E[n_{GS}] \quad (4.3)$$

The electronic ground state energy of a system of interacting electrons is thus expressed in terms of their spatial charge density instead of the many-particle wave function. The main problem of DFT is to find the shape of the universal functional $F[n]$. The statements on which DFT is based demonstrate only the existence of this functional, but they do not suggest how we can build it.

4.1.1 The Kohn-Sham equations

In 1965 Kohn and Sham [69] proposed a new reformulation of the energy functional, Eqn. (4.2), in order to find an analytical solution for it. The functional $F[n]$ is split into parts:

$$F[n] = T_0[n] + E_H[n] + E_{xc}[n] \quad (4.4)$$

There are three components. The first term, $T_0[n]$, is the kinetic energy functional for a fictitious system of non-interacting electrons producing the same density as $n(\mathbf{r})$. The second term, $E_H[n]$, is the so called Hartree energy, arising classically from the mutual Coulomb repulsion of all electrons:

$$E_H[n] = \frac{1}{2} \int \int \frac{n(\mathbf{r})n(\mathbf{r}')}{|\mathbf{r} - \mathbf{r}'|} d\mathbf{r}d\mathbf{r}' \quad (4.5)$$

The last term, $E_{xc}[n]$, called the exchange-correlation functional, is a correction term, which accounts for all many-body effects in $F[n]$. The treatment of this term decides upon the viability of any DFT implementation. All terms but the last of Eqn. (4.4) are known analytically. The functional form of the correction term $E_{xc}[n]$ is unknown and must be approximated. Practical applications of the DFT are classified according to the approximations taken for the exchange-correlation functional $E_{xc}[n]$.

The first attempt to give a shape to the exchange-correlation functional has been the LDA,

$$E_{xc}[n] = \int \varepsilon_{xc}[n(\mathbf{r})]n(\mathbf{r})d\mathbf{r} \quad (4.6)$$

where $\varepsilon_{xc}[n]$ is the exchange-correlation energy per electron in a uniform electron gas of density $n(\mathbf{r}) = \text{const}$. The energy $\varepsilon_{xc}[n]$ is a function of only the local density value, and no longer a functional of the global density distribution and its form is well known.

The $T_0[n]$ term can be described defining a set of single particles orbitals which are orthogonal and normalized and that are related to the real density of the system as follows:

$$n(\mathbf{r}) = \sum_{i=1}^{\infty} n_i |\Phi_i(\mathbf{r})|^2 \quad (4.7)$$

$$\langle \Phi_i | \Phi_i \rangle = \int |\Phi_i(\mathbf{r})|^2 d\mathbf{r} = 1 \quad (4.8)$$

where n_i are the occupation numbers of these orbitals. The occupation numbers are constrained to be a certain set of values: integer numbers (0 and 1 for spin-unrestricted solution and 0,1 and 2 for spin-restricted solutions) or real numbers following a Fermi-Dirac distribution in case of small thermal excitation. The kinetic term becomes:

$$T_0[\{\Phi_i(\mathbf{r})\}] = \sum_{i=1}^{\infty} n_i \int \Phi_i^*(\mathbf{r}) \left(-\frac{\Delta}{2} \right) \Phi_i(\mathbf{r}) d\mathbf{r} \quad (4.9)$$

The entire functional, $E[n]$, can be expressed as a functional of the new orbitals. The minimum of the energy functional with respect to the density becomes a variation respect the orbitals, with the constraint that the orbitals must remain orthogonal and normalized:

$$\frac{\delta}{\delta \Phi_i^*(\mathbf{r})} \left\{ E[n(\mathbf{r})] + \sum_{i=1}^{\infty} \varepsilon_i \left[1 - \int |\Phi_i(\mathbf{r})|^2 d\mathbf{r} \right] \right\} = 0 \quad (4.10)$$

where the ε_i are the Lagrange parameters. Solving Eqn. 4.10 we get at the end a Schrödinger-like equation,

$$\left[-\frac{\Delta}{2} + V_{ext}(\mathbf{r}) + V_H([n(\mathbf{r})], \mathbf{r}) + V_{xc}([n(\mathbf{r})], \mathbf{r}) \right] \Phi_i(\mathbf{r}) = \varepsilon_i \Phi_i(\mathbf{r}), \quad (4.11)$$

this equation plus Eqn. (4.7) are called the Kohn-Sham equations. The three terms V_{ext} , V_H and V_{xc} are the variational counterpart of the energy functional. Their sum is a potentials which describe the external field, the classical electron-electron repulsion and the many-body effects (exchange due to Pauli exclusion principle and correlation) respectively. The picture of Kohn-Sham equations is a set of N not interacting particles merged in a effective external potential which is the sum of these three terms. We can be tempted to give a physical interpretation to the eigenvalues (Lagrange parameters) of Eqn. (4.11) ε_i . Janak has demonstrated [70] that, in fact, the eigenvalue of the highest occupied orbital is fundamentally the first ionization energy changed in sign. The interpretation of the others eigenvalues is more controversial.

An analytic solution of the Kohn-Sham equations is rather difficult. Instead, the unknown functions $\Phi_i(\mathbf{r})$ are sought numerically employing tools from mathematical physics. Two classes of approaches will yield a solution: real-space grid methods and basis function expansions. Either approach will transform the differential equation for the unknown functions into a set of algebraic ones for unknown expansion coefficients of a reference

basis of functions. The general expansion of the one-electron wave functions reads:

$$\Phi_i(\mathbf{r}) = \sum_{v=1}^N C_{iv} \phi_v(\mathbf{r}) \quad (4.12)$$

Once the basis is chosen, depending to the kind of problem, the coefficients C_{iv} are obtained solving a general secular equation:

$$\sum_{v=1}^N C_{iv} (h_{\mu v} - \varepsilon_i S_{\mu v}) = 0 \quad (4.13)$$

where

$$h_{\mu v} = \langle \phi_\mu | \hat{H}'_0 | \phi_v \rangle = \int \phi_\mu^* \left[-\frac{\Delta}{2} + V_H + V_{xc}([n(\mathbf{r})], \mathbf{r}) \right] \phi_v d\mathbf{r} \quad (4.14)$$

$$S_{\mu v} = \langle \phi_\mu | \phi_v \rangle = \int \phi_\mu^* \phi_v d\mathbf{r} \quad (4.15)$$

Since the orbital solution depends on the density, and in turn, by Eqn. (4.12), on the orbitals themselves, Eqn. (4.14) needs to be solved self-consistently starting from a guess density, $n_0(\mathbf{r})$.

4.2 DFTB: method and approximations

The Kohn-Sham equation are implemented in the DFTB method with some approximations. These mostly take the form of separations of global quantities like potentials and wave functions into atomic contributions. This separation principle allows the effective treatment of compound atomic systems by building as much as possible upon preparatory work, which is performed beforehand on isolated subsystems of atoms and atom pairs. This previous work is used to evaluate the computational expensive reference Hamiltonian and other contributions, like the nuclei repulsion, into simple tables.

The total-energy expression of the DFTB approach follows the one that can be derived from full Kohn-Sham equations,

$$\begin{aligned} E_{tot}[n_0 + \Delta n] &= \sum_{i=1}^{occ} n_i \langle \Phi_i | \hat{h}_0 | \Phi_i \rangle + E_{rep}[n_0] + E_2[n_0, \Delta n] \\ &= E_{BS} + E_{rep} + E_2 \end{aligned} \quad (4.16)$$

where E_{BS} is the trace of the eigenstates of the system over a Hamiltonian \hat{h}_0 which depends on the guess density n_0 only:

$$\hat{h}_0 = -\frac{\Delta}{2} + V_{eff}[n_0, \mathbf{r}]. \quad (4.17)$$

The second term, E_{rep} constitutes a repulsion energy similar to standard tight-binding theory, which subsumes the double counting terms of the reference Hamiltonian, as well as the nuclear repulsion. Finally, the last term, E_2 , describes atomic charge fluctuations and is subject to a self-consistent treatment.

The main approximations to obtain the DFTB method from the stationary principle of DFT are in turn:

- superposition of pseudo-atomic densities as starting density;
- usually a minimal-basis, valence-only Linear Combination of Molecular Orbital (LCAO) wave functions, is used;
- two-centre Hamiltonian (neglect of crystal-field and three-centre terms);
- repulsive pair potential for the double-counting and inter-nuclear energies;
- for the second-order correction:
 1. monopole approximation and extrapolation of $\delta V_{xc}[n]/\delta n$;
 2. Mulliken charges;
 3. Integral approximations for the γ matrix;

4.2.1 Pseudo-atomic starting density

In DFTB, the starting density is chosen as superposition of slightly compressed densities of neutral atoms,

$$n_0(\mathbf{r}) = \sum_a n_0^a(\mathbf{r}_a); \quad \mathbf{r}_a = \mathbf{r} - \mathbf{R}_a \quad (4.18)$$

The densities of free atoms are too diffuse to be a good initial guess in compound systems. The densities are the result of a self-consistent LDA or General Gradient Approximation (GGA) calculation of *pseudo-atoms*, i.e., atoms placed within a weak parabolic constriction potential as expressed in a modified Kohn-Sham equation:

$$\left[-\frac{\Delta}{2} + V_{eff}^{at}[n_0^a] + \left(\frac{r}{r_0} \right)^m \right] \psi_v^{psat}(\mathbf{r}) = \epsilon_v^{psat} \psi_v^{psat}(\mathbf{r}) \quad (4.19)$$

The constriction potential is characterized by its exponent m and range r_0 . The exponent was shown to have rather small influence on the final results, so that $m = 2$ is usually used. For the range parameter, a number of calculations has lead to results with optimal transferability in covalent systems (barring $3d$ transition metals) using $r_0 \approx 1.85r_{cov}$, where r_{cov} is the covalent radius of the given element. The pseudo atomic wavefunctions are used for the LCAO basis. These wavefunctions are represented by Slater-type orbitals (STO) characterized by coefficients a_{ij} and exponents α_i :

$$\psi_v(\mathbf{r}) \equiv \psi_{lmn}(\mathbf{r}) = \sum_{i=1} \sum_{j=0} a_{ij} r^{l+j} e^{-\alpha_i r} Y_{lm} \left(\frac{\mathbf{r}}{r} \right). \quad (4.20)$$

4.2.2 Tight-binding integrals and the two-centre approximation

The pseudo-atomic are used as basis set for the expansion of the eigenfunctions

$$\Phi_i(\mathbf{r}) = \sum_a \sum_{\nu[a]} C_{i\nu} \psi_\nu(\mathbf{r}_a). \quad (4.21)$$

The reference Hamiltonian can be represented on this basis, giving matrix elements denoted $h_{\mu\nu}^0$ and non-orthogonal overlap elements $S_{\mu\nu}$,

$$h_{\mu\nu}^0 = \langle \psi_\mu | \hat{h}_0 | \psi_\nu \rangle \quad (4.22)$$

$$S_{\mu\nu} = \langle \psi_\mu | \psi_\nu \rangle = \int \psi_\mu^* \psi_\nu d\mathbf{r}. \quad (4.23)$$

These integrals are calculated immediately and are tabulated as function of distance between the two centres. The integrals at general difference vectors as needed in the system, $\Delta\mathbf{R}_{ab} = \mathbf{R}_a - \mathbf{R}_b$, are transformed using projection relations [71]. Due to symmetry, only few integrals between basis functions remain nonzero for angular momenta up to $l = 2$.

In order to achieve the *two-centre* representation for the Hamiltonian matrix elements, the effective Kohn-Sham potential is formally decomposed into atomic-like contributions. Due to the non-linearity of the exchange-correlation potential, there are two ways to do this in practice, either to sum atomic *potentials* or atomic *densities*:

$$V_{eff}[n_0, \mathbf{r}] \approx \begin{cases} \sum_c V_c^0[n_c^0, \mathbf{r}_c] & \text{potential superposition} \\ V_{eff}[\sum_c n_c^0] & \text{density superposition} \end{cases} \quad (4.24)$$

Depending on the centres involved for the basis functions and the potential, the Hamiltonian matrix elements fall into a number of categories, which are summarized in Table (9.1).

Type	Classification	Centres	Status
(A)	onsite-terms	$a = b = c$	retained
(B)	crystal-field terms	$a = b \neq c$	neglected
(C)	two-centre terms	$a \neq b, c = a$ or $c = b$	retained
(D)	three-centre terms	$a \neq b \neq c$ and $b \neq c$	neglected

Table 4.1: Integral types in the DFTB Hamiltonian $h_{\mu\nu}^0$. Centres a and b denote orbital centres, with basis functions $\mu \in a$, $\nu \in b$ and c is the potential centre.

The neglect of three-centre terms provides the largest practical simplification because on the one hand the handling for three centres is more involved than for two centres and on the other hand there are many more combinations. On the other hand, the crystal-field integrals are relatively simple. However, the integral neglects work only in concert because there is error-cancellation of a considerable degree. The justification of this process is complex and was discussed originally by Seifert *et al.* [72] and later reviewed in ref. [63].

Moreover, using a valence-only basis assures the core-valence orthogonalisation between different centres.

Among the retained integrals, type (A) represents on-site energies ε_v of single atoms,

$$h_{vv}^0 = \varepsilon_v \quad (4.25)$$

which are obtained in the first step of the atom calculation. In the other remaining integral type (C), the potentials and densities of two distinct atoms are to be combined:

$$h_{\mu\nu}^0 = \langle \psi_\mu | -\frac{\Delta}{2} + \left\{ \begin{array}{c} V_a^0[\mathbf{r}_a] + V_b^0[\mathbf{r}_b] \\ V_{eff}[n_a^0 + n_b^0] \end{array} \right\} | \psi_\nu \rangle; \quad a[\mu], b[\nu]. \quad (4.26)$$

4.2.3 Repulsive potential

The next term that must be evaluated is the so called repulsive term which includes the double-counting terms between E_{BS} , evaluated at the input density, and E_2 , the self-consistent correction, in the energy functional. Moreover, it includes also the inter-nuclear repulsion

$$E_{nuc} = \frac{1}{2} \sum_{a,b \neq a}^{N_{at}} \frac{Z_a Z_b}{|\mathbf{R}_a - \mathbf{R}_b|}. \quad (4.27)$$

The DFTB Method sum of short-ranged repulsive pair potentials:

$$E_{rep}[n_0, \{\mathbf{R}_a\}] \approx \frac{1}{2} \sum_a \sum_{a \neq b} V_{rep}^{ab}(|\mathbf{R}_a - \mathbf{R}_b|). \quad (4.28)$$

This approximation is justified by two observations:

- With n_0 represented by neutral atomic fragments, there are no long-range Coulomb interactions in the combined electrostatic Hartree and nuclear contributions to the double counting energy, $E_H[\sum_a n_0^a] + E_{nuc}(\mathbf{R}_a)$, due to mutual screening. Furthermore, since the atomic starting densities are spherically symmetric, the Hartree integrals for atom pairs (4.5) depend on internuclear distance only. The same is trivially the case for the nuclear repulsion. Therefore, these contributions together are representable by short-range pair potentials without loss of accuracy.
- Contributions due to exchange and correlation are not separable into pair potential form per se because of the non-linearity of the xc-functional. However, a cluster expansion [63] allows to extract two-body components. Its higher order terms involve the overlap of the densities of three centres, which is negligible for the compressed starting densities used here. The remaining two-body terms may again be represented by pair-potentials.

All monomer contributions are contained within the atomic orbital energies ε_v to ensure that the repulsive potential actually goes to zero in the dissociation limit. The repulsive

potential is obtained from self-contained ab initio calculations of the energy of a set of reference molecules for a range of a typical bond length. This is the most delicate term in the DFTB method, because still there is not a systematic way to get a set of molecules and compounds that can assure the transferability of the values obtained. Most conveniently, the reference molecules are dimers, but also methane-like structures. For solid state calculations, as in gold crystals which are widely used in this work, crystal reference structures may be used. For each reference structure j , the energy difference,

$$\tilde{E}_{rep}^j(r) = E_{scf}^j(r) - E_{BS}^j(r) \quad (4.29)$$

is calculated as function of distance r . As a consequence of the concepts and approximations taken thus far, the set of repulsive energies has the following important properties:

- Usually $\tilde{E}_{rep}^j > 0$. For small distances, i.e., close atoms, E_{rep} has a steep repulsive slope indicative of strong Pauli repulsion of the electron shells and the ion-ion repulsion.
- It decays rapidly to zero between typical first- and second-neighbor distances. This is another indication that the pair-potential representation of the double-counting terms embodied within E_{rep} , is valid.
- Most importantly, \tilde{E}_{rep}^j for different molecules are close to each other. This property is indicative of the degree of *transferability* of the method, i.e., its applicability to a wide range of atomic structures.

It was found that $\tilde{E}_{rep}(r)$ for high-coordinated crystal phases such as *fcc* and *bcc* often does not coincide with the curve of other structures. Such phases cannot be treated with the present method. All the crystalline gold electrodes used in the simulations in the last four Chapters (6- 9) were in fact not allowed to relax using DFTB. For practical calculations, the set of repulsive energies are represented numerically by splines for each atom type combination.

4.2.4 Second-order correction

The last term in the DFTB total-energy expression to discuss is the second-order correction $E_2[n_0, \Delta n]$. This term becomes important in the simulation of heteroatomic molecules and polar semiconductors where chemical bonding is influenced considerably by charge transfer effects and long-range Coulomb interactions.

In line with previous procedures, the charge fluctuations Δn are decomposed into atomic contributions which are expected to decay rapidly with increasing distance from their centre. The second-order term then reads,

$$E_2[n_0, \Delta n] = \frac{1}{2} \sum_{a,b} \int \int \left[\frac{1}{|\mathbf{r} - \mathbf{r}'|} + \frac{\delta V_{xc}([n(\mathbf{r}), \mathbf{r}])}{\delta n(\mathbf{r}')} \right]_{n_0} \Delta n_a \Delta n_b d\mathbf{r} d\mathbf{r}' \quad (4.30)$$

The term is expected to give a small contribution of the total energy, so that integrations can be approximated. First, one expresses Δn_a as a mere monopole contribution:

$$\Delta n_a(\mathbf{r}) = \sum_{lm} c_{lm}^a F_{lm}^a(\mathbf{r}_a) Y_{lm} \left(\frac{\mathbf{r}_a}{r_a} \right) \approx \Delta q_a F_{00}^a(\mathbf{r}_a) Y_{00}; \quad \mathbf{r}_a = \mathbf{r} - \mathbf{R}_a. \quad (4.31)$$

Thus, Eqn. (4.30) takes a simple matrix form:

$$E_2[n_0, \Delta n] \approx \frac{1}{2} \sum_{a,b}^M \gamma_{ab} \Delta q_a \Delta q_b \quad (4.32)$$

where γ matrix is:

$$\gamma_{ab} = \frac{1}{4\pi} \int \int \left[\frac{1}{|\mathbf{r} - \mathbf{r}'|} + \frac{\delta V_{xc}[n]}{\delta n(\mathbf{r}')} \right]_{n_0} F_{00}^a(\mathbf{r}_a) F_{00}^b(\mathbf{r}'_b) d\mathbf{r} d\mathbf{r}'. \quad (4.33)$$

The γ matrix contains the dependency of E_2 on ionic positions. This matrix, except for the V_{xc} part, is well known from the CNDO-formalism by Pople, Santry and Segal [73]. The F_{00}^i term is the normalized radial dependence of the density fluctuation on atom i . If the latter are assumed to have a fixed form, spherically symmetric, to be weighted by Δq_a , the only geometry parameter in γ_{ab} will be the interatomic distance $R = |\mathbf{R}_a - \mathbf{R}_b|$. The limit $R \rightarrow 0$ means coinciding atomic centres a and b . In this case, γ_{aa} equals a Hubbard-like parameter U_a for the atom. The Hubbard parameter is related to the chemical hardness $\eta \approx U_a/2$, which is a measure of the ionization potential and electron affinity of the atom. Neglecting the influence of the environment and employing Janak's theorem [70], U_a is obtained non-empirically at the DFT level during the pseudo-atom calculation as the derivative of the HOMO of the free atom with respect to its occupation number:

$$\gamma_{aa} = U_a = \left. \frac{\partial^2 E_{at}}{\partial q_{at}^2} \right|_{q=q_0} = \frac{\partial \epsilon_{HOMO}^a}{\partial n_{HOMO}} \quad (4.34)$$

In the limit of large interatomic distances, γ_{ab} reduces to a $1/R$ dependency, since V_{xc} interactions vanish in this case. To obtain a continuous transition between the limits of small and large interatomic distances an interpolation formula is used [74]. Assuming a normalized Slater-type function with a range parameter τ_a ,

$$F_{00}^a(r) = \frac{\tau_a^3}{8\pi} e^{-\tau_a |r - R_a|} \quad (4.35)$$

the Coulomb integral of two such charge densities reads, after some manipulations (for integrals of this type, see Pople and Beveridge [75]):

$$\gamma_{ab}(\tau_a, \tau_b, R) = \frac{1}{R} - S(\tau_a, \tau_b, R) \quad (4.36)$$

where

$$\begin{aligned}
S(\tau_a, \tau_b, R) = & e^{-\tau_a R} \left(\frac{\tau_b^4 \tau_a}{2(\tau_b^2 - \tau_a^2)^2} - \frac{\tau_b^6 - 3\tau_b^4 \tau_a}{R(\tau_b^2 - \tau_a^2)^3} \right) + \\
& + e^{-\tau_b R} \left(\frac{\tau_a^4 \tau_b}{2(\tau_a^2 - \tau_b^2)^2} - \frac{\tau_a^6 - 3\tau_a^4 \tau_b}{R(\tau_a^2 - \tau_b^2)^3} \right); \quad \tau_a \neq \tau_b \quad (4.37)
\end{aligned}$$

$$S(\tau, R) = e^{-\tau R} \left(\frac{48 + 33\tau R + 9\tau R^2 + \tau R^3}{48R} \right); \quad \tau_a = \tau_b = \tau \quad (4.38)$$

In the limit of short distances γ_{ab} should equal the Hubbard parameter for an isolated atom. This being a known quantity, one obtains a one-to-one relation between the hitherto unspecified charge fluctuation range τ_a of an atom and its Hubbard parameter:

$$\gamma_{aa} = U_a = \frac{5}{16} \tau_a \quad (4.39)$$

Since Eqn. (4.36) was derived from pure Coulomb interactions, yet the Hubbard parameter incorporates xc contributions, this step may seem inconsistent. To reconcile the approaches, the following should be considered: appreciable deviations from the point charge behavior of $1/R$ occur only close to atoms, namely, within radii of typical bond lengths. Adjusting the inner limit to include xc interactions by way of equating it to the ab-initio DFT value, one corrects mainly the on-site terms of γ_{ab} .

To finally evaluate the second-order energy contributions, one needs the atomic charge deviations Δq_a . These are obtained from Mulliken charges. Given real-valued eigenvectors $C_{i\mu}$ in an atomic basis with overlap matrix \mathbf{S} , the Mulliken charges q_a and charge deviations Δq_a on atoms are:

$$\begin{aligned}
q_a &= \sum_{i=1}^{occ} n_i q_a^i = \sum_{i=1}^{occ} n_i \sum_{\mu[a]} \sum_{\nu} C_{i\mu} C_{i\nu} S_{\mu\nu} = \sum_{\mu[a]} \sum_{\nu} q_{\mu\nu} \\
\Delta q_a &= q_a - q_a^0 \quad (4.40)
\end{aligned}$$

where q_a^0 are the charges of the respective neutral atoms.

4.2.5 DFTB secular equation

With the approximations discussed above the DFTB total-energy reads:

$$E_{tot} = \sum_{i=1}^{occ} n_i \sum_{\mu} \sum_{\nu} C_{i\mu} C_{i\nu} h_{\mu\nu}^0 + \frac{1}{2} \sum_{ab}^{N_{at}} \gamma_{ab} \Delta q_a \Delta q_b + E_{rep}[\mathbf{R}_a] \quad (4.41)$$

Given a set of atomic coordinates $\{\mathbf{R}_a\}$ and the resulting matrices \mathbf{h}^0 , \mathbf{S} and γ , the LCAO coefficients which minimize the DFTB total energy (4.41) are found by the variation principle subject to orbital normalization:

$$\frac{\partial}{\partial C_{i\mu}} \left[E_{tot} + \sum_{i=1}^{occ} n_i \tilde{\epsilon}_i \left(1 - \sum_{\mu} \sum_{\nu} C_{i\mu} C_{i\nu} S_{\mu\nu} \right) \right] = 0 \quad (4.42)$$

The procedure is quite similar to the standard tight binding case. The resulting secular equation reads:

$$\sum_{\nu=1}^N C_{i\nu} (h_{\mu\nu} - \tilde{\epsilon}_i S_{\mu\nu}) = 0 \quad (4.43)$$

where, as a consequence of the minimization of E_2 alongside E_{BS} the original Hamiltonian matrix elements are augmented as follows:

$$h_{\mu\nu} = h_{\mu\nu}^0 + \frac{1}{2} S_{\mu\nu} \sum_c^M (\gamma_{ac} + \gamma_{bc})(q_c - q_c^0) \quad \mu \in a; \nu \in b; \quad (4.44)$$

As for the generic Kohn-Sham system, Eqn. (4.43) is a generalized eigenvalue problem which is solved using standard libraries. Since the charges in the augmented Hamiltonian depend upon the coefficients of the solution, the equation has to be solved self-consistently. The iteration is driven by some mixing algorithm for the charges $\{q_a\}$.

Forces on atoms can be obtained analytically without resorting to repeated energy calculations for finite displacements. The essential result of the DFTB calculation is available in form of the total energy and the electronic eigenvectors. Other physical observables like charge distributions or vibrational properties may be extracted, the latter not without considerable numerical effort.

4.3 Disadvantages of DFT in transport simulations

There is a number of significant limitations known to be associated with modern density functionals. These include [76]: poor treatment of dispersive forces, poor treatment of covalent bond breakage, poor treatment of systems involving partial electron removal, and poor treatment of conjugated π systems.

Firstly, dispersive forces are very important for the determination of the geometrical structure of interfaces, being the primary contributor to physisorptive processes including the strong π -stacking interactions that can occur between gold and aromatic molecules, the interactions of nitrogen bases with gold, and contributions along with covalent bonding to thiol-gold interactions. While these forces are treated sporadically by DFT, they are also excluded from the basic DFTB hamiltonian. However, DFTB+ now includes provision for the inclusion of these forces.

Secondly, in general, covalent bond breakage is treated poorly by modern DFT func-

tionals, with their poor description of long-range electron correlation leading to contamination of supposedly radical-like reaction products with ionic-like structures [77, 78]. This failure has immediate consequences for the determination of realistic strained electrode-molecule junction structures as dynamic bond breaking and forming processes are likely to be important. However, it has more profound effects owing to the way in which Green's function-based methods perceive the current carrying process [79]. Effectively, they perceive conduction as occurring between the two macroscopic contacts through tunneling. All that is important is the tunneling probability, effectively obtained from the calculated energy gap between the electrode-localized tunneling orbitals. The process by which this energy gap arises is irrelevant: it could be via direct through-space interactions of the electrodes or via superexchange [80] through molecule-assisted pathways. Viewed in this way, through-molecule conduction is analogous to through-space conduction between two electrodes with broken inter-electrode covalent bonds, allowing errors associated with covalent bond breakage to enter calculations in a profound way. Covalent bond breakage is an open-shell problem for which valid solutions may be obtained using spin-unrestricted means if just one bond is involved [81], a situation not typical in molecular electronics applications.

Inappropriate application of the Kohn-Sham theorem leads to error up to 20% in the underestimation of the magnitude of excited state energies, energies interpreted by Green's function codes as depicting the strength of tunneling, leading to large overestimation of the conductivity. Also, as the LDA functional in DFT provides realistic treatments of the metal electrodes but gives a poor description of the molecular component. Only hybrid functionals, however, include the long-range exchange interactions that are often critical in electron transfer problems. Hence the development of improved density functionals is a priority.

The third limitation of DFT is related to the so called self-interaction energy error. This error arises from the approximated form of the exchange potential in DFT. In exact exchange potential a charge in a certain state cannot interact with itself because the term of self-interaction in the Hartree energy cancels exactly with the same term in exchange potential. In the case of DFT this cancelation is not exact and this means that a certain self-interaction survives. This is particularly problematic for localized states [66]. Practically, this results in low energies for charge transfer states, a type of state that can contribute to through-molecule conductivity, and an incorrectly positioned molecular highest-occupied molecular energy (HOMO) level that is typically too high in energy by 3-4 eV. In molecular electronics applications, this leads to errors in the line-up of the orbital bands of the electrodes and the molecule [82].

Lastly, we consider limitations of standard DFT in treating conjugated π systems. Many molecules used in molecular electronics applications, especially the highly conductive ones, such as 1,4-benzenedithiol, are of this type. Molecular conduction involves partial oxidation or reduction processes of the molecule, processes whose energies are identified in single-particle implementations of Green's function kinetics theories with molecular-orbital energy differences. While such an identification follows naturally from Hartree-Fock based approaches through application of Koopmans' theorem, in DFT the calculated orbital-energy differences actually reflect the much smaller energies associated with optical transitions [82]. Also DFTB is subject to errors of this type [83]. For standard

DFT, the interplay between the self-interaction correction (HOMO error) and the undesired physical interpretation of the band gap is complex. Fortunately, the two errors cancel to some extent for the band line-up of the molecular lowest-energy unoccupied molecular orbital (LUMO).

However, as the self-interaction error also results in significant underestimation of the actual excited-state optical transition energies, both effects reinforce each other in making molecules appear metal-like. Polyacetylene, for example, is predicted by modern density functionals to have a ground state of at least triplet spin multiplicity rather than being a wide band-gap semiconductor [84], with associated errors in calculated polarizabilities for the actual closed-shell ground state [85]. Porphyrin and chlorophyll molecules, ubiquitous for their roles in naturally occurring systems involving through-molecule conduction, are also poorly described [84].

The Electron-Phonon Code

The present Chapter is focused on the implementation of the Green's function code for the electron-phonon interaction based on DFTB. The code was implemented by the author of the present work and Dr. Alessandro Pecchia, of the University of Rome "Tor Vergata". It belongs to the so called gDFTB family, see [86], a set of transport codes applying equilibrium and non equilibrium Green's function formalism and based on DFTB. The codes already developed, beside the electron-phonon, are a gDFTB version for Landauer-Büttiker evaluation of the elastic current and another for a full treatment of the bias in the device with the solution of the Poisson equation in NEGF. The first code is already contained in both the electron-phonon and bias codes as a special case when the interaction, in one case, or the Poisson solving, in the other case, are neglected. A further step will be the merging of the bias and electron-phonon codes in a final program. The aim of this final gDFTB code is to be merged in a full multiscale approach to transport called *TiberCAD*. This final package will contain modules to simulate transport in electronic devices at different scales, from micrometers down to nanoscale, and interlace them. The gDFTB is the atomistic part.

The implementation of an electron-phonon calculation requires a certain number of steps. First of all the definition of the system simulated, that is the definition of the partitioning in device and contact regions. The second step is the relaxation of the geometry between the two electrodes and the calculation of the zero order DFTB Hamiltonian \hat{H}'_0 . The third step is the calculation of the normal mode of vibrations and the evaluation of the electron-phonon coupling matrices elements $M_{\mu\nu}^\alpha$, where the index α runs over all the normal modes and the indices μ and ν over the local basis set. This last step is very delicate because the electron-phonon interaction depends strongly on the couplings. To obtain a good set of couplings we need a fully relaxed geometry, the relaxation of the structure must in fact reach a global minimum in order to really catch a good description of the vibrational spectrum.

Finally the calculation of the current can be performed. The zero order Hamiltonian is used to compute the retarded self-energies needed by the code, for the open boundary conditions (Σ'_L and Σ'_R) and for the electron-phonon interaction (Σ'_{ph}). Indeed, in the NEGF, we need to compute also the equivalent quantities for the lesser and greater quantities. All

the matrices can be later on used to compute the current, via the Meir-Wingreen equation, and the power dissipated in the device.

The Chapter is organized as follows: first, a brief description of the main approximations used in the code is given. Then, the treatment of the open boundary conditions follows. The next sections are devoted to describe in more details the calculation of the electron-phonon self-energies and the vibronic couplings. Finally, the last part of the Chapter describes in details the flowchart of the code.

5.1 Approximations in the electron-phonon code

This short paragraph is focused on the approximations implemented in the electron-phonon code. A full description of the code and its potentiality cannot dispense to address also the main simplifications introduced in the calculations of the quantities needed for the evaluation of the current.

The set of approximations related to the DFTB Hamiltonian have been already described in Chapter 4 and they will be not repeated here. Further approximations appear at the NEGF level. First of all the calculation of the electron-phonon self-energy is performed at the first level of perturbation, called Born approximation (BA). The diagrammatic representation of that term is shown in Fig. (5.2, a).

A better description of interaction can be performed allowing a self-consistent Born approximation (SCBA) in which the propagators of the self-energy is renormalized Fig. (5.2, b). In this way we are including other diagrams in the self-energy. However, the difference in the results between SCBA and BA is usually pretty small, within few percentage. The real advantage of SCBA is that it assures the conservation of the charges in the current. This conservation is in fact slightly broken in the mere BA and this can become a problem in case of high current amount, when for example one of the states of the device is in resonance. However, also an SCBA is not able to describe scattering processes if we are in the strong electron-phonon couple regime. The entire perturbation approach to the self-energy, in fact, fails badly in the latter case.

Problems can arise also in the weak coupling regime if the device region is weakly bounded to the contacts (weak contact couplings). In that case it is possible that the electron lifetime in the device is long enough for the formation of complex deformations of the device itself, like polaron states. Also in that case the perturbation approach is not able to recover the correct quantities. Fortunately, in many molecular electronics experimental setups, like in break-junction experiments, the molecule is strongly bounded to the contacts via thiolate groups and the lifetime of the electrons is small enough and we can assume that we are in the weak electron-phonon coupling regime.

The phonon Green's functions are the free phonon propagators enlisted in Eqs. (3.59). The latter approximation means that the phonon population is regarded as a simple set of Einstein oscillators with infinite lifetime. Moreover, we consider them in thermodynamic equilibrium. The two main consequences are that the phonon population for every mode, N_{α} , is described by a simple Bose-Einstein distribution and, second, that the relaxation of the phonons in the contacts is neglected.

Another approximation is related to the real part of the electron-phonon self-energy. As explained the self-energy contains a real and an imaginary part where the former represents a shift of the energy levels and the latter a lifetime of the particle induced by the electron-phonon interaction. The real and imaginary parts for the retarded Green's function are correlated by the Kramers-Kronig relations which states the following:

$$\text{Re}(\Sigma_{ph}^r) = \frac{1}{\pi} \mathcal{P} \int_{-\infty}^{+\infty} dE' \frac{\text{Im}(\Sigma_{ph}^r)}{E' - E}. \quad (5.1)$$

In the calculations, this real part is neglected because the effects of the shift in energy induced by the contacts is much larger than the one induced by the electron-phonon interaction.

The evaluation of the normal modes, vibrational vectors and frequencies, is performed getting the relaxed geometry after a relaxation of the system. Later on the equilibrium potential for the distribution of atoms is perturbed up to the second order defining a parabolic approximation for the potential in the limit of small vibrations, the so called harmonic approximation. In the evaluation of the spectrum is fundamental to define which atoms are allowed to vibrate. It is obvious that, until we do not allow the relaxation of the phonons from the device to the contacts, the knowledge of the phonon dispersion function for the bulks of the contacts is not required. What is more critic is the decision of which part of the device can vibrate, that means if also some of the leads atoms, the one closest to the interface between the molecule and the leads, should vibrate. In fact the vibrations of the surface and the molecule together can have important effects on the total conduction, like conduction modulation, where the charging and discharging of the molecule induced by vibrations can change dramatically the conduction [87]. In all the calculations presented in Chapters 6-9 only the molecules were allowed to vibrate. This approximation can be particularly questionable when the atoms in the leads have more or less the same mass of the atoms in the molecular region (sulphur, carbon mainly). In that case it is obvious that a vibration of the molecule can easily stimulate a vibration of the contacts. However, in many experimental setups of interest, the contacts are made of gold that means that the ratio between the masses of gold atoms and the sulphur junction atoms of the thiol group is very large. It is possible to assume that the atoms in the gold are frozen in their equilibrium positions.

Finally some words must be spent about the modeling of the external bias. The effect of the voltage is equivalent to the one of an external electric field. The bias drops linearly in the device regions, the effect of polarization induced by charge arrangements is neglected. This effect, that in return changes the bias drop profile, can be included only by a full treatment of the Poisson equation.

5.2 The scheme of the device and the open boundary conditions

The real system which is simulated in the code looks like the one depicted in Fig. (5.1). The device region is formed by the molecule (M) plus the two leads (L). For metal contacts, due to the good charge screening, the leads reduce to a couple of layers of atoms. Periodic boundary conditions must be used to ensure that the principal layers (PL) of the electrodes behave like in a bulk. The periodic boundary conditions in the direction of the current produce problems when a real bias is applied between the two contacts. So, the periodicity in that direction must be used only for the evaluation of the contacts self-energy and discarded after for the calculation with the bias applied.

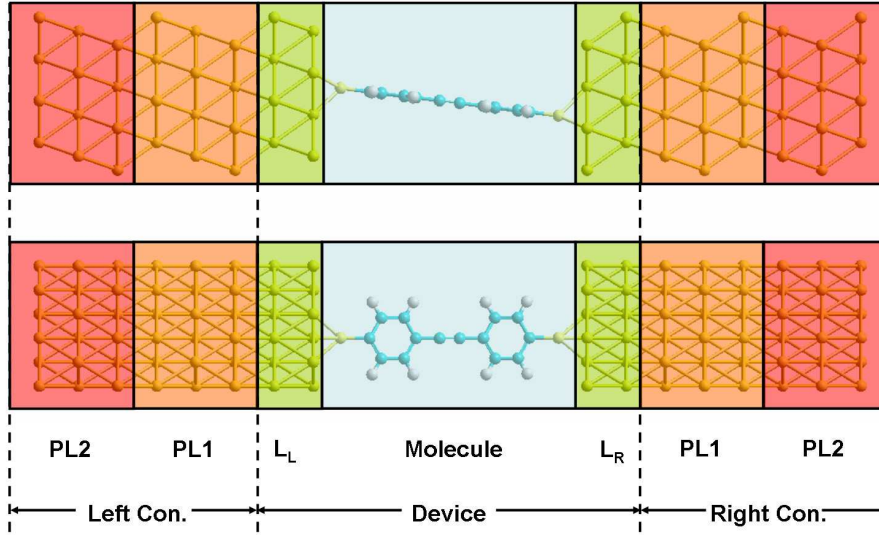


Figure 5.1: A view of a typical molecular electronic device. In the picture different regions can be recognized, the molecular (M) and the surfaces or leads regions (L) which together form the device region (D). The two semi-infinite contacts (C_L and C_R), the charge reservoirs, are represented by two chunks of the real electrodes. This chunks are formed by two principal layers (PL) each. The PLs are the basis to evaluate the self-energies for the open boundary conditions.

The partitioning of the system as shown in the figure is reflected in the total DFTB Hamiltonian matrix as:

$$\mathbf{H}'_0 = \begin{pmatrix} \mathbf{H}_D & \mathbf{J}_{DL} & \mathbf{J}_{DR} \\ \mathbf{J}_{DL}^\dagger & \mathbf{H}_L & 0 \\ \mathbf{J}_{DR}^\dagger & 0 & \mathbf{H}_R \end{pmatrix} \quad (5.2)$$

where the three diagonal blocks are the Hamiltonian parts for the device, left contact and right contact respectively and the off-diagonal terms are the coupling between the three.

Clearly, there is no coupling between the two contacts directly, this ensures that the self-energies for the contacts are two independent contributions.

The task to evaluate the self-energies is fundamental in transport calculations. The two self-energies represent a sort of equivalent potential, principally located in the junctions between the device and the contacts, which record all the perturbation effects induced by the semi-infinite contacts. To evaluate the self-energies we can expand the Dyson's equation for the zeroth order retarded propagator in matrix form

$$(\varepsilon\mathbf{S} - \mathbf{H})\mathbf{G}_0^r = \mathbf{1} \quad (5.3)$$

where $\varepsilon = (E + i\eta)$ and η is an infinitesimal positive quantity. We can expand the latter equation

$$\begin{pmatrix} \varepsilon\mathbf{S}_D - \mathbf{H}_D & \varepsilon\mathbf{S}_{DL} - \mathbf{J}_{DL} & \varepsilon\mathbf{S}_{DR} - \mathbf{J}_{DR} \\ \varepsilon\mathbf{S}_{DL}^\dagger - \mathbf{J}_{DL}^\dagger & \varepsilon\mathbf{S}_L - \mathbf{H}_L & 0 \\ \varepsilon\mathbf{S}_{DR}^\dagger - \mathbf{J}_{DR}^\dagger & 0 & \varepsilon\mathbf{S}_R - \mathbf{H}_R \end{pmatrix} \begin{pmatrix} \mathbf{G}_{D,0}^r & \mathbf{G}_{DL,0}^r & \mathbf{G}_{DR,0}^r \\ \mathbf{G}_{LD,0}^r & \mathbf{G}_{L,0}^r & \mathbf{G}_{LR,0}^r \\ \mathbf{G}_{RD,0}^r & \mathbf{G}_{RL,0}^r & \mathbf{G}_{R,0}^r \end{pmatrix} = \mathbf{1} \quad (5.4)$$

where we have emphasized the block structure of the total Green's function matrix for the entire system. However, we are interested in the device block $\mathbf{G}_{D,0}^r$ only. To get that part we can start from the propagators of the isolated contacts and device, assuming that we can ideally split the system in three non interacting parts:

$$\mathbf{g}_L^r = (\varepsilon\mathbf{S}_L - \mathbf{H}_L)^{-1} \quad (5.5)$$

$$\mathbf{g}_R^r = (\varepsilon\mathbf{S}_R - \mathbf{H}_R)^{-1} \quad (5.6)$$

$$\mathbf{g}_D^r = (\varepsilon\mathbf{S}_D - \mathbf{H}_D)^{-1} \quad (5.7)$$

The computation of the two free propagators for the semi-infinite electrodes is explained in more details in Appendix B. Expanding Eqn. (5.4) for the device block and manipulating them we get the three equations:

$$\mathbf{G}_{LD,0}^r = -\mathbf{g}_L^r(\varepsilon\mathbf{S}_{DL}^\dagger - \mathbf{J}_{DL}^\dagger)\mathbf{G}_{D,0}^r \quad (5.8)$$

$$\mathbf{G}_{RD,0}^r = -\mathbf{g}_R^r(\varepsilon\mathbf{S}_{DR}^\dagger - \mathbf{J}_{DR}^\dagger)\mathbf{G}_{D,0}^r \quad (5.9)$$

$$(\varepsilon\mathbf{S}_D - \mathbf{H}_D)\mathbf{G}_{D,0}^r + (\varepsilon\mathbf{S}_{DL} - \mathbf{J}_{DL})\mathbf{G}_{LD,0}^r + (\varepsilon\mathbf{S}_{DR} - \mathbf{J}_{DR})\mathbf{G}_{RD,0}^r = \mathbf{1} \quad (5.10)$$

Substituting Eqn. (5.8) and Eqn. (5.9) in Eqn. (5.10) we get at the end the following:

$$\begin{aligned} \mathbf{G}_{D,0}^r &= [\mathbf{E}\mathbf{S}_D - \mathbf{H}_D - (\boldsymbol{\varepsilon}\mathbf{S}_{DL} - \mathbf{J}_{DL})\mathbf{g}_L^r(\boldsymbol{\varepsilon}\mathbf{S}_{DL}^\dagger - \mathbf{J}_{DL}^\dagger) - (\boldsymbol{\varepsilon}\mathbf{S}_{DR} - \mathbf{J}_{DR})\mathbf{g}_R^r(\boldsymbol{\varepsilon}\mathbf{S}_{DR}^\dagger - \mathbf{J}_{DR}^\dagger)]^{-1} \\ &= [\mathbf{E}\mathbf{S}_D - \mathbf{H}_D - \boldsymbol{\Sigma}_L^r(E) - \boldsymbol{\Sigma}_R^r(E)]^{-1}. \end{aligned} \quad (5.11)$$

The latter is the zero order Green's function with the self-energy for the open boundary conditions: $\boldsymbol{\Sigma}_{L(R)}^r$. The self-energies depend on the coupling between the device region and the contacts and on the free propagators of the contacts. The advantage of using a linear combination of atomic orbitals basis set is particular evident here where we need that the coupling blocks do not extend too much, but are quite localized in the interface between contacts and device.

The two PLs in Fig. (5.1) are used to evaluate the free propagators of the contacts for the evaluation of the self-energies and after are not take into account anymore in the proceeding of the calculations. The self-energies in fact map the semi-infinite contacts on the device region. So fort all the matrices implemented for the calculation of the current have the dimension of the device region only.

5.3 The electron-phonon self-energies

For the electron-phonon interaction we can use the perturbation expansion starting from the zeroth order propagators including only the open boundary conditions. The approximation implemented here is the BA, in its consistent or not consistent form. The diagram representations are shown in Fig. (5.2, a), BA, and Fig. (5.2, b), SCBA.

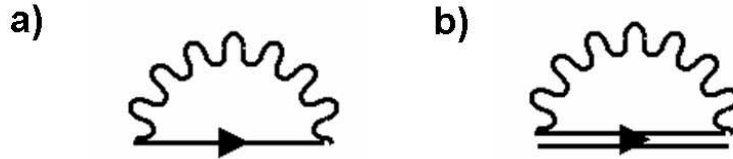


Figure 5.2: The diagrammatic representations of the self-energy for electron-phonon in Born approximation (a) or in self-consistent Born approximation (b).

In analytic form the lesser and greater self-energies are the following

$$\boldsymbol{\Sigma}_{ph}^{<, >}(E) = \sum_{\alpha} \frac{i}{2\pi} \int_{-\infty}^{\infty} \mathbf{M}^{\alpha} \mathbf{G}_0^{<, >}(E - E') \mathbf{M}^{\alpha} D_{\alpha,0}^{<, >}(E') dE' \quad (5.12)$$

for BA and

$$\Sigma_{ph}^{<, >}(E) = \sum_{\alpha} \frac{i}{2\pi} \int_{-\infty}^{\infty} \mathbf{M}^{\alpha} \mathbf{G}^{<, >}(E - E') \mathbf{M}^{\alpha} D_{\alpha,0}^{<, >}(E') dE' \quad (5.13)$$

for SCBA. The only difference in the two self-energies is that in one case we use the zeroth order propagators, and in the second case the full renormalized $\mathbf{G}^{<(>)}$ defined as

$$\mathbf{G}^{<, >} = \mathbf{G}^r [\Sigma_L^{<, >} + \Sigma_R^{<, >} + \Sigma_{ph}^{<, >}] \mathbf{G}^a. \quad (5.14)$$

The evaluation of the integration in Eqn. (5.12) and Eqn. (5.13) is quite expensive computationally. However, following the approximation that our phonon population is described by a collection of free oscillators, we obtain a simple formula for the phonon lesser and greater propagators,

$$D_{\alpha,0}^{>} = -2\pi i [(N_{\alpha} + 1)\delta(E - \omega_{\alpha}) + N_{\alpha}\delta(E + \omega_{\alpha})] \quad (5.15)$$

$$D_{\alpha,0}^{<} = [(N_{\alpha} + 1)\delta(E + \omega_{\alpha}) + N_{\alpha}\delta(E - \omega_{\alpha})]. \quad (5.16)$$

Under those approximations Eqn. (5.12) reduces to,

$$\Sigma_{ph}^{>} = \sum_{\alpha} (N_{\alpha} + 1) \mathbf{M}^{\alpha} \mathbf{G}^{>}(E - \omega_{\alpha}) \mathbf{M}^{\alpha} + N_{\alpha} \mathbf{M}^{\alpha} \mathbf{G}^{>}(E + \omega_{\alpha}) \mathbf{M}^{\alpha} \quad (5.17)$$

$$\Sigma_{ph}^{<} = \sum_{\alpha} (N_{\alpha} + 1) \mathbf{M}^{\alpha} \mathbf{G}^{<}(E + \omega_{\alpha}) \mathbf{M}^{\alpha} + N_{\alpha} \mathbf{M}^{\alpha} \mathbf{G}^{<}(E - \omega_{\alpha}) \mathbf{M}^{\alpha}. \quad (5.18)$$

The retarded and advanced propagators should be also renormalized taking into account that, until the matrices are symmetric, it is possible to use the identity

$$i(\Sigma_{ph}^{>} - \Sigma_{ph}^{<}) = i(\Sigma_{ph}^r - \Sigma_{ph}^a) = -2Im(\Sigma_{ph}^R) \quad (5.19)$$

the symmetry of the matrices in fact ensures that $(\Sigma_{ph}^r)^{\dagger} = (\Sigma_{ph}^a)^{*} = \Sigma_{ph}^a$. The identity (5.19) can be used to compute the imaginary part of the retarded self-energy for the electron-phonon interaction. The real part is neglected. Neglecting the real part we are neglecting all the polaronic effects induced by the interaction between the charge and its environment. The shift in the device spectrum is in fact zero, and the only effect of the vibration is a correction to the electron lifetime.

The lesser and greater self-energies for electron-phonon interaction represent, as for the equivalent quantities of the contacts, a flux of injecting and outjecting of charges, respectively. In fact the scattering processes can be seen as a third virtual contact, see Fig. (5.3), connected to the external phonon bath, with which it exchanges electrons. For charge conservation the total current through this third contact must be zero for every mode,

$$I_{\alpha} = \frac{2e}{h} \int_{-\infty}^{+\infty} dE Tr[\Sigma_{\alpha}^{<} \mathbf{G}^{>} - \Sigma_{\alpha}^{>} \mathbf{G}^{<}] = \int_{-\infty}^{+\infty} J_{\alpha}(E) dE = 0. \quad (5.20)$$

where $J_\alpha(E)$ is a density of current for energy unit.

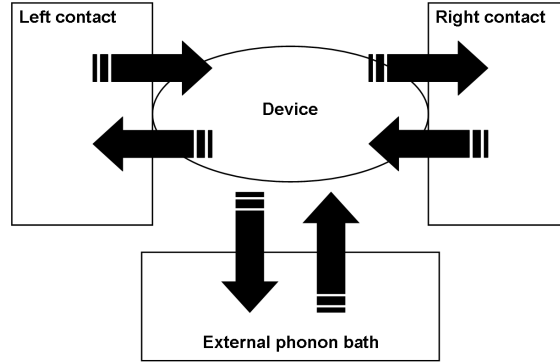


Figure 5.3: The schematic representation of the device connected to the two real electrodes and the third virtual contact which connects the device to the external bath.

In few words, this means that for every charge that enter in the virtual contact, another one must come out. However, the energy of the two charges is not the same, but differs of the value $\pm\omega_\alpha$ depending if it is describing an absorption or an emission process. This means that also if the current I_α is null, the power dissipated is not:

$$P_\alpha = \frac{1}{e} \int_{-\infty}^{+\infty} E J_\alpha(E) dE \neq 0. \quad (5.21)$$

To evaluate the power dissipated by every mode of vibration the Meir-Wingreen equation is invoked,

$$P_\alpha = \frac{2}{h} \int_{-\infty}^{+\infty} dE E (Tr[\Sigma_\alpha^< \mathbf{G}^> - \Sigma_\alpha^> \mathbf{G}^<]) \quad (5.22)$$

where $\Sigma_{ph}^<,> = \Sigma_\alpha \Sigma_\alpha^<,>$.

5.4 Computation of the electron-phonon couplings

As in most studies of vibronic coupling effects in molecular electronic, the small amplitude of vibrational motion is usually invoked to approximate the electron-phonon couplings, see [88]. In this case we can reduce the vibronic coupling to the expansion up to the first order of the Hamiltonian of the device respect the displacements of the ions along every normal mode of vibration α :

$$M_{ij}^\alpha = \sum_N \sum_\beta \sqrt{\frac{\hbar}{2m_N \omega_\alpha}} \langle i | \frac{\partial \hat{H}_D}{\partial R_{\beta,N}} | j \rangle e_{\beta,N}^\alpha \quad (5.23)$$

where N runs over all the nuclei, β over the three cartesian coordinates, m_N is the mass of the N^{th} nuclei, ω_α the frequency and $e_{\beta,N}^\alpha$ the proper mode eigenvector element. The expansion of the Hamiltonian can be further developed:

$$\langle i | \frac{\partial \hat{H}_D}{\partial R_{\beta,N}} | j \rangle = \frac{\partial \langle i | \hat{H}_D | j \rangle}{\partial R_{\beta,N}} - \langle i' | \hat{H}_D | j \rangle - \langle i | \hat{H}_D | j' \rangle \quad (5.24)$$

where $\langle i' | \equiv \partial \langle i | / \partial R_{\beta,N}$ represents the change in basis orbitals with displacements, and using the identity

$$1 = \sum_{ij} |i\rangle (\mathbf{S}^{-1})_{ij} \langle j| \quad (5.25)$$

where \mathbf{S} is the overlap matrix, we get

$$\langle i | \frac{\partial \hat{H}_D}{\partial R_{\beta,N}} | j \rangle = \frac{\partial \langle i | \hat{H}_D | j \rangle}{\partial R_{\beta,N}} - \sum_{nl} \langle i' | n \rangle (\mathbf{S}^{-1})_{nl} \langle l | \hat{H}_D | j \rangle - \sum_{nl} \langle i | \hat{H}_D | n \rangle (\mathbf{S}^{-1})_{nl} \langle l | j' \rangle \quad (5.26)$$

The terms $\langle i' | n \rangle$ can be evaluated numerically computing the first derivative of the overlap matrix elements $\partial S_{in} / \partial R_{\beta,N}$ using the unperturbed and deformed geometries. Substituting Eqn. 5.26 in Eqn. 5.23 we get the final form of the electron-phonon coupling matrix elements:

$$M_{ij}^\alpha = \sum_N \sum_\beta \sqrt{\frac{\hbar}{2m_N \omega_\alpha}} \left(\frac{\partial H_{ij}^D}{\partial R_{\beta,N}} - \sum_{nl} \frac{\partial S_{in}}{\partial R_{\beta,N}} (\mathbf{S}^{-1})_{nl} H_{lj}^D - \sum_{nl} H_{in}^D (\mathbf{S}^{-1})_{nl} \frac{\partial S_{lj}}{\partial R_{\beta,N}} \right) e_{\beta,N}^\alpha \quad (5.27)$$

The importance to retain all the matrix elements is related to the fact that the inelastic current can be strongly affected by motion that changes the overlap between different sites. For example when two neighbor atoms in a molecular structure are oriented so that they lie along the tunneling direction, a modulation of their distance can dramatically affect the inelastic current.

5.5 The flowchart of the code

The final implementation of the code is shown in the flowchart in Fig. (5.4). After the relaxation of the geometry, the DFTB code is used to compute the Hamiltonian \mathbf{H}'_0 for bare electrons in the whole system without phonons, the modes of vibration of the device (frequencies and eigenvectors) and the overlap matrix \mathbf{S} . Before starting the evaluation of the current a calculation at zero bias is done to evaluate the electron-phonon coupling matrices \mathbf{M}^α . The matrices are stored to be used later.

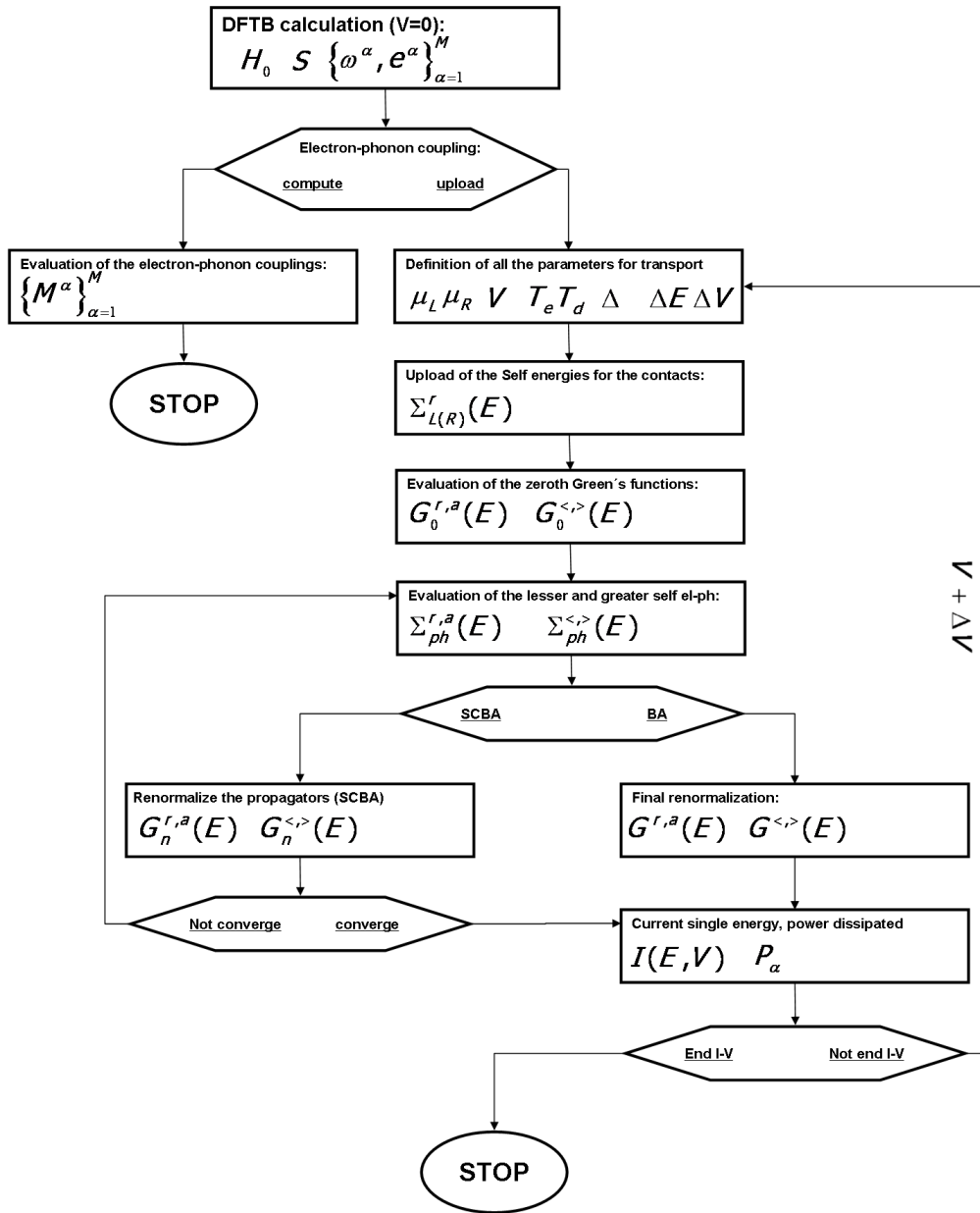


Figure 5.4: Flowchart of the code.

Now, it is possible to start the real calculation for the current. The very first step is the definition of a set of parameters, that means the chemical potential of the two contacts μ_L and μ_R , related to the Fermi energy of the contacts at equilibrium E_F . Other important parameters are the applied bias V and the temperature of the charge carriers T_e and the temperature of the device T_d . The former affects the electron distribution in the contacts, which in return changes the injection of charges in the device. The latter fixes the phonon population.

Concerning the numerical calculation there are two important parameters to set. One is the energy grid of linearly spaced points ΔE used for the numerical sampling. It should span a sufficiently large energy range while at the same time resolve the variations of all Green's functions, self-energies, etc. The second is a parameter Δ which sets a convergence criterium for the iteration procedure toward self-consistency. Finally, only in case the full I-V characteristic is computed, there is the voltage step ΔV . Every calculation computes a single current-voltage point and the power dissipation at that voltage. Using a script it is possible to repeat the calculation for many points and get the full I-V curve.

The self-energies for the contacts and the bias are further used to compute the zero order retarded Green's function,

$$[ES - \mathbf{H}'_0 - \Sigma'_L(E) - \Sigma'_R(E)]\mathbf{G}'_0 = \mathbf{1}. \quad (5.28)$$

Using the identity $\mathbf{G}^a = (\mathbf{G}^r)^\dagger$, the zeroth order of the lesser (greater) Green's function can be computed:

$$\mathbf{G}_0^{<, >} = \mathbf{G}'_0[\Sigma_L^{<, >} + \Sigma_R^{<, >}] \mathbf{G}_0^a \quad (5.29)$$

where

$$\Sigma_{L(R)}^{<} = i(n_{L(R)})\Gamma_{L(R)} = i(n_{L(R)})(-2)Im(\Sigma_{L(R)}^r) \quad (5.30)$$

$$\Sigma_{L(R)}^{>} = -i(1 - n_{L(R)})\Gamma_{L(R)} \quad (5.31)$$

and $n_{L(R)}$ is the Fermi function for the left (right) contact.

The zeroth order Green's functions are used to compute the self-energies for the electron-phonon interaction. At this stage lies the difference between BA and SCBA. If we are in BA the electron-phonon self-energies are used to renormalize the propagators, \mathbf{G}'_0 , $\mathbf{G}_0^{<}$ and $\mathbf{G}_0^{>}$ and the Meir-Wingreen equation is evaluated for that voltage point. In case we are in the SCBA, the new propagators are used to recompute the electron-phonon self-energies and the scheme is iterated until convergence is reached. Finally, the current, the power dissipation and the density of states are evaluated,

$$I(V) = \frac{2e}{h} \sum_{i=1}^N Tr[\Sigma_L^{<}(E_i)\mathbf{G}^{>}(E_i) - \Sigma_L^{>}(E_i)\mathbf{G}^{<}(E_i)]\Delta E \quad (5.32)$$

$$P_\alpha(V) = \frac{2}{h} \sum_{i=1}^N E_i \left(Tr[\Sigma_{ph,\alpha}^{<}(E_i)\mathbf{G}^{>}(E_i) - \Sigma_{ph,\alpha}^{>}(E_i)\mathbf{G}^{<}(E_i)] \right) \Delta E \quad (5.33)$$

$$\rho(E, V) = Tr[i(\mathbf{G}^r - \mathbf{G}^a)] = Tr[\mathbf{A}(E, V)]. \quad (5.34)$$

In case the number of modes included in the calculation is set to zero, the code reduces to evaluate the elastic current via a Landauer-Büttiker equation.

Power Dissipation at Low Temperature in Molecular Electronic Devices

The first application of the electron-phonon code is the evaluation of the power dissipated in molecular devices. Due to the approximations enlisted previously the simulations can evaluate dissipation at low temperature only.

The dissipation in molecular electronic devices is certainly a very important issue for the future of the field. In order to generalize the method it is fundamental to extend the technique of the gDFTB code also for higher temperatures. It is in fact clear that these kind of simulations will become fundamental in the future to test the stability of molecular junctions at work temperatures inside real electronic circuits. Recently an extension of the method, to take care of real non equilibrium population of phonons in the molecular region due to the coupling with the contacts, has been developed by Pecchia *et al.* [56].

Intuitively we can think that electron-phonon interaction is one of the main inelastic mechanism responsible for thermal relaxations of electrons in molecular junctions, its understanding is important for controlling not only the stability of the device, but also for other fundamental aspects. In fact, knowing where the dissipation is the highest in the molecule can suggest how to improve, with molecular substituents, the performance of the device.

In this Chapter is investigated the dissipation in octanedithiol molecules sandwiched between two gold electrodes.

6.1 Dissipation in alkanethiols

6.1.1 Geometry and vibrational modes

Although a simple and clear understanding of transport mechanisms has not been reached yet for most of the molecular compounds, transport in alkanethiols is essentially at a mature stage of experimental development. Such type of molecules align on Au surfaces via covalent S-Au bonds to form regular and stable self-assembled monolayers (SAMs). They are characterized by a large optical band gap (> 5 eV), making them very stable to photodegradation. The same large gap is responsible for a very low conduction via tunneling in Au-thiol-Au structures, giving good electrical stability. For the reasons above, it is not surprising that experiments of conduction through these compounds have been reproduced by many research groups [89, 90]. This paragraph is focused on octanedithiol between two (111) gold surfaces.

The gold atoms, composing the two contacts, are kept at fixed positions, corresponding to an ideal *fcc* crystal with Au-Au separation of 2.884 Å. First the octanedithiol saturated with a hydrogen termination was relaxed on top of one gold surface comprising six atomic layers. After this first step, the hydrogen was removed and the second Au surface was put, taking care that the Au-S distance obtained at the first interface was reproduced at the second interface. Then this system was relaxed again. Periodic boundary conditions were used in all these calculations. The final relaxed structure is shown in Fig. (6.1). Although the global minimum of the isolated octanedithiol is the one with the highest symmetry configuration, this symmetry is broken in the relaxed structure of the molecule attached to Au electrodes.

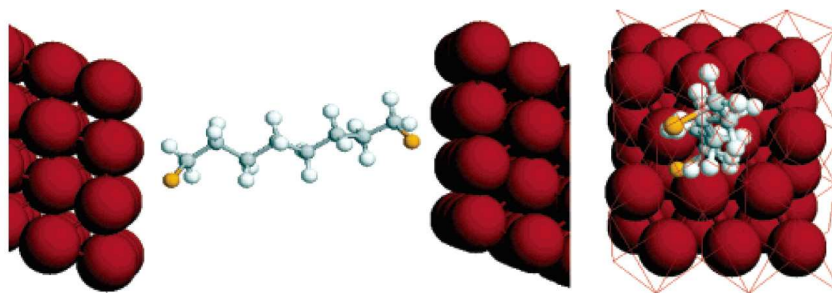


Figure 6.1: Diagram representing the relaxed atomic coordinates of the octanedithiol between Au contacts.

The vibrational frequencies are slightly affected by this, since many degeneracies are lifted. However, the differences in the whole spectrum of vibrations between the molecule in gas phase and relaxed on gold are within 20%, which is inconsequential for the present analysis. The S atom is found to form a bond with an energy minimum at the hollow site of the Au(111) crystal. Actually, the exact minimal configuration is not completely

understood, it is found with the sulfur atom slightly shifted from the hollow position, as reported in other ab-initio DFT calculations [91, 92]. The sulfur atom is found at 2.76 Å from the Au plane. After the relaxation of the molecular coordinates, obtained by imposing the atomic forces to be smaller than 10^{-4} a.u., the computation of the vibrational modes and frequencies was done.

6.1.2 Power dissipation in the molecule

While crossing the system, the electrons interact with the molecular ionic vibrations from which they can be inelastically scattered. In the present context the assumption was made that the metal ions do not move; henceforth, the electron-phonon scattering within the leads is neglected. This is a reasonable approximation given the very large difference in atomic masses between the Au atoms and the organic elements. It is clear that this assumption must be relaxed if we handle different kind of contacts, like silicon contacts.

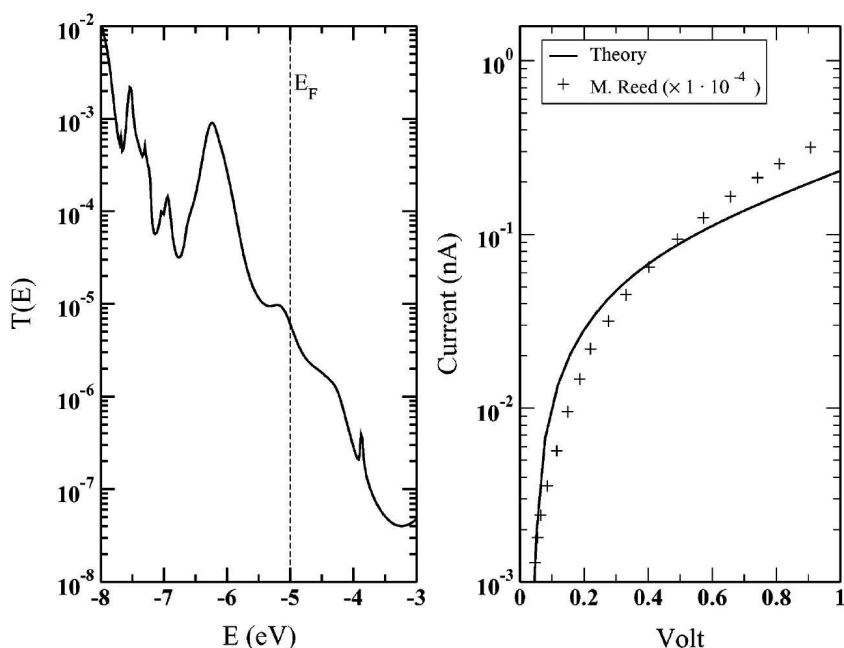


Figure 6.2: (left) Tunneling probability as a function of injection energy across a molecule of octanethiol. The Fermi energy corresponds to the Au contacts. (right) The computed I-V characteristics of the system (solid line) compared to experimental results (see [90]).

The separation between the molecular and the contact regions is obtained by two leads composed by three layers of gold atoms representing the metal surfaces that have been treated as to be part of the molecular region. Because of the short range of the atomic orbital interactions and since the Au atoms do not move, such three layers ensure that the contact and electron-phonon self-energies act on orthogonal subspaces of the Hamiltonian

matrix. In this calculation the Born approximation (BA) was applied for the calculation of the phonon self-energies. After that a self-consistent solution (SCBA) was done for comparison.

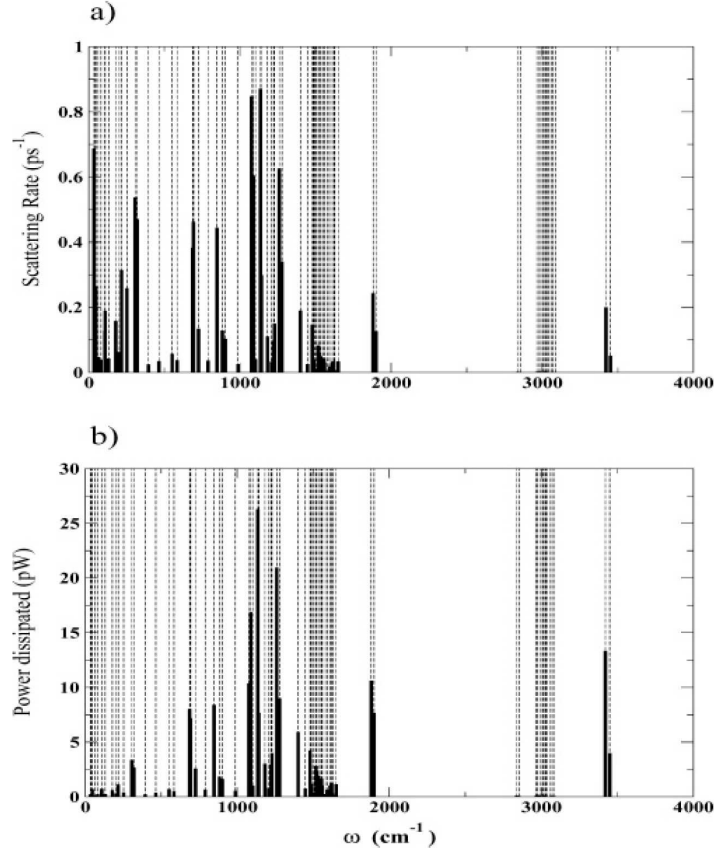


Figure 6.3: Calculated (a) Scattering rate and (b) power dissipated for each vibrational mode.

Since I am mainly interested on inelastic phonon emission, the approximation of the phonon self-energy to be purely imaginary, neglecting the shift of the van-Hoove singularities (i.e., essentially neglecting energy shifts due to polaron-like states), is reasonable. This assumption is valid since the molecular levels are far from the relevant range of injection energies and therefore the small shift will not modify appreciably the tunneling current. In any case, the BA is valid in the small electron-phonon interaction limit and far from resonant situations where polaron effects should be taken into account. Using the mathematical machinery of the NEGF, the tunneling current through an alkylthiolate molecule, $\text{Au-S}(\text{CH}_2)_8\text{S-Au}$, has been computed. Applying the Meir-Wingreen equation to get the current we obtain the curve shown in Fig. (6.2). The current computed is compared to experimental data obtained by measuring the current through a SAM assembled within a nanopore [90].

The simulation has been performed on a single molecule connecting the two contacts, assuming that the SAM assembled in a lattice $(\sqrt{3} \times \sqrt{3})\mathbf{R}30^\circ$, from the measured

nanopore diameter of 45 nm, it is possible to estimate that approximately 10,000 molecules are sampled in parallel. Accordingly, the experimental measurements are scaled by a factor 10^{-4} in order to compare with the calculations. The order of magnitude of the tunneling current is predicted very well. This is important, particularly in relation to the absolute magnitude of the power dissipated in such system, as discussed later.

For each of the 78 modes, the contribution to the inelastic current at $T = 0$ K and for an applied bias of 2 Volts has been computed. At $T = 0$, the inelastic part of the tunneling probability is related to the net phonon emission rate by $\tau_{\alpha}^{-1} = I_{inel}^{\alpha}/e$, where the α index stands for the vibrational mode. This quantity is used as a measure of the electron-phonon strength and is used to compare the different modes. A summary of such computations is reported in Table (6.1) and in Fig. (6.3, a). The lowest vibrational modes correspond to oscillations of the carbon atoms in the backbone plane, resembling the first harmonics of a string, and rigid twist around the C-C bonds of large subunits involving two or more CH_2 groups.

ω	τ_{α}^{-1}	description	ω exp.
34.8	0.608	$(\text{CH}_2)_2$ twist	
106.9	0.127	$(\text{CH}_2)_2$ twist	
109.3	0.189	$(\text{CH}_2)_2$ twist	
178.8	0.157	$(\text{CH}_2)_2$ twist	
217.0	0.314	Au-S stretch	225 ¹ -
320.6	0.470	Au-S stretch	-255 ¹
687.5	0.383	S-C stretch	650-706 ²
693.6	0.462	S-C stretch	
848.1	0.444	CH_2 rock	715-925 ^{1,3}
1076.8	0.848	C-C stretch	1050 ¹
1136.2	0.871	C-C stretch	1120 ²
1222.8	0.097	CH_2 wag	1330 ³
1259.9	0.626	CH_2 twist	1265 ¹
1479.2	0.147	CH_2 twist	
1518.2	0.082	CH_2 scissor	1455 ¹
1881.0	0.243	C-C + H swing	
2976.5	0.002	C-H stretch	2860 ¹
3421.4	0.200	H-Au stretch	

Table 6.1: Summary of the most important calculated frequencies (cm^{-1}) of the octanedithiol, phonon emission rate (ps^{-1}), followed by a brief description of the mode and the typical experimental value, obtained by (1) HREELS [93], (2) Raman [94] or (3) IR [95].

The two sulfur atoms remain practically fixed or slide slightly over the gold surface. The frequencies of such modes are affected by large relative errors because they are sensitive to small differences in the atomic pair potentials and to the relaxed geometry. Furthermore, these modes are not easily accessible experimentally. We find that modes associated to internal twists of the C-C backbone involving the motion of $(\text{CH}_2)_2$ subunits are more

effective in scattering electrons. As expected, the Au-S stretching modes, which are found in the range between 250 cm^{-1} to 320 cm^{-1} , in agreement with experiments [90], give a large contribution to the electron-phonon scattering. Similarly, a large contribution is given by the C-S stretch modes, found around 690 cm^{-1} . The band of modes found between 1000 and 1100 cm^{-1} corresponds to C-C stretch modes. These give the largest contribution to the inelastic current. A large contribution comes also from the modes related to motions of the CH_2 modes, particularly rocking and twisting. Wagging and scissoring modes, instead, give a smaller contribution.

In the simulation there is also a non negligible signal from some vibrational modes that have not been discussed in experimental papers, since they are special to the Au-octanedithiol-Au system and are not seen in isolated molecules. In particular, two modes around 1900 cm^{-1} (0.23 eV) are associated with a slight rotation of the C-S bond, a stretch of the C-C bonds involving the motion of the C at position close to sulfur, and a pronounced swing of the H atom closest to the gold surface. Another mode affecting the inelastic current is related to the oscillation of the hydrogens closest to the Au surfaces. Such modes could be seen as a Au-H stretch and are found at a frequency of 3400 cm^{-1} (0.42 eV).

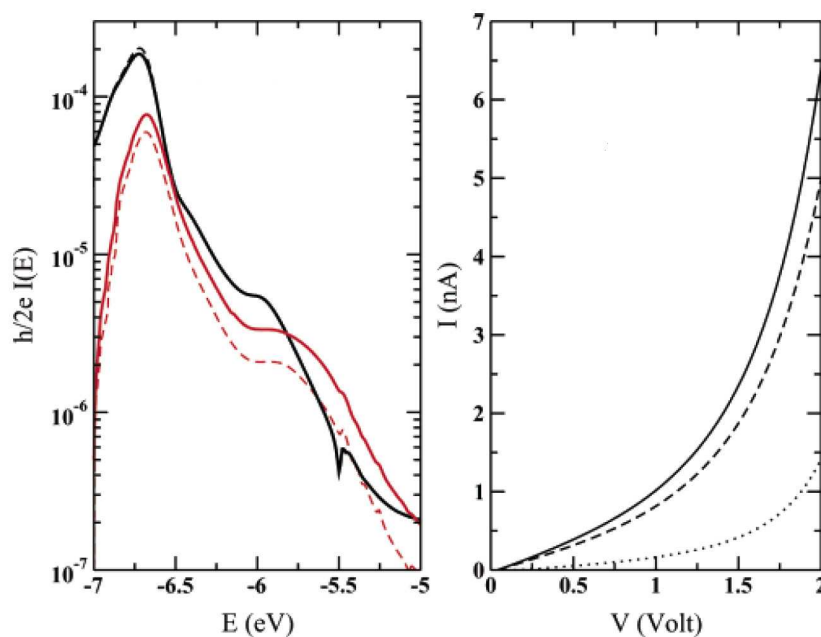


Figure 6.4: (left) Tunneling probability as a function of injection energy across a molecule of octanedithiol. The contribution of the inelastic (dashed) and elastic (solid) tunneling current are shown. The black curves are the first-order BA, the red ones are the SCBA. (right) The SCBA I-V characteristics of the system. The continuous line is the total current, the broken line is the elastic component and the dotted line the inelastic component.

The 34 modes giving an inelastic rate greater than 108 ps^{-1} have been included for the calculation of the inelastic current. Figure (6.4) shows the elastic and inelastic contributions

to the total tunneling current resolved in energy for the bias of 2.0 V and the calculated I-V characteristics of the system. The peaks in the transmission function correspond to features of the surface density of states of gold. In Fig. (6.4) the first-order BA has been compared with the SCBA. It is important to remark that for this system the first-order Born approximation gives already an acceptable result and the self-consistent loop does not introduce substantial changes in the transmission probability in the relevant energy range. Differences are appreciably deep in the energy gap, where the transmission probability is already small and the total contribution to the current is negligible.

At this point it is possible to compute the amount of power dissipated in the molecule due to inelastic phonon emission. This calculation can be obtained by considering the virtual contact current. The power dissipated can be easily calculated by Eqn. (5.21). This quantity is the virtual contact current, simply representing the total current scattered from its original energy to a new one after phonon emission (or absorption). The calculation shows that the power dissipated in the octanedithiol is $W = 0.16$ nWatt (1 eV/ns) at 2 Volt of applied bias. It is interesting, however, to analyze the power dissipated in each vibrational mode, as shown in Fig. (6.3, b). This is not directly proportional to the emission rate, since the power dissipated depends on the phonon energy as well. As expected, the low frequency modes contribute little to the dissipation, despite the relatively large scattering rates. The modes giving the largest contribution are found in the band of C-C stretch modes, the C-S stretch, and the CH₂ rocking modes. Considerable power is also absorbed by the modes at 1900 and 3400 cm⁻¹, involving essentially movements of the hydrogens close to the Au surfaces.

Simulation of IETS in Alkanethiols

In this Chapter an application of the electron-phonon code to simulate Inelastic Electron Tunneling Spectroscopy (IETS) measurements is presented. The systems under investigation are self-assembled monolayers of alkanethiols between two gold electrodes [90]. At least three papers have investigated the IETS of alkanethiols on gold. First, a sophisticated theoretical method [96] was applied to varying length alkanethiols [42] to give results which reproduced experimentally observed odd-even effects with varying chain lengths. Second, by making use of a model based on perturbation theory [45] it was shown that it is possible to get informative predictions of IETS showing good agreement with experiment [97]. Third, a number of different geometries for alkanethiol binding were considered with an examination of the impact of this binding on the IETS [46]. Here, I continue from this work and look further at the dependence on molecular structure and how this relates to the understanding of IETS.

The Chapter is organized as follows: after an introduction about the calculation of the geometry and of the vibrational frequencies, the IETS spectrum is discussed. The analysis section is divided in four parts. First, it is shown the general features of the spectrum. Second, it is looked at the unambiguous assignment of this spectrum that is achievable through simulations. Third, it is examined the nature of the low-voltage conduction channel and its control of the IETS signal. Finally it is shown the nature of the vibrational modes that produce the IETS.

7.1 IETS approximation

IETS is defined as d^2I/dV^2 . To obtain d^2I/dV^2 we should take, from the Meir-Wingreen,

$$I(V) = \int_{-\infty}^{+\infty} J(E, V) dE \quad (7.1)$$

and derive two times respect the bias. However, in IETS the bias applied is very small, so that we can consider that the density of current is independent from the bias: $J(E, V) \approx J(E)$. Moreover, for small electron-phonon coupling the integration limits reduce to the chemical potentials of the two contacts. Considering one of the contact as the reference one, we get:

$$I(V) \approx \int_{E_F}^{E_F+eV} J(E) dE = \int_{E_F/e}^{E_F/e+V} eJ(e\xi) d\xi \quad (7.2)$$

where it has been made a simple variable substitution in the last equation: $e\xi = E$, with e the electron charge. The first derivative of the current respect to the bias becomes:

$$\frac{dI(V)}{dV} \approx eJ(eV) \quad (7.3)$$

Iterating the latter for the second derivative and with a further variable substitution $E = eV$, it is obtained

$$\frac{dI^2(V)}{dV^2} \approx e^2 \frac{dJ}{dE}. \quad (7.4)$$

This final relation has been used to generate the IETS. This approximation neglects the voltage dependence of the electronic structure, a property considered to be minimal at the low voltages considered.

7.2 The choice of binding site

The binding geometry of alkylthiol molecules chemisorbed (with terminal proton loss from sulfur during the adsorption process) on gold surfaces has received considerable attention in the literature [98, 99, 100, 101] without any clear conclusion. Calculations performed on flat Au(111) surfaces [102, 103] suggest different geometries from those resulting from thiol-induced surface reconstructions [82]. In this section I present results for a representative geometry which is consistent with recent experimental results [104].

In Chapter 6 was already discussed a geometry for octanethiol between two gold contacts. However, for the IETS simulation a new geometry has been computed. A different relaxation scheme was adopted to preserve the symmetry in the junction between molecule and gold at the two surfaces.

The geometry of the molecule in the junction is determined in two steps. First, an optimized geometry is obtained for chemisorbed octanethiol or in the case of the other chain lengths the monothiol of that alkane chemisorbed through the terminal sulfur to a top site on a single Au(111) surface; while experimentally it is likely that sulfur does indeed sit vertically above a gold atom, it is probable that it is some reconstructed surface instead of a pure (111) surface. Periodic boundary conditions are used, with the chemisorbed molecules sufficiently far apart to be considered isolated [a $p(5 \times 5)$ unit cell].

The geometry for the full electrode-molecule-electrode system was then generated by

symmetrizing about a point of inversion between the central bond of the alkane chain to give a chemisorbed alkanedithiol bound to two cofacial Au(111) surfaces. Optimized geometries for octanedithiol in two slightly different local minima are shown in Fig. (7.1). The lowest-energy structure has the octane backbone at a tilt angle of 28° (from the Au surface normal), reducing to 18° for the other. These values differ significantly from what has been reported experimentally [105, 106, 107] for condensed monolayers, supporting the proposal that this property is controlled by interchain and solvent interactions. Detailed structures for molecules sandwiched between two electrodes remain unknown.

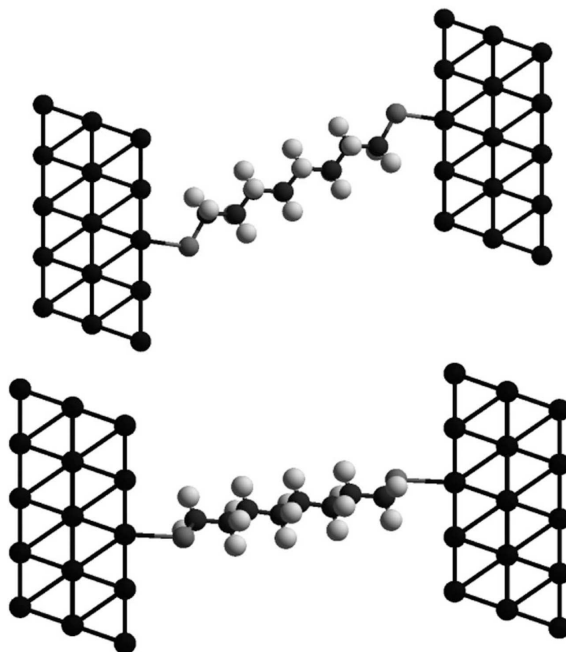


Figure 7.1: Two optimized geometries of octanedithiol between the two electrodes. The top geometry is the lower-energy minima of the two.

7.2.1 Atomic partitioning of the system

In the case of highly conducting conjugated molecules it is necessary to include a number of gold atoms in the extended molecule in order to accurately calculate the conductance of these systems. If no gold atoms are included in the extended molecule the self-energies do not shift and broaden the molecular states sufficiently to accurately model the coherent conduction channels that link the interface regions of the real semi-infinite systems. While the inclusion of a large number of gold atoms in the junction region significantly enhances the calculation of coherent transport, it does so by introducing a discrete approximation to the notionally continuous distribution of the low-voltage interface to interface conduction channels.

While the effects of excluding the interface region may be more important for conduction through conjugated molecules, much smaller effects are expected for alkanethiols. The smaller band gap HOMO-LUMO in conjugated systems means that the conductance varies significantly depending upon how the system is partitioned as even a slight shift in the molecular energy levels is important for the conductance at low voltage.

For alkanethiols, however, the significantly larger band gap means that the exact character of the molecular energy levels at low voltage is not as important. Further, the IETS is, as would be expected, very sensitive to changes in the number of conducting channels available. In the low-voltage regime considered here (< 0.4 V) the density of coherent conduction channels should be voltage independent, as it only depends upon the gold density of states; it is the change in the number of accessible incoherent channels as the voltage increases that gives the IETS signal. This will produce a large and broad feature underlying the fine structure of the IETS signal. For this reason we do not include any gold atom in the extended molecule.

7.2.2 Correction of the DFTB vibrational frequencies

The DFTB method is known to overestimate harmonic frequencies [62] as do other theoretical methods. In order to have sufficient accuracy in the calculated spectra to confirm experimental assignments for observed peaks, it is necessary to correct the DFTB frequencies with a scale factor λ . This factor is generated for a gas-phase octanedithiol molecule by the procedure described by Scott and Radom [108] as

$$\lambda = \frac{\sum_i^{all} \omega_i^{theor} \nu_i^{exp}}{\sum_i^{all} (\omega_i^{theor})^2} \quad (7.5)$$

where ω_i^{theor} and ν_i^{exp} are theoretical harmonic and experimental frequencies, respectively. In this case, however, due to the lack of experimentally assigned gas-phase frequencies for the octanedithiol, the experimental frequencies were substituted with B3LYP6-31g(*d*) frequencies calculated using GAUSSIAN 03 which had first been corrected with the relevant scale factor. This gave a scale factor of 0.913 for the DFTB frequencies. Implicit in this procedure is the assumption that the majority of the error in the calculated frequencies arises due to intrinsic limitations in the electronic-structure methodology rather than with the specific treatment of the interaction of the molecule with the gold surfaces. All frequencies presented in this IETS spectrum, as well as all figures, have been corrected with this scale factor.

7.3 Discussion of the IETS simulations

The observed and calculated IETS of chemisorbed octanedithiol are shown in Fig. (7.2) as a function of the applied voltage, 0.1 V corresponds to 806.5 cm^{-1} vibrational wave number. The calculated spectrum is obtained from the low-energy structure shown in

Fig. (7.1). Both spectra depict a variety of well-resolved peaks covering the vibrational energy range, but they differ in terms of the spectral base line and the band shapes.

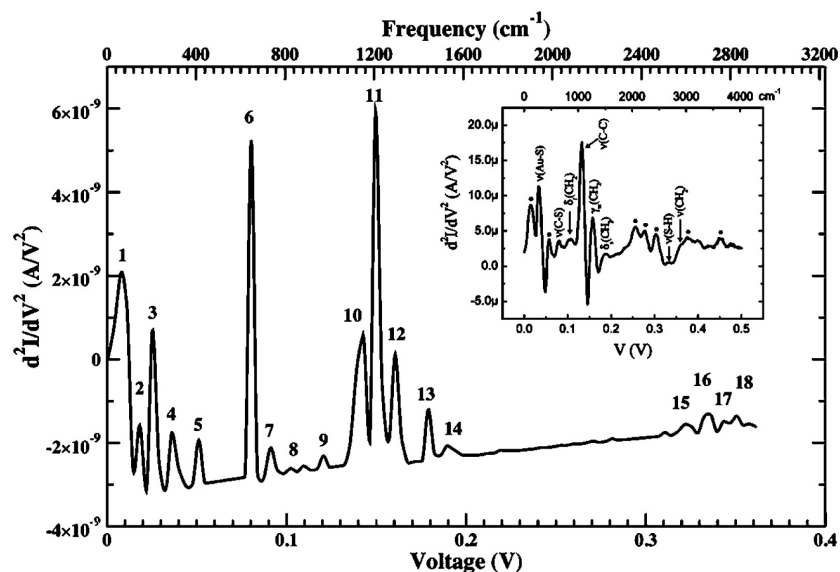


Figure 7.2: The calculated IETS for octanedithiol between two gold electrodes with the experimental results from ref. [90] shown in the inset. Numbered peaks are assigned in Table (7.1).

A close inspection of the figure shows that the observed and calculated peaks occur at similar voltages, and, while significant differences between the observed and calculated intensities are apparent, the number of resolved bands is approximately the same. This facilitates the assignment of the observed spectra, as discussed in detail later. The accuracy of the calculated band positions and intensities depends most significantly on the accuracy of the DFTB method used to calculate the electronic and nuclear structure. While in general density-functional tight-binding calculations such as these perform very well for the calculation of geometries and vibrational frequencies, latter improved by the use of the scale factor, errors in calculated energy levels do arise. As the intensities of calculated IETS bands depend significantly on the values for the energy levels, lower accuracy is, in general, expected for this property.

Previously [90], the IET spectrum of octanedithiol has been assigned by comparison of the observed bands with vibration frequencies obtained by IR spectroscopy, Raman spectroscopy, and HREELS. This assignment is not a straightforward process as the other techniques have specific selection rules, unlike IETS. It has been observed previously that in IET spectra both IR-active modes and Raman-active modes can be seen as well as additional modes, although not *all* IR-active or Raman-active modes may be seen. The experimental assignment is indicated in the inset of Fig. (7.2) and comprises eight firmly assigned molecular vibrations as well as seven tentative assignments, marked “*”, to vibrations in the surrounding Si_3N_4 matrix. For the calculated spectrum shown in Fig. (7.2), simple assignments arise for all bands except for that labeled 1, and these are given in Table (7.1) where they are compared to the experimental assignments.

Calculated spectrum				Experimental spectrum		
Peak	Volt. (V)	ω (cm ⁻¹)	Assignment [†]	Volt. (V)	ω (cm ⁻¹)	Assignment
1	0.007	61	Many modes			
2	0.018	151	C-C-C scissor	0.015	121	*
3	0.025	204	Au-S stretch	0.033	266	Au-S stretch
4	0.036	302	S-C-C scissor			
5	0.051	424	C-C-C scissor	0.058	468	*
6	0.080	648	C-S stretch	0.080	645	C-S stretch
7	0.091	737	CH ₂ 2 in-plane rock			
8	0.102	825	CH ₂ in-plane rock (all)	0.107	863	in-plane rock
9	0.120	972	CH ₂ in-plane rock (all)			
10	0.142	1149	C-C stretch (cent.)	0.133	1073	C-C stretch
11	0.150	1208	C-C stretch (ext.)			
12	0.161	1296	CH ₂ twist (ext.)	0.158	1274	CH ₂ wag
13	0.179	1444	CH ₂ scissor (ext.)			
14	0.189	1525	CH ₂ scissor (cent.)			
15	0.321	2593	C-H stretch sym. (ext.)			
16	0.333	2688	C-H stretch asym. (cent.)			
17	0.343	2769	C-H stretch sym. (ext.)			
18	0.348	2806	C-H stretch asym. (cent.)	0.357	2879	C-H str. asym.

Table 7.1: The assignment of the peaks observed in the calculated IET spectra shown in Fig. (7.2). †: the labels (ext.), (cent.) and (all) stand for “extremities”, “central” and “all the molecule” respectively and are related to the localization of the mode of vibration.

Of the seven bands originally tentatively assigned to the Si₃N₄ matrix, five occur above 0.25 eV (2000 cm⁻¹) in a region in which the molecule does not have vibrational fundamentals. Any molecular band in this region would thus have to be a combination or overtone band. As such bands have never been observed to produce a strong signal in IET spectra [109], they are explicitly excluded from the electron-phonon coupling and hence the calculations provide no new information concerning the nature of these five observed modes. However, a variety of molecular peaks are predicted in regions (0.01 and 0.07 V) of the other two peaks that were not originally authoritatively assigned. The calculations thus suggest new assignments of these peaks.

Of the eight bands positively identified experimentally, seven correspond to calculated bands of the same nature, as indicated in Table (7.1); however, the calculations enhance these assignments by providing more specific information. For example, the most intense band in the observed and calculated spectra was originally assigned as a C-C stretch but the calculations indicate that the various C-C stretches within octanedithiol should have different frequencies and very different intensities, allowing the observed band to be assigned to C-C stretch modes at the extremities of the alkane chain. Similarly, the calculations reveal that the observed CH₂ stretch and rock modes are localized on the extremities. These conclusions are obtained following the examination of the IETS spectrum shown in Fig. (7.3) calculated at much higher resolution than the experimental spectrum.

Due to the effect of modulation broadening, high-resolution experimental spectra with

36 clearly identifiable modes will be difficult to obtain and hence calculations offer a long-term solution to the assignment problem of IETS. While the calculations indicate that the vibrational modes at the center and extremities of the molecule are distinguishable, they also indicate that most of the major peaks shown in low resolution in Fig. (7.2) actually arise from multiple modes as indicated in Fig. (7.3).

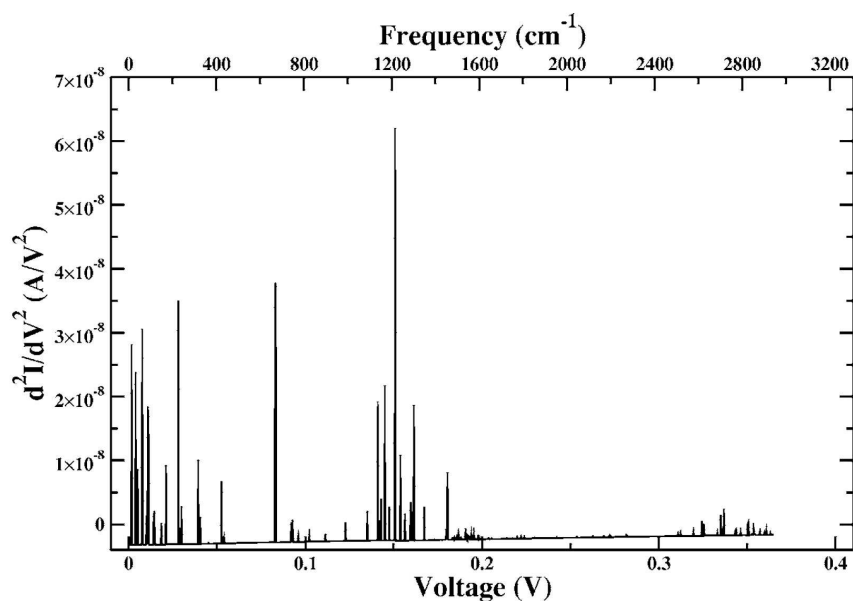


Figure 7.3: The calculated IET spectrum at high resolution showing the contribution of individual modes to the broad peaks observed experimentally.

For all bands other than peak 1, all contributing modes are modes of the same type so it is possible to assign the peaks. For peak 1, the contributions are from *different* types of modes associated with translation of the carbon chain in the two directions parallel to the gold surface, the rotation of the molecule about the chain direction, and some asymmetric combinations of these modes about the center of the molecule.

The only region of the spectrum where the calculated assignment is not fully consistent with the experimental assignment is part of the *fingerprint region* (1200-1500 cm^{-1}) in which a variety of different types of modes occur such as CH_2 wags and CH_2 twists that often mix strongly with each other. The most prominent disparity is the assignment of peak 12 as a CH_2 twist in the calculated spectrum compared with the CH_2 wag assigned at 1274 cm^{-1} in the experimental spectrum. Throughout this region DFTB predicts a strong Duschinsky rotation between the modes, and in addition DFTB and B3LYP calculations differ significantly in their perception of the mixing for gas-phase octanedithiol.

While all calculations predict the IETS signal for the twist to be stronger than that for the wag, I find that the calculated twist frequency is very sensitive to interface geometry, leading to the possibility that structural irregularities wash out the signal from the twist. Computationally, this makes a definitive assignment impossible without detailed knowledge of the experimental structure, independent of the reliability of the method. Also,

the arguments used to make the original experimental assignments of the IR and Raman spectra may need to be reexamined.

7.3.1 Nature of the orbitals controlling conduction and IETS

IETS is controlled by the electron-phonon couplings $M_{\mu\nu}^{\alpha}$ between atomic orbitals μ and ν in mode α as well as the Green's function matrices lesser and greater that also act to determine the coherent electron transport. Shown in Fig. (7.4, a) is the coherent transmission $T(E)$ calculated using the Landauer formalism as in Eqn. (2.37) where the contact self-energies are related to the $\Gamma_{L(R)}$ matrices.

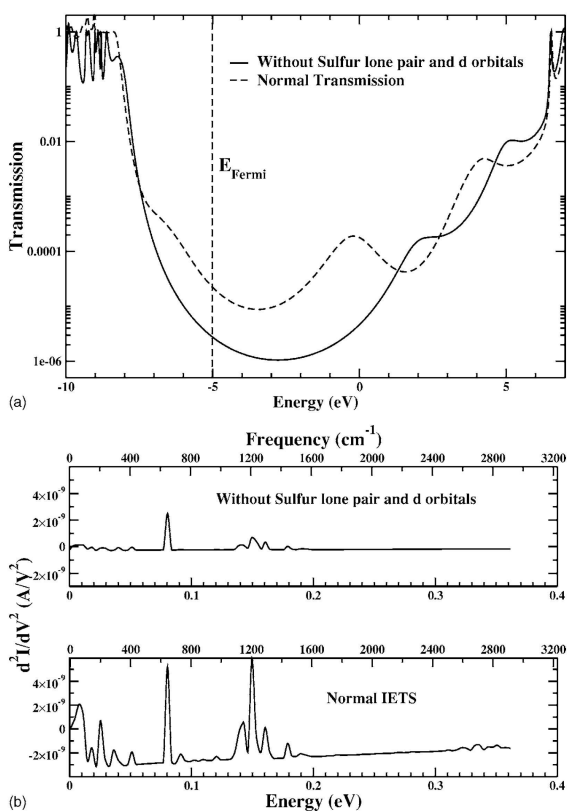


Figure 7.4: The transmission (a) and IETS (b) for the normal system and the system where the sulfur lone-pair and d orbitals have been shifted to very high energy, showing that these are the dominant conduction channels at low voltage.

The peaks in this function correspond to conduction channels embodied within $\mathbf{G}_0^{<(>)}$; the general nature of such channels is quite complex and their effects on IETS will be described in detail in Chapter 8. Here, I show that broad features can be identified with conduction involving the sulfur lone-pair and valence d orbitals by taking the DFTB-calculated Hamiltonian matrix in the Löwdin orthogonalized atomic-orbital basis and artificially shift-

ing these orbitals to remote energies. The modified coherent transmission is also shown in Fig. (7.4, a) and it is evident that there is a dramatic lowering of the transmission near -4 eV, attributable to the lone-pair orbitals, and 0 eV, attributable to the d orbitals. It is hence clear that at the Fermi energy of the electrodes these orbitals constitute the primary conduction channel(s).

As alkanethiols have very large band gaps (HOMO-LUMO gap) these primary conduction channels at low voltage are not resonant channels with a large amount of molecular character, as they are for, say, 1,4-benzenedithiol, but rather are states that are primarily localized on the electrodes with a small amount of molecular character. This is effectively a conduction through the wings of the probability distribution functions representing the molecular orbitals; these functions show significant broadening owing to their coupling with the electrodes. Figure (7.4, b) shows the calculated IETS for both the original and modified Hamiltonians, and it is evident that the majority of the IETS signal disappears when the sulfur lone pair and d orbitals are shifted to very high energy.

Interestingly, the peak in the IETS resulting from the C-S stretch mode does not decrease proportionately with the rest of the spectrum when the orbitals are removed. The reason for this is that this mode couples strongly with the high-energy transmission channel at ca. -8 eV associated with the C-S σ bond, the channel that produces the weak remnant transmission at the Fermi energy depicted in Fig. (7.4, a) after the removal of the other sulfur orbitals. Hence it is clear that the conduction channels that control the low voltage coherent transport *also* control IETS. The signal obtained in IETS thus arises as a result of energy loss from electrons in the low-voltage conduction channels as they excite the vibrational modes of the molecule.

7.3.2 Nature of the vibrations that produce IETS

As the low-voltage conduction channel dominates IETS, the peaks of highest intensity will be those associated with the vibrational modes that provide the greatest perturbation in the region where this channel has electron density. As the main conduction channels for octanedithiol have been determined to involve sulfur lone-pair and d orbitals as well as some contribution for the C-S sigma system, vibrations localized on the S and terminal C atoms are expected to be the most significant. It is this physical principle that underpins the previously mentioned assignment of the dominant IETS modes as modes involving the extremities of the bridging molecule.

This physical picture leads to the prediction that the IET spectra of alkanethiols will be very sensitive to changes in the binding geometry and less so to changes in the backbone of the chain. To test this hypothesis numerically, I calculate the IETS for alkanethiols of modified chain length and different binding site. Figure (7.5) shows the calculated current-voltage characteristics (left) and the corresponding IET spectra (right) for C₄, C₈, C₁₂, and C₁₆ alkanethiols.

The geometry optimizations for these molecules were performed so as to achieve similar binding configurations, and this is reflected in the similarity of the IETS features. The current decreases approximately exponentially with increasing length as is expected and as a result so does the magnitude of the IETS base line. Beyond the change in base line,

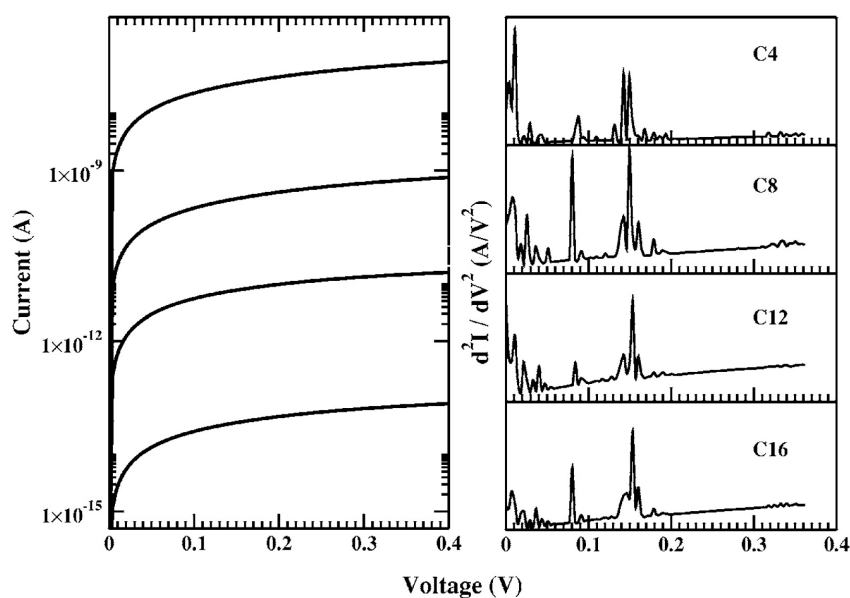


Figure 7.5: The simulated current vs voltage and IETS for C₄, C₈, C₁₂, and C₁₆ length chains.

however, the differences are slight and simply reflect the subtle variation in the calculated molecular binding geometry (for example, the slight rotation of the terminal CH₂ group). This result shows that the vibrational modes in the central region of the molecule do not contribute significantly to the IETS signal, as hypothesized.

This result is consistent with that found previously by Chen *et al.* [42] for the effect of chain length on IETS characteristics. In that work the low-energy modes (below 50 meV) were predicted to be very much smaller in magnitude than the other features, in contrast with the present results, however, the predicted length dependencies were similar. As the treatment of the interface region in this previous work was quite different in that the electrodes were treated with a jellium model, it can be concluded that the major conclusion concerning the significance of the terminal vibrations is found to be robustly obtained.

As there are many minima on the potential-energy surface for binding octanedithiol on gold it is possible to investigate two similar binding sites that feature the sulfur atoms bound directly above an Au site. The first geometry is the low-energy structure that has been used up to this point and the second is a higher-energy optimized geometry shown in Fig. (7.1). In this second structure the tilt angle to the Au surface normal is now 18°; and there is a greater twist in the alkane chain; both geometries are shown together in Fig. (7.1) for comparison.

Figure (7.6) shows the calculated IETS spectra for these two geometries, and these display qualitative differences that reflect the changes in the binding site in addition to the changes found in the magnitude of the observed current (evidenced in the IETS by the changes in the base line). The most significant change observed is the modulation of the intensities of the C-S and C-H stretches and CH₂ in-plane rock modes between the two ge-

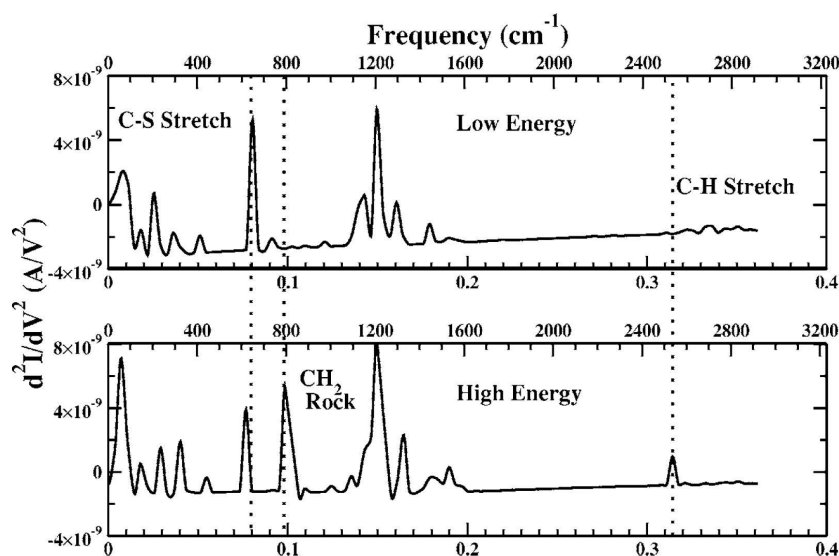


Figure 7.6: The calculated IETS for the two different binding sites corresponding to the two different geometries shown in Fig. (7.1) The modulation of the C-S stretch and C-H stretch modes reflects the changes in the geometry of the terminal CH_2 group with respect to the gold surface.

ometries. In the low-energy geometry we have the large C-S stretch peak corresponding to sensitivity to this vibrational mode as the molecular component of the conduction channel is predominantly sulfur density. Conversely, in the high-energy geometry with the greater twist angle in the alkane chain a hydrogen atom of the first CH_2 group is now in close proximity to the surface. This results in the molecular component of the conduction channel having significant density on this hydrogen atom in addition to the sulfur, and in turn the IETS signal shows sensitivity to the CH_2 in-plane rock and C-H stretch of the extremities.

7.4 Conclusions

The IETS of chemisorbed octanedithiol between two gold contacts shows to reproduce key features of the experimental spectrum for this molecule, including the verification of the major molecular vibrational modes involved. However, the calculations are shown to lead to increased specificity in the assignments and to new assignments. The previous experimental assignments were obtained by the comparison of the IETS results with those from other spectroscopies, but the different selection rules and chemical environments make this a difficult process. The calculations suggest that a number of the modes that were attributed to possibly coming from the Si_3N_4 matrix [90] may in fact have molecular character.

Further, the evidence of a mixing of modes with different symmetry in the fingerprint region suggests that the detailed assignment of this region may prove illusory without detailed knowledge of experimental structure. They show that for chemisorbed alkanethiols,

IETS is dominated by vibrational modes localized at the ends of the molecule, providing additional assignment information that is critical to the understanding of the nature of the process. It may be possible to verify these features of the assignment if higher-resolution spectra can be obtained, beyond the modulation-broadening limit, as such spectra are predicted to be able to discriminate in both frequency and intensity between central and terminal vibrational modes.

The calculations indicate that there is a strong correlation between the conduction channels that dominate the low voltage coherent conductance of alkanethiols and those that dominate IETS. These channels are shown to be dominated by the sulfur lone-pair and other orbitals, leading to the result that IETS is most sensitive to vibrations localized at the ends of the molecule. For conduction through conjugated molecules, the lower molecular band gap results in greater participation of the center region of the molecule in the conduction channel, and so the dominance of terminal modes is not expected to be as pronounced. For alkanethiols, however, the deduced sensitivity to the metal-molecule interface region indicates that IETS spectra should show considerable variation with subtle changes in binding site and small variations with increasing chain length, and these predictions are verified by the simulations.

Other calculations [46] of the IETS of octanedithiol have predicted significant differences in the relative intensities of the C-C and C-S modes to those shown in Fig. (7.2), most likely as the result of the different interface geometries and treatments used. While optimized structures were used in the calculations, many binding sites are possible on smooth gold surfaces ([82]), and many irregular binding sites are likely to occur in real metal-molecule junctions. Experimental spectra obtained in, say, nanopores involving thousands of molecules are likely to depict an ensemble of possibly very different junctions, making detailed interpretation difficult. The calculations are also approximate in that they do not allow the gold surface atoms to relax, nor do they include gold surface vibrational modes. Consequently, the predicted properties for terminal vibrational modes are not expected to be as accurate as those for the central modes. Hence, while IETS are predicted to show details revealing critical but largely unknown aspects of the alkanethiol-metal interface, the design of computations that can authoritatively unravel these features poses a major challenge.

The most striking feature of IETS results remains; this is the first technique to provide conclusive evidence that current flows through a molecule, as opposed to a metal filament.

The Role of Symmetry and Channels in Conduction

The analysis of IETS in Chapter 7 arises many questions. First, it was shown the difficulty of a clear assignment of the peaks in the IET spectrum. This is related to two facts: the uncertainty in the definition of the geometry of the molecule and the metallic surfaces from experiments data and the different selection rules shown by IETS. Second, from the analysis of the conduction in the octanedithiol molecule was clearly shown that only few “channels” conduce all the current which is inelastically scattered by the most relevant vibrational modes, and those channel can be partially related to some canonical molecular orbitals of the molecule. However, the canonical molecular orbitals are usually not a suitable set of channels for transport problems, due to the presence of the open boundary conditions, that means the coupling of the molecule with the contacts.

The present Chapter is focused on answering these two points. The Chapter is articulated as follows: in the first part it is shown how define a point group for the molecule between the electrodes. It is clear that starting from the molecule in gas phase, the effects of the contacts is to reduce the symmetry of the system in a subgroup of the original symmetry point group. The second part of the Chapter is devoted in the definition of channels for transport. These channels decompose the total current in a sum of non interfering contributions. Every channel can be labeled according to its irreducible representation from the reduced point group.

During this Chapter it is made use of the Landauer-Büttiker formalism, that means I am considering elastic current only. In Chapter 9 the formalism will be generalized to include also scattering processes in the full Meir-Wingreen equation. This will lead to an investigation of selection rules in IETS.

8.1 The definition of the symmetry of conduction

It is well known that one of the most powerful concepts to aid in understanding molecular properties is symmetry. As researchers today expend more effort to utilize molecular properties in single molecule electronic devices, it is important to understand how symmetry operates within these regimes.

Understanding the symmetry of a molecule carrying current is an important step in molecular electronics for resolution of issues such as whether there can be symmetry selection rules in IETS, or the means by which molecular orbitals influence conduction characteristics. These issues in turn feed back to experimental design, providing guidance for device characterization and synthetic targets. This section will show how symmetry operates within the standard conduction formalism of molecular electronics and from this illustrate the additional information that symmetry assignment provides concerning molecular conduction.

In order to describe the symmetry of molecular conductance, it is necessary to understand the relationship between the symmetry of each of the quantities within the Meir-Wingreen equation in terms of the geometric point group of the entire system. Assuming for simplicity the absence of an applied bias ($V = 0$), the first important consideration is that the self-energies $\Sigma_{L(R)}^r$ arising from the electrode-molecule interactions *do not* commute with all of the symmetry operators that define the point group of the bridging molecule. Moreover, the application of an electric field only increases the symmetry breaking.

First, a single electrode will couple strongly to one end of the molecule and weakly to the other. This results in the individual Σ_L^r and Σ_R^r matrices not having an end-to-end symmetry even if such symmetry is present in the geometric point group of the *full* electrode-molecule-electrode system. With end-to-end symmetry I mean that the symmetry of the self-energies cannot contain all the symmetry operations of the device point group which relate one end of the device to the other. Second, as $\Sigma_{L(R)}^r$ embody the interactions between the molecule and the left (right) electrode, the symmetry of these matrices embodies only the symmetry elements that are common to both the molecule and the electrode junction.

These two levels of symmetry breaking provide a natural framework to define the symmetry of conductance. The symmetry of the transmission through the full system can be defined exactly as the *conductance point group*; the symmetry operators that define this point group will commute with all quantities appearing in the NEGF formalism. Hence the conductance point group contains the common elements of the symmetries of Σ_L^r and Σ_R^r , called the *junction-conductance point groups*, as well as those of the geometric point group of the isolated molecule. Put another way, the conductance point group contains all the symmetry of the two electrodes and the molecule and also all the symmetry breaking interactions between the three.

While the conductance point group and the individual junction-conductance point groups are important as they describe molecular conductance within the NEGF formalism exactly, in practical applications the required precise junction geometries and electrode symmetries are likely to be unknown and/or uncontrollable [110]. However, the dominant symmetry breaking contribution in molecular conductance comes not from the details of the electrode geometry but from the loss of end-to-end symmetry which is a universal feature of

all $\Sigma_{L(R)}^r$ matrices. Consequently, I introduce a *molecular-conductance* point group comprising only the symmetry operators of the geometric point group of the *molecule* that do not interchange its two ends.

This is of practical utility as it allows the dominant symmetry contributions to the transmission through a molecule to be determined from knowledge of just the molecular geometry alone without need for knowledge of the details of the electrode binding. The disadvantage is that the molecular-conductance point group may not be an exact descriptor of the symmetry of transmission as it neglects the possible symmetry breaking contributions arising from the internal electrode geometries. However, I will show later that in the case of sulfur-gold binding this symmetry reduction either does not occur or is inconsequential from a practical standpoint.

8.1.1 Application to molecular system

The approach makes it possible to separate the different symmetry contributions to the conductance for a molecular system. To demonstrate this, calculations are performed for conduction through a 1,4-benzenedithiol molecule chemisorbed on two gold electrodes. Two binding configurations are considered: the bridge binding site where the sulfur atom sits above two gold atoms and the hollow binding site where the sulfur sits above three gold atoms. The molecule is defined as being the central $C_6H_4S_2$ moiety whose geometric point group is D_{2h} . The important difference between the two binding geometries is that the differing symmetry in the binding gold atoms makes the conductance point group C_s in the case of the hollow binding site, whereas the bridge binding site leads to a conductance point group of C_{2v} . Different interface geometries thus result in different conductance point groups. However, when the molecule is considered alone, the molecular-conductance point group is insensitive to the interface structure: it is C_{2v} independent of binding site and hence unambiguously determinable.

Figure (8.1) shows how the molecular-conductance point group is determined through examination of the symmetry operators of the D_{2h} point group of the $C_6H_4S_2$ fragment. Those operators shown in red—the center of inversion, the σ_{xy} plane, and the C_{2x} and C_{2y} axes—are not part of the molecular-conductance point group of C_{2v} , as only the σ_{xz} and σ_{yz} planes and the C_{2z} axis may possibly commute with $\Sigma_{L(R)}^r$.

It has been discussed previously that the impact of the electrodes on the molecular electronic structure is treated more precisely, with consequent improvements in numerical accuracy, when a number of electrode atoms are included with the molecule to form an “extended molecule”. This inclusion has ramifications on the molecular-conductance point group of the system, as now electrode atoms are included in the geometric point group under consideration. If the shape of the unit cell is chosen with care, a bridge binding site geometry will still have a molecular-conductance point group of C_{2v} ; however, a hollow binding site geometry can only have C_s symmetry.

For the bridge binding site, the zero-voltage transmission can thus be separated into the four different symmetry components, A_1 , A_2 , B_1 , and B_2 consisting of two σ and two π representations, as shown in Fig. (8.2) for the molecule alone (black curve) and an extended

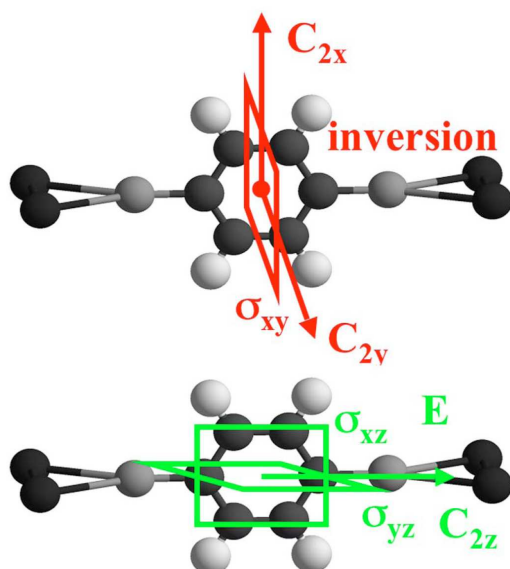


Figure 8.1: The symmetry operators that define the geometric point group of D_{2h} , those shown in green, are the operators present in the molecular-conductance point group of C_{2v} , while those shown in red reflect end-to-end symmetry and do not commute with $\Sigma'_{L(R)}$.

molecule with 25 gold atoms included on each side (red curve). This immediately yields an intuitive picture of conduction in this system that is not otherwise demonstrable. At very low energies (below -9 eV), conduction is dominated by transmission through the σ system with A_1 symmetry; however, in the range from -9 to 4 eV that includes all accessible energies, the dominant transmission is through the π system with B_1 symmetry. There is nothing surprising in this result; it just provides a formal basis for the general assumptions about the nature of the conductivity in conjugated systems of this kind. An interesting feature to note is that while the region of high transmission through the σ system does not lie in an energy range that is accessible using gold electrodes whereas that for the π system does, the transmission coefficients become large in both cases. This result accords with what is known from intramolecular electron transfer experiments [111] where it was seen that when systems are designed to make the σ system energetically accessible then high rates of electron transfer can be achieved over large distances.

Additionally, it is evident that the inclusion of electrode atoms in an extended molecule simply acts as a perturbation on the symmetry separated transmissions without changing their character. Hence including only the isolated molecule in the molecular component is a reasonable approximation for revealing the character of symmetry separated components of the transmission. This approximation facilitates the definition of a single conductance symmetry for a particular molecule, irrespective of the binding site.

The bridge binding site considered above is a special case in which inclusion of the gold atoms at the binding site does not lower the symmetry of the system. This results in the molecular-conductance point group being the same as the conductance point group. Gener-

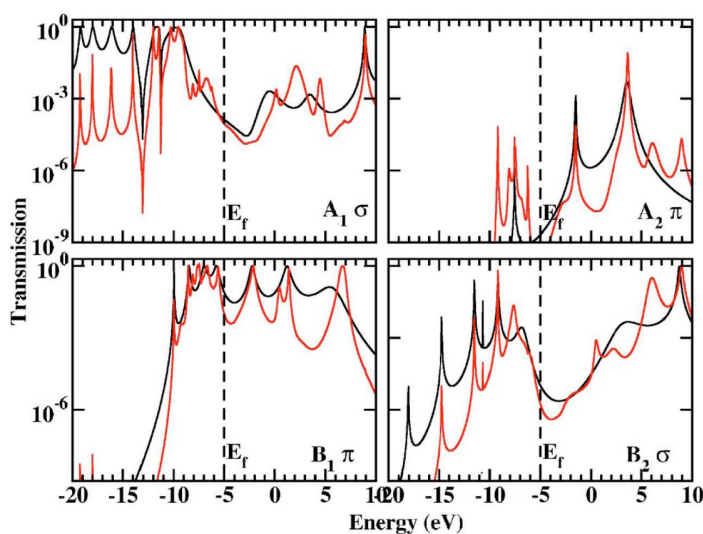


Figure 8.2: Symmetry separated components of the transmission through chemisorbed 1,4-benzenedithiol bound to the bridge site with two gold contacts. In each case the black curve is the transmission calculated without any gold atoms included in the extended molecule and the red curve results from 25 gold atoms being included on each side.

ally, however, this is not the case. The simplest illustration of this is again the chemisorbed 1,4-benzenedithiol bound this time to the hollow site. In this case the symmetry of the full system is now C_{2v} , and although the geometric point group of the central $C_6H_4S_2$ moiety is still D_{2h} , the conductance point group (defined by the common elements of the junction-conductance point group and the geometric point group) is no longer C_{2v} but C_s as the C_2 axis of the full system is not the electrode-molecule-electrode axis.

Figure (8.3) provides a comparison of the two ways of treating the symmetry of the system where no gold atoms are included in the extended molecule. First are the two symmetry components of the transmission through the molecule alone that arise, without approximation, as the system can be described using its C_s conductance point group (black curve). These results are compared with those obtained approximately by neglecting the terms in $\Sigma'_{L(R)}$ that break C_{2v} symmetry (green curve). While this approximation allows the conductance to be classified in terms of the A_1 , A_2 , B_1 , and B_2 representations of the C_{2v} point group, the A_1 and B_1 as well as the A_2 and B_2 components may be summed and compared to the true A' and A'' components, respectively.

Figure (8.3) shows that the results obtained using the molecular-conductance point group are indistinguishable from the exact transmission at most energies. The important practical result is that the symmetry reduction in systems bound through a terminal sulfur can be considered, to a very good approximation, to only be the loss of end-to-end symmetry *irrespective* of the symmetry of the electrode-molecule junction.

Also shown in Fig. (8.3) are the results obtained using the C_s point group with the inclusion of 25 gold atoms per contact in the extended molecule. It is again evident that the inclusion of gold atoms in the extended molecule perturbs the symmetry separated

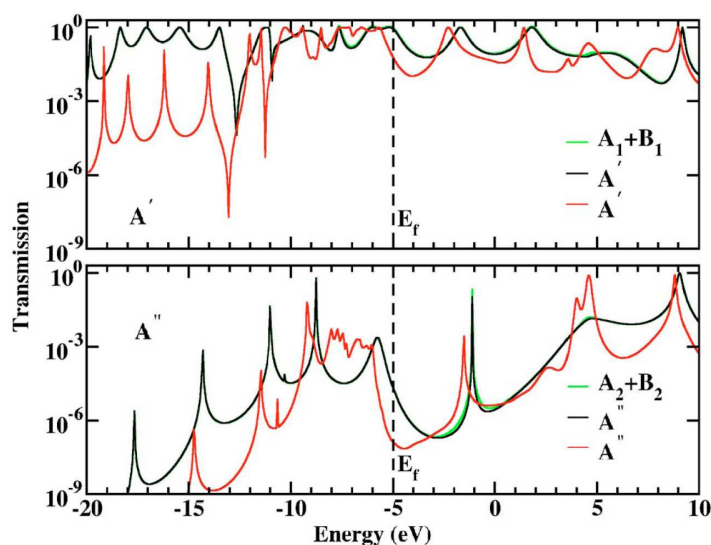


Figure 8.3: Symmetry separated components of the transmission through chemisorbed 1,4-benzenedithiol bound to the hollow site with two gold contacts. In each case the green curve is the sum of the symmetry components when the conductance point group is approximated to be C_{2v} , while the black curve is the transmission when the system is treated without approximation as having a conductance point group of C_s . Also shown in red is the transmission when 25 gold atoms are included on each side to form an extended molecule.

components of the transmission without changing their character. The difference in this instance is that with an extended molecule it is not possible to examine the hollow binding site transmission in C_{2v} symmetry. Consequently, the level of detail that can be obtained in symmetry analysis is reduced. The effect of any modification of the molecule which does not affect all symmetry components equally, for example, chemical substitution, will be most clearly seen in a higher symmetry representation.

The separation of transmission into symmetry components as shown in Figs. (8.2) and (8.3) indicates that at no energy is the transmission *purely* through channels of just one symmetry. There are energies at which the transmission is dominated by a single symmetry component but other symmetry components are always present, albeit that their contributions are orders of magnitude less. This fact may be vital to interpretation of spectroscopic properties associated with electron transmission, because channels that make small contributions to the total current can, in principle, dominate effects such as IETS. Further, a relationship between the peaks in each symmetry component of the transmission and molecular orbitals of known symmetry can be identified leading to a useful chemical picture of molecular conductance that can aid synthetic design.

An alternative perspective on the significance of the conductance point group can be gained by considering the nature of the wave vectors transmitted through the entire molecular component, whether this constitutes the real molecule or some extended one. In the bulk electrode on either side, the wave vectors of the transmitted and reflected electrons can be defined. From this point of view the molecule can be considered as a momentum filter only

allowing certain wave vectors to be transmitted [112]. It is the conductance point group that determines those linear combinations of wave vectors that will be allowed to pass through the molecule from the set of all wave vectors incident on the electrode-molecule interface.

While all of the discussion so far has been concerned with systems where the scattering processes are neglected, $\Sigma_{ph}^{<, >} = 0$, or when $\Sigma_{ph}^{<, >}$ commutes with all symmetry operators that define the geometric point group of the molecular system, the applicability of symmetry characterization is not limited to such situations. These conditions on $\Sigma_{ph}^{<, >}$ result in it not modifying the conductance point group of the system from what would be expected through analysis of $\Sigma_{L(R)}^r$ alone. In the case where $\Sigma_{ph}^{<, >}$ is not equal to zero and does not have the symmetry of the geometric point group of the system, it may act to further reduce the conductance point group. If $\Sigma_{ph}^{<, >}$ has the same symmetry as $\Sigma_{L(R)}^r$, this will not be the case as no further symmetry breaking will be introduced. However, if $\Sigma_{ph}^{<, >}$ has lower symmetry than $\Sigma_{L(R)}^r$, it will become the dominant component in the symmetry reduction of the conduction process and the conductance point group will be determined also by the symmetry of $\Sigma_{ph}^{<, >}$. A symmetry breaking component arising from $\Sigma_{ph}^{<, >}$ may be large, depending upon the effect being included, in which case analysis using molecular-conductance point group may be a poor approximation to the transmission obtained using the conductance point group.

8.2 The definition of channels in elastic transport

The idea of conduction channels is connected to the real promise of molecular electronics which is not just in the small size of molecular components but also in tunable electrical characteristics. If molecular properties can control conduction characteristics, then these could be as varied as the immense range of chemical substitution allows. In the devices developed today it is not always clear that it is the molecular characteristics, as opposed to properties of the junction, that dominate the transmission [110, 22]. However, increasingly sophisticated experimental techniques are allowing more information to be obtained about the conducting entity than just simple current-voltage characteristics. Recently, shot-noise measurements on a single molecule were reported [113], which made it possible to distinguish between proposed binding geometries because of the differing numbers of conduction channels that were active in each case. The conduction channels observed in shot-noise measurements must have a molecular origin; however, it has not been clear how to describe them in terms of the properties of the molecule.

Qualitatively, it is clear that resonant transport occurs at energies close to that of the molecular orbitals of the molecular component of the system [114]. However, molecular conduction has, so far, eluded quantitative description in chemical terms. It was shown by Büttiker that it is possible to separate transmission into components from individual channels [115] whose transmission coefficient lies between zero and one. This has been applied to molecular systems [116] and necked metallic wires [112], but it is not clear how they may be quantitatively described in terms of molecular properties, for example the molecular orbitals, of the system. In the case of single-atom metallic wires, it has been

shown both experimentally [17] and theoretically [117] that the number of channels relates to the valence of the atom; however, this needs to be extended to describe how conduction channels operate in molecular systems.

Here it will be shown how conduction channels can be linked to molecular properties. First, it is shown that only a small number of conduction channels are expected because of the nature of chemical binding of molecules to electrodes. Second, it is shown alternatively how conduction channels can be understood in terms of the connections that they provide between incoming and outgoing junction states.

8.2.1 Büttiker channels

Using the ubiquitous Landauer-Büttiker equation, the current (I) through a molecule can be expressed as a function of bias (V) as

$$I(V) = \frac{2e}{h} \int_{-\infty}^{+\infty} g(E, V)(n_L - n_R)dE \quad (8.1)$$

The quantum conductance, $g(E, V)$ (the sum of the transmission probabilities through all available channels) is defined as usual:

$$g(E, V) = Tr[\Gamma_L(E, V)\mathbf{G}^r(E, V)\Gamma_R(E, V)\mathbf{G}^a(E, V)]. \quad (8.2)$$

The one-electron Hamiltonians, \mathbf{H}_D , \mathbf{H}_L , and \mathbf{H}_R , as well as the electrode-molecule coupling matrices, \mathbf{J}_{DL} and \mathbf{J}_{DR} , are partitioned from the Hamiltonian of the full electrode-molecule-electrode system \mathbf{H}'_0 , Eqn. (5.2). As shown by Büttiker, the contributions from individual eigenchannels can be determined by diagonalizing $\mathbf{T} = \Gamma_L\mathbf{G}^r\Gamma_R\mathbf{G}^a$ from Eqn. (8.2) to yield [115]:

$$g(E, V) = \sum_i T_i(E, V) \quad (8.3)$$

where T_i are the resulting eigenvalues and $0 \leq T_i \leq 1$. In order to label the eigenvalues T_i with an irreducible representation of the molecular-conductance point group of the system, before diagonalizing $\mathbf{T}(E, V)$ we perform a transformation of the matrix in the symmetry adapted basis. The matrix results block-diagonalized and every block refers to a single irreducible representation of the point group:

$$\mathbf{T} = \begin{pmatrix} \mathbf{IR}_1 & 0 & 0 \\ 0 & \mathbf{IR}_2 & 0 \\ 0 & 0 & \ddots \end{pmatrix} \quad (8.4)$$

where \mathbf{IR}_i stands for the i^{th} irreducible representation of the symmetry group.

Performing this analysis for a 1,4-benzenedithiol illuminates a number of interesting features. The molecule is chemisorbed at the bridge site of two gold electrodes as shown in Fig. (8.1), with partitioning of \mathbf{H}'_0 into its \mathbf{H}_D , \mathbf{H}_L , and \mathbf{H}_R components occurring across

the gold-sulfur bonds. The first feature of this system is that there are very few eigenchannels with relevant (above 10^{-14}) transmission. Figure (8.4) shows the eigenchannel transmissions for this system separated into the symmetry components of the molecular-conductance point group.

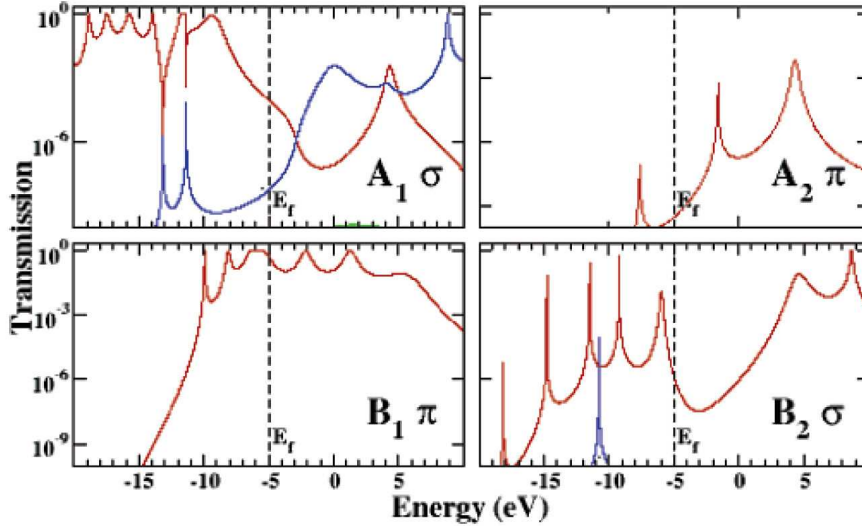


Figure 8.4: Contributions to the transmission from individual conduction channels separated by symmetry group for clarity. In each symmetry group, the primary conduction channel (dominant transmission at the Fermi energy) is shown in red, the secondary channel is shown in blue, and only in the A_1 case is a third channel visible in green.

The number of eigenchannels is formally related to the dimension of the molecule (for the minimal basis set used in the system here we have 46 channels); however, the vast majority of these channels do not contribute to the total transmission. The small number of nonzero eigenchannel transmissions can be understood by considering the nature of the chemical binding to the electrodes and the impact this has on the matrices that generate the transmission. The main feature of the $\mathbf{T}_{L(R)}(E, V)$ matrices is that they contain the information about the bottleneck of the junction between the sulfur atoms and the contacts. So, if the electrode only couples with a small number of molecular states then there will be many near zero elements in \mathbf{J}_{DL} and \mathbf{J}_{DR} . As a result, rows and columns of near-zero elements appear in $\mathbf{T}_{L(R)}(E, V)$, which in turn leads to eigenchannels with negligible transmission. This is an intuitive picture of transmission; the number of open eigenchannels will not be greater than those supported by the smallest bottleneck in the system. It has long been recognized to apply to necked junctions in atomic wires [117] but here it is shown to be generally relevant to bridged-conductor conductivity.

Mathematically, this process is readily identified when the bottleneck occurs at the sites at which \mathbf{H}_D , \mathbf{H}_L , and \mathbf{H}_R are partitioned, as described above. If the situation is examined numerically, including 25 gold atoms on each side in the extended molecule. This results in a modified transmission curve as the influence of the electrodes is treated more precisely through the inclusion of explicit gold atoms in the molecular part compared

to when the effect of the electrodes is limited to the self energies, $\Sigma_L^r(E, V)$ and $\Sigma_R^r(E, V)$. However, the number of eigenchannels found with transmission above 10^{-10} is *invariant* to this enhancement. The internal coupling elements between the gold and sulfur atoms within \mathbf{H}_D are the dominant factor controlling the number of open channels by effectively reducing the rank of the product of $g(E, V)$. This is an important result: it is the physical and chemical nature of the system, not the choice of partitioning in the calculation, that determines the number of conduction channels with significant transmission. The number of channels with significant transmission is determined by the size of the bottleneck that the connection through the sulfur allows and is not determined by the size of the matrix \mathbf{H}_D , which determines the theoretical limit for the number of perceived eigenchannels. However, through judicious choice of the partitioning, the nature of the conductivity may be described using simple models [118, 119] or molecular symmetry.

The number of eigenchannels with nonzero transmission, as well as the total transmission, is dependent on the size of the basis set used for the atoms at the bottleneck. In the above calculations, the basis set used for the sulfur atom has *s*, *p*, and *d* functions. If the *d* functions are removed, then the A_2 channel shown in Fig. (8.4) disappears completely in addition to the changes in shape that come from the total transmission being modified. A result similar to this was obtained in the work of Cuevas *et al.* [117] for tunneling through atomic wires. Significantly, in that application the electronic coupling elements were assumed to connect only nearest-neighbor atoms, resulting in the size of the bottleneck being *exactly* the dimension of the number of basis functions on a single metal atom. For molecules in comprehensive treatments, it is not always reasonable to assume that only nearest-neighbor coupling elements are nonzero. At the molecule-electrode junction, for example, the accuracy of such an assumption will be dependent on the nature of the binding group. In the case of chemisorbed 1,4-benzenedithiol, direct Au-S and S-C couplings are the dominant terms but an extensive calculation will also give small but nonzero Au-H and Au-C couplings. This means that the number of open conduction channels will not be precisely determined by the Au-S interaction.

Beyond the technicalities of the calculations, the significance of this result is that the number of open conduction channels arises from a chemical property of the system. The smallest bottleneck in the system can be controlled by chemical substitution, be it by multiple binding groups between the molecule and the electrode or by different backbone structures for molecular wires. This understanding allows for appropriate synthetic targets to be envisaged without any unforeseen constraints in conductivity dominating the conductance characteristics. Additionally, when the bottleneck occurs at the binding site, as was the case for the example system above, the size of this bottleneck, that is, the number of observable conduction channels, will change with changes in the binding geometry. For example, if the molecule was tilted on the surface direct Au-H and Au-C coupling would be more significant and may increase the number of conduction channels observed. Conversely, if the terminal sulfur atom sat directly above a super-surface gold atom or at the apex of a single atom on a gold tip, then this effect may reduce the coupling with the sulfur orbitals of π symmetry and thereby reduce the number of channels observed. This means that molecules such as chemisorbed 1,4-benzenedithiol can be used as probes for the nature of thiol binding on gold surfaces as the number of channels observed in shot-noise measurements will

be sensitive to the geometry of the junction region.

Understanding the cause of the small number of open eigenchannels does not, however, provide any further illumination of the relationship between conduction channels and molecular orbitals. Indeed, a striking feature of Fig. (8.4) is that each conduction channel spans a range that encompasses many molecular orbitals further complicating any quantitative description of conduction through a single orbital. As has been reported elsewhere [118], when the eigenvectors are computed in the atomic orbital basis they are difficult to interpret. In fact, the details of the unusual character of the eigenvectors of $g(E,V)$ are important. The eigenvectors at all transmission energies E are dominated by coefficients on the sulfur atom at the charge-injecting electrode. The charge injecting electrode (L in the notation used herein) is distinguished by the asymmetry in $g(E,V)$, which allows the total transmission to be calculated through the knowledge of the transmission across the interface between the charge injecting electrode and the molecule. Where two channels cross (akin to avoided crossings between molecular potential energy surfaces) the identity of each channel can, in principle, be determined from the eigenvectors. However, there are energies at which two channels meet but do not cross, a situation that cannot occur for Hermitian operators, and the eigenvectors are *not* continuous over this region with the meeting point coinciding with the discontinuity. Also, the eigenvectors are not guaranteed to be orthogonal (zero overlap) and this point actually coincides with the *maximum* in the overlap between the two eigenvectors. An example of where this unusual behavior occurs is the meeting of two channels around -13 eV in the A_1 symmetry transmission. This region is shown in high resolution in Fig. (8.5) with the coefficients on the sulfur atom at the charge-injecting electrode as a function of energy shown below for the primary and secondary conduction channels shown above, the discontinuity being readily apparent around -13.15 eV, whereas the overlap peaks at 0.8, indicating nearly parallel eigenvectors. In fact, the determinant of the eigenvector matrix, which is 1 for an orthogonal transformation, takes a maximum value as a function of energy of just 10^{-32} , indicating a high degree of eigenvector linear dependency.

8.2.2 Γ -channels

As mentioned previously, the eigenvectors of the Büttiker channels reflect only the site of charge injection and do not capture the full symmetry of through-molecule conductivity. A means by which this symmetry can be perceived is through pre-diagonalization of the two sets of molecule-electrode interactions $\mathbf{\Gamma}_{L(R)}(E,V)$ as suggested by Troisi and Ratner [38]. I ignore the orbital overlap during this process, introducing the (real diagonal) eigenvalue and (real orthogonal) eigenvector matrices $\mathbf{\Gamma}_{L(R)}(E,V)$ and $\mathbf{D}_{L(R)}(E,V)$, respectively, through

$$\hat{\mathbf{\Gamma}}_{L(R)}(E,V) = \mathbf{D}_{L(R)}^\dagger(E,V) \mathbf{\Gamma}_{L(R)}(E,V) \mathbf{D}_{L(R)}(E,V) \quad (8.5)$$

In order to assign symmetry to the eigenvalues a transformation of the two matrices in the symmetry adapted basis must be performed before the diagonalization. If the two junctions are symmetrically related, then $\hat{\mathbf{\Gamma}}_L(E,V) = \hat{\mathbf{\Gamma}}_R(E,V) = \hat{\mathbf{\Gamma}}(E,V)$ so the current

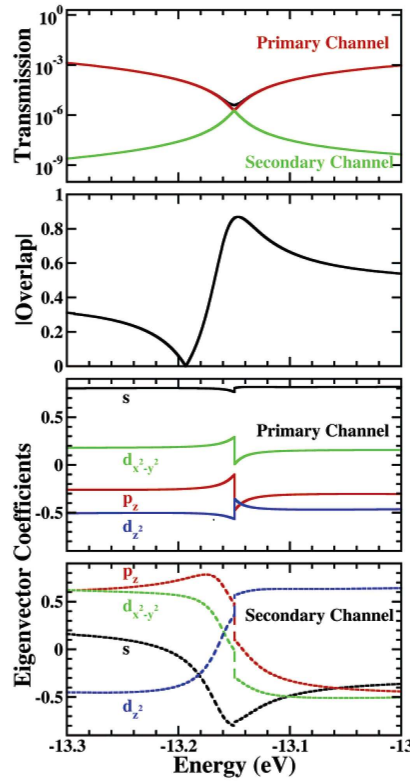


Figure 8.5: Unusual properties of the eigenvectors associated with the primary and secondary channel of A_1 symmetry at the point where they meet but do not cross. The maximum in the overlap and the discontinuities in the coefficients on the sulfur at the charge injecting electrode atom illustrate the unusual characteristics of the eigenvectors associated with conduction channels.

from Eqn. (8.2) can be written without approximation as

$$\begin{aligned}
 g(E, V) &= \text{Tr}[\hat{\mathbf{F}}(E, V)\hat{\mathbf{G}}^r(E, V)\hat{\mathbf{F}}(E, V)\hat{\mathbf{G}}^a(E, V)] \\
 &= \sum_{ij} \hat{\mathbf{F}}_{ii}^\lambda(E, V)\hat{\mathbf{F}}_{jj}^\lambda(E, V)|\hat{\mathbf{G}}_{ij}^r(E, V)|^2
 \end{aligned} \tag{8.6}$$

where

$$\hat{\mathbf{G}}^r(E, V) = \mathbf{D}_L^{-1}(E, V)\mathbf{G}^r(E, V)\mathbf{D}_R(E, V) \tag{8.7}$$

and λ is the label for the irreducible representation to which belongs a certain eigenvalue. This expression for the transmission suggests that the tunneling current can be viewed as entering one electrode through the input junction channel i , being transferred through the molecule with probability $|\hat{\mathbf{G}}_{ij}^r(E, V)|^2$ and then leaving through the exit junction j . In this

way, the total current can be considered to be decomposed into the sum of n^2 independent channels, where n is the number of atomic orbitals of the molecule. This interpretation is formally applicable whenever the eigenvalues $\hat{\Gamma}_{ii}^\lambda(E, V)$ are guaranteed to be all positive, as is the case when the basis functions do not overlap. In general, the arguments used earlier to interpret the Büttiker conduction channels may again be applied, however, concluding that most of the eigenvalues should be zero with just a few large and positive contributions facilitating current flow. Hence this interpretation, though only formally exact for a restricted problem, is expected to be rather useful in characterizing through-molecule conductivity.

For the case of 1,4-benzenedithiol symmetrically chemisorbed between two gold contacts as studied earlier using full treatment of orbital overlap, numerical calculations reveal only 15 junction eigenvalues $\hat{\Gamma}_{ii}^\lambda$ that are nonzero (i.e., $\hat{\Gamma}_{ii}^\lambda > 10^{-16}$ within numerical precision); these are listed in Table (8.1). Of them, only one is negative corresponding to a junction path of A_1 symmetry with $\hat{\Gamma}_{ii}^\lambda = -1.1 \times 10^{-12}$. Hence, the interference contributions to Eqn. (8.6) are at least 12 orders of magnitude weaker than the direct contributions and so the current may indeed be perceived in terms of simple contributions from each junction linked through the molecule.

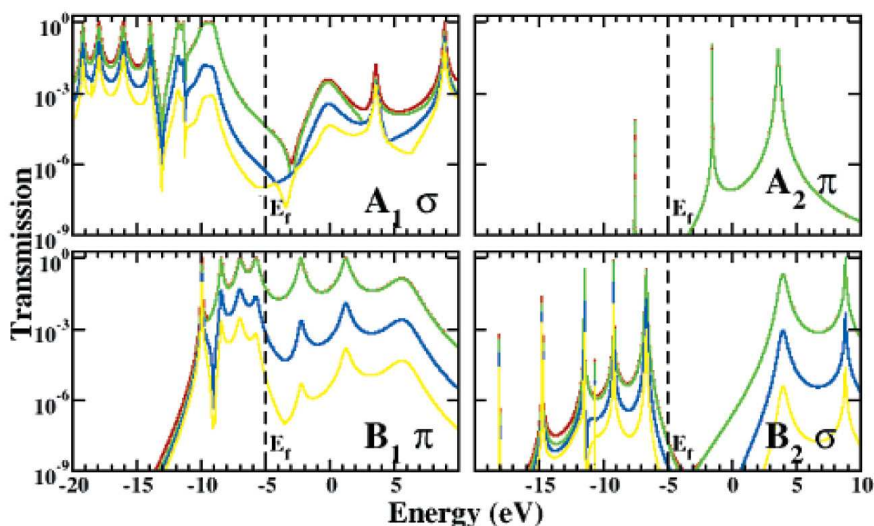


Figure 8.6: First three conduction channels obtained through the Troisi-Ratner method for each system. In each case the primary channel is shown in green, the secondary channel is shown in blue, and the tertiary channel is shown in yellow. Where visible, the red curve represents the total transmission for each symmetry.

From Table (8.1), it can be seen that a significant number of the junction eigenvalues fall within 3 orders of magnitude of the most prolific junction channel. On the basis of the very small number of Büttiker channels depicted in Fig. (8.4) smaller number of significant junction channels could be expected. The change is due to the neglect of the orbital overlap in Eqn. (8.7), a feature required in order to obtain the desired $|\hat{G}^r(E, V)|^2$

label	A ₁	A ₂	B ₁	B ₂
1	1.9462×10^{-1}	1.2691×10^{-3}	3.4940×10^{-2}	8.1665×10^{-3}
2	1.0196×10^{-2}		4.4071×10^{-3}	3.5221×10^{-4}
3	1.5149×10^{-3}		8.7315×10^{-8}	4.7558×10^{-10}
4	7.6416×10^{-5}			9.4243×10^{-14}
5	4.9025×10^{-8}			
6	3.6017×10^{-9}			
7	-1.1494×10^{-12}			

Table 8.1: Nonzero Eigenvalues of $\hat{\Gamma}_{ii}^\lambda$ at -5.0 eV Separated into Symmetry-Block contributions.

dependence of the molecular contribution in Eqn. (8.6). The contributions of the dominant terms from the individual $\hat{\Gamma}_{ii}^\lambda(E, V)\hat{\Gamma}_{jj}^\lambda(E, V)|\hat{G}_{ij}^r(E, V)|^2$ terms in Eqn. (8.6) are shown in Fig. (8.6). For each symmetry the contribution from the $\hat{\Gamma}_{11}^\lambda(E, V)\hat{\Gamma}_{11}^\lambda(E, V)|\hat{G}_{11}^r(E, V)|^2$ term is in general the most important one. The energy dependence of these probabilities reflects largely the nature of the conducting molecule and is independent of the path that the tunneling electrons takes through the entry and exit channels. The Büttiker channels focus on the conductivity bottlenecks and associated shot noise, whereas the Troisi-Ratner channels focus on the nature of both junctions and the net way in which the molecule passes the current, but neither of these illuminates the means by which the molecule facilitates conductivity.

8.3 Conclusions

The symmetry of molecular conductance is not simply that of the geometric point group of the conducting molecule but instead can be described in terms of a molecular-conductance point group and/or a full conductance point group. While the molecular-conductance point group can always readily be determined from the geometric point group as is illustrated for some molecules commonly used for molecular electronics applications in Fig. (8.7), the conductance point group requires detailed knowledge of the possible symmetry breaking contributions from the electrodes as well as any other effect included through additional self-energies.

In the case of molecules bound to gold through a terminal sulfur, in the absence of symmetry breaking terms in $\Sigma_{ph}^{<, >}$, if the molecular-conductance point group is different from the full conductance point group then the simpler description is shown to still provide a good approximation to the transmission. It is thus possible to determine the symmetry of conduction channels (and thereby understand the contribution that molecular symmetry makes to conductance) and also understand how the selection rules of spectroscopies applied to molecules in this conducting state operate. Of course it is not always clear that molecular properties will dominate single-molecule conduction; indeed, there is considerable evidence that the contacts may in some cases dominate the conduction characteristics.

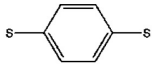
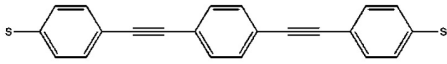
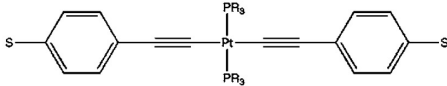

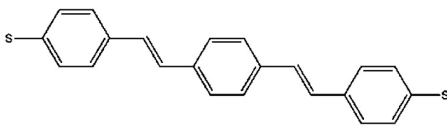
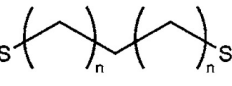
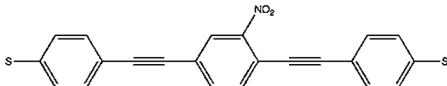
$\text{Au} - \text{Au} - \text{Au} - \text{Au}$	$D_{\infty h} \rightarrow C_{\infty v}$
	$D_{2h} \rightarrow C_{2v}$
	$D_{2h} \rightarrow C_{2v}$
	$\sim D_{2h}^*$ $\rightarrow \sim C_{2v}$
 even alkane	$C_{2h} \rightarrow C_s$
	$C_{2h} \rightarrow C_s$
 odd alkane	$C_{2v} \rightarrow C_s$
	$C_s \rightarrow C_s$

Figure 8.7: The symmetry reduction between the geometric point group and the molecular-conductance point group for some common molecules used in molecular electronics research. (*) Precisely, the geometric point group is either C_{2v} or C_{2h} depending upon the PR_3 rotation: The C_{2h} case results in a molecular-conductance point group of C_s , whereas the C_{2v} case retains this symmetry for the molecular-conductance point group.

Moreover, by separating molecular transmission in a variety of ways into non-interacting components it is possible to isolate the roles of the junction region and the bridging molecule in determining conductivity properties. First, the small number of rigorously defined eigenchannels with nonzero transmission can be understood to arise from the size of the smallest bottleneck in the system. This, in turn arises, from the chemical structure of the molecule or the interaction of the binding group with the electrodes and consequently can be controlled by synthetic modifications.

Further, it means that, with careful selection of target molecules, shot-noise measurements can be used to probe the details of molecular binding geometry. Second, by pre-diagonalizing \mathbf{T} , conduction can be described in terms of molecular conductivity channels linking well defined junction states. Although this process is only approximate, the interference terms found manifest in our model calculations of conductivity through 1,4-benzenedithiol were 12 orders of magnitude smaller than the primary contributions, making this an excellent practical method for understanding the role of the junction in the process.

Together these features make it possible to quantitatively describe molecular conduction in terms of atomistic descriptors of the conducting system.

Propensity Rules in Inelastic Electron Tunneling Spectroscopy

This Chapter is devoted to the application of the theoretical machinery developed in Chapter 8, molecular-conductance point group and channels, to investigate IETS. Already two groups Troisi *et al.* [38, 120] and Lorente *et al.* [39, 40], have developed some intuitive propensity rules that capture many of the features that lead to vibrational-mode selectivity in IETS. The main aim of the present Chapter is to present a general approach to the interpretation of IETS measurements, starting with fundamental principles implemented using a generally applicable a priori computational scheme. Further it will be derived and justified a simplified form of the inelastic current. Finally, it will be shown how not only the propensity rules Troisi and Ratner may be rigorously derived but also how these rules can be extended. This can provide a thorough, yet easily, understood description of the general phenomenon of IETS that may be readily applied in diverse practical applications.

9.1 Theoretical formalism

Starting from the ubiquitous Meir-Wingreen equation for the current:

$$I = \frac{2e}{h} \int_{-\infty}^{+\infty} Tr[\Sigma_L^<(E)\mathbf{G}^>(E) - \Sigma_L^>(E)\mathbf{G}^<(E)]dE \quad (9.1)$$

and remembering that at Born Approximation (BA) level the electron-phonon self-energies are

$$\Sigma_{ph}^<,>(E) = \sum_{\alpha} \frac{i}{2\pi} \int_{-\infty}^{\infty} \mathbf{M}^{\alpha} \mathbf{G}_0^<,>(E - E') \mathbf{M}^{\alpha} D_{\alpha,0}^<,>(E') dE' \quad (9.2)$$

with \mathbf{M}^α

$$\mathbf{M}^\alpha = \frac{\partial \mathbf{H}_D}{\partial Q_\alpha} - \frac{\partial \mathbf{S}}{\partial Q_\alpha} \mathbf{S}^{-1} \mathbf{H}_D - \mathbf{H}_D \mathbf{S}^{-1} \frac{\partial \mathbf{S}}{\partial Q_\alpha} \quad (9.3)$$

for vibrational mode α with normal mode Q_α . As IETS measurements are performed at very low temperature (usually 4 K), we can simplify Eqn. (9.2) assuming temperature $T = 0$. We also approximate the phonon population as a collection of Einstein oscillators in thermodynamic equilibrium with the environment. Under this approximation, at $T = 0$, the population of phonon N_α is set to zero and Eqn. (9.2) becomes

$$\Sigma_{ph}^{<, >}(E) = \mathbf{M}^\alpha \mathbf{G}_0^{<, >}(E \pm \omega_\alpha) \mathbf{M}^\alpha \quad (9.4)$$

where the upper (lower) sign is for the lesser (greater) self-energy and $\mathbf{G}_0^{<, >}$ are the zeroth order lesser or greater Green's functions obtained in the absence of electron-phonon coupling. The current from Eqn. (9.1) thus becomes, expanding up to the second order in \mathbf{M}^α :

$$\begin{aligned} I &= \frac{2e}{h} \int_{\mu_R}^{\mu_L} \left(Tr[\Gamma_L \mathbf{G}_0^r \Gamma_R \mathbf{G}_0^a] + \sum_{\alpha} Tr[\Gamma_L \mathbf{G}_0^r \Sigma_{ph}^r \mathbf{G}_0^r \Gamma_R \mathbf{G}_0^a] + Tr[\Gamma_L \mathbf{G}_0^r \Gamma_R \mathbf{G}_0^a \Sigma_{ph}^a \mathbf{G}_0^a] dE \right) \\ &+ \sum_{\alpha} \Theta(\mu_L - \mu_R - \omega_\alpha) \frac{2e}{h} \int_{\mu_R + \omega_\alpha}^{\mu_L} Tr[\Gamma_L \mathbf{G}_0^r \mathbf{M}^\alpha \tilde{\mathbf{G}}_0^r \tilde{\Gamma}_R \tilde{\mathbf{G}}_0^a \mathbf{M}^\alpha \mathbf{G}_0^a] dE \\ &= I_{el} + \sum_{\alpha} \Theta(\mu_L - \mu_R - \omega_\alpha) I_{inel}^\alpha \end{aligned} \quad (9.5)$$

where the three terms in parenthesis are part of the coherent current including part of the virtual electron-phonon scattering terms, whilst the latter term is the real inelastic current. The inelastic current shows in fact a change in the limits of integrations due to the real emission of a phonon.

I_{inel}^α is defined as

$$I_{inel}^\alpha = \frac{2e}{h} \int_{\mu_R + \omega_\alpha}^{\mu_L} g_\alpha dE \quad (9.6)$$

with

$$g_\alpha = Tr[\Gamma_L \mathbf{G}_0^r \mathbf{M}^\alpha \tilde{\mathbf{G}}_0^r \tilde{\Gamma}_R \tilde{\mathbf{G}}_0^a \mathbf{M}^\alpha \mathbf{G}_0^a]. \quad (9.7)$$

The use of the zeroth order Green's functions in Eqs. (9.5) and (9.6) is a valid approximation, because the electron-phonon interaction is small in the system considered here. Numerical calculations, including the renormalization of the propagators lead to essentially the same incoherent current, to within few percent of errors.

The first three terms in Eqn. (9.5) give a coherent contribution, describing the elastic part of the current, while the last term is the inelastic component expressed as the sum of

independent contributions, I_{inel}^α , from all of the vibrational modes of the molecule. In order for phonon emission to take place, the applied bias must obey the condition $\mu_L - \mu_R > \omega_\alpha$, which is emphasized by the Heaviside function in front of the inelastic component.

In the inelastic term the matrices with a tilde are computed at an energy shifted by the energy of a phonon: $E' = E - \omega_\alpha$. The shift comes from the conservation of energy and in fact describes the lowering of the energy of the electron after the excitation of a phonon. We hence see that the inelastic current depends on five basic quantities: the propagators $\mathbf{G}_0^{r,a}$, the vibronic coupling matrix \mathbf{M}^α , the vibrational frequency ω_α , the couplings between the contacts and the molecule $\Gamma_{L(R)}$, and the Fermi energy E_F . The main question is, of course: what are the relationships between these quantities and how we can simplify the picture in order to have a better insight into the physics involved?

The application of the formalism developed in Chapter 8 must certainly be applied. The definition of the molecular conductance point group permits to assign univocally the symmetry to the molecule connected to the contacts and so the entire device part. This define to which symmetry group belongs the device under investigation. After the assignment of the molecular conductance point group is always possible to rotate all the matrices involved in the inelastic transmission, which is the one relevant for the IETS, in the symmetry adapted basis for the symmetry point group. This means that all the matrices are block diagonalized and every block represents one irreducible representation of the molecular conductance point group. Diagonalizing the matrix we get that all the eigenvalues spectrum can finally be assigned to a certain irreducible representation as the corresponding eigenvector. Particular important is the transformation into the symmetry adapted basis of the electron-phonon coupling matrices \mathbf{M}^α that, depending on the symmetry of the vibrational mode they describe, can result in a block diagonal matrix in case of a totally symmetric mode or in a matrix with off diagonal blocks which describe the mixing between channels which belong to different irreducible representations induced by the vibrational mode. Since now it is assumed that all the matrices are already rotated in the symmetry adapted basis corresponding to the molecular conductance point group so that it is always possible to assign an irreducible representation label to all the modes and the channels involved in the analysis of the inelastic current at the base of the IETS signal.

9.2 From Γ -channels to A-channels

The specific system investigated in this study is the 1,4-benzenedithiol molecule chemisorbed between two gold contacts already used in the previous Chapter, though the applications of the method presented are quite general. As already demonstrated, the symmetry properties of coherent transport through gold-thiol junctions are dominated by the molecular symmetry and that low-dimensional models of the electrode capture most of the essential features of observed IETS. So only two atoms are used to represent each lead, as shown in Fig. (9.1).

The low-temperature IETS spectrum calculated using only the Born approximation is shown and assigned in Fig. (9.2). We seek a basic understanding of how this spectrum arises and the relative propensities calculated for the modes. The chemisorbed 1,4-

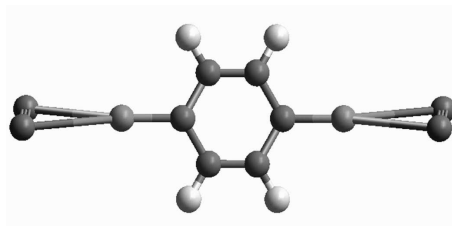


Figure 9.1: A chemisorbed 1,4-benzenedithiol molecule connected to two gold atoms on each side.

benzenedithiol molecule has d_{2h} symmetry, and the IETS-active modes are categorized in Fig. (9.2) accordingly: the most prominent modes are in-plane totally symmetric a_g modes while the out-of-plane antisymmetric b_{2g} and b_{3u} modes are also significant. However, the conduction process depicted by Eqn. (9.6) does not display d_{2h} symmetry as the $\Gamma_{L(R)}$ matrices have only the symmetry of the Left and Right junctions, not the full molecular or device symmetry, see Chapter 8. Analysis of Eqn. (9.6) thus must commence with this reduced symmetry, the molecular conductance point group symmetry which, in this case, is C_{2v} ; note that lower-case symbols are used throughout for the description of molecular symmetry while upper-case symbols are used for the description of molecular-conductance symmetry. We must demonstrate how IETS appears to take on the molecular symmetry properties in spite of this limitation.

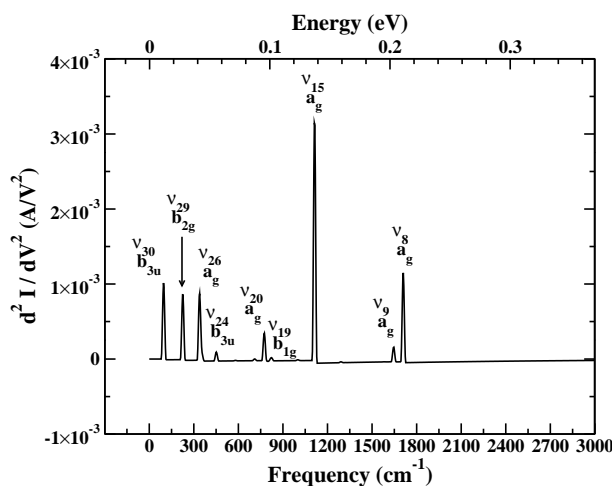


Figure 9.2: The IET spectrum of our system. The broadening of the peaks has been introduced empirically considering a phonon lifetime of 6.6×10^{-13} s, corresponding to a broadening of 2×10^{-3} eV.

The approach is based on the idea that both the elastic and inelastic current can be expressed as the sum of a small number of essentially non interacting paths or channels through the device. Using the same machinery used for elastic transport through the intro-

duction of the transformation

$$\hat{\Gamma}_{L(R)} = \mathbf{D}_{L(R)}^\dagger \Gamma_{L(R)} \mathbf{D}_{L(R)}, \quad (9.8)$$

which reduces the electrode-molecule coupling matrices to diagonal form, a transformation that captures the essence of the physical insight used previously by Troisi *et al.* [38, 120] in their proposed IETS propensity rules. After this transformation is applied we get the following formula for the inelastic current of every mode:

$$I_{inel}^\alpha = \frac{2e}{h} \int_{\mu_R + \omega_\alpha}^{\mu_L} \left(\sum_{ij} \hat{\Gamma}_{ii}^{L,\lambda} \hat{\Gamma}_{jj}^{R,\beta} (E - \omega_\alpha) |\hat{\Lambda}_{ij}|^2 \right) dE, \quad (9.9)$$

where $\hat{\Lambda} = \hat{\mathbf{G}}_0^r \hat{\mathbf{M}}^\alpha \hat{\mathbf{G}}_0^r (E - \omega_\alpha)$ and λ and β are the irreducible representation labels of the left and right channels respectively.

The above junction channels will provide a good simple description of the (elastic or inelastic) conduction process whenever the bottleneck between the molecule and its contacts is the most important physical element. In this depiction, $|\hat{\Lambda}_{ij}|^2$ determines the probability that an electron or hole that enters the molecule from Left lead through channel i , with symmetry λ , is scattered inelastically out the Right lead through channel j , with symmetry β . In Fig. (9.3), upper section, it is plotted the amplitude $\hat{\Gamma}_{ii}^{L,\lambda}$ for an electron entering the molecule in a window of energy of 5 eV encompassing the Fermi energy. The eigenvalues show a very low dependence on energy as the s -band density of states of the gold contacts is nearly energy independent. The graph shows also that effectively only one junction channel, of symmetry A_1 in the molecular-conductance point group, dominates the process, with the next most significant channel being of B_1 symmetry but an order of magnitude less transmissive. This result suggests that the most intense IETS process is likely to involve electrons or holes entering and exiting through the dominant A_1 Left and Right junction channels, respectively; a process that is only possible when vibrations of A_1 symmetry are involved. While this argument correctly predicts the propensity for a_g modes apparent in Fig. (9.2), the dominant process is actually found to involve the *less* transmissive B_1 channels of the Left and Right junctions. This shows that the $\hat{\Lambda}$ matrix, which contains information about the chemical properties of the molecule, also plays an important role in selecting which channel is the most important for the current, a role that arises as the conduction in the molecule near the Fermi energy of chemisorbed 1,4-benzenedithiol is dominated by the electronic π -system that embodies B_1 but not A_1 symmetry.

The promise of this approach points to the possibility that a new set of channels might preserve all the nice characteristics of the previous ones, but allow for better insight into the role of the molecular properties. My proposal lies in a second transformation based on diagonalization of the matrices $\mathbf{A}^R = \mathbf{G}_0^r \Gamma_R \mathbf{G}_0^a$ and $(\mathbf{A}^L)^* = \mathbf{G}_0^a \Gamma_L \mathbf{G}_0^r$

$$\begin{aligned} \bar{\mathbf{A}}^R &= \mathbf{C}_R^\dagger \mathbf{A}^R \mathbf{C}_R, \\ \bar{\mathbf{A}}^L &= \mathbf{C}_L^\dagger (\mathbf{A}^L)^* \mathbf{C}_L. \end{aligned} \quad (9.10)$$

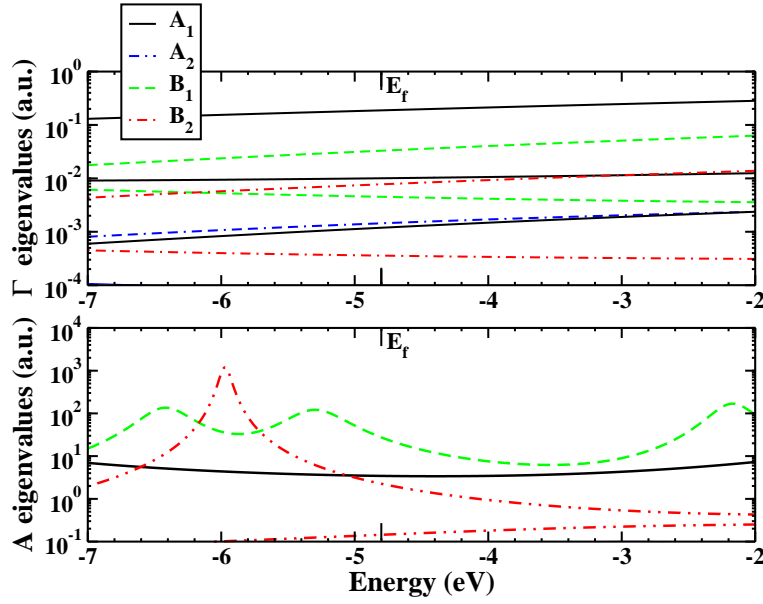


Figure 9.3: The energy dependence around the Fermi energy E_F for the eigenvalues $\hat{\Gamma}_{ii}^{L,\lambda}$ of Γ_L (top) and $\bar{A}_{ii}^{L,\lambda}$ of $\bar{\mathbf{A}}^L$ (bottom) partitioned into symmetry components.

The conjugation of \mathbf{A}^L arises because the Hamiltonian is a real matrix and therefore $(\mathbf{G}_0^r)^\dagger = (\mathbf{G}_0^r)^* = \mathbf{G}_0^a$. Moreover, due to the fact that \mathbf{A}^L is a Hermitian positive definite matrix, the conjugation does not change its positive and real eigenvalues.

Although in this derivation I have used the unrenormalized propagators, the approach is quite general since Eqn. (9.6) is valid also in the so called self-consistent Born approximation (SCBA), provided all $\mathbf{G}_0^{r,a}$ are substituted by renormalized propagators $\mathbf{G}^{r,a}$. The electron-phonon self-energy, $\Sigma_{ph}^{r,a}$, do not reduce further the symmetry of $(\mathbf{A}_L)^*$ and \mathbf{A}_R .

These matrices depict the coupling-weighted molecular density of states [53] and contain information about not only the junctions but also the chemical properties of the molecule as well. In Fig. (9.3), bottom section, there are plotted the eigenvalues $\bar{A}_{ii}^{L,\lambda}$ to be compared to those previously discussed for $\hat{\Gamma}_{ii}^{L,\lambda}$. The first thing we can observe is that a strong energy dependence appears with the $\bar{A}_{ii}^{L,\lambda}$ eigenvalues showing peaks close to the energies of the molecular orbitals. The dominant eigenvalues at the Fermi energy are listed in Table (9.1) and, as expected, by far the largest eigenvalue is found to be of B_1 symmetry, named $1B_1$. Hence this new transformation provides improved insight into the physical problem of IETS scattering. The inelastic conductances are then given by

$$g_\alpha = \sum_{ij} \bar{A}_{ii}^{L,\lambda} \bar{A}_{jj}^{R,\beta} (E - \omega_\alpha) \bar{M}_{ij}^\alpha \bar{M}_{ji}^\alpha, \quad (9.11)$$

where

$$\bar{\mathbf{M}}^\alpha = \mathbf{C}_L^\dagger \mathbf{M}^\alpha \mathbf{C}_R \text{ and } \bar{\bar{\mathbf{M}}}^\alpha = \mathbf{C}_R^\dagger \mathbf{M}^\alpha \mathbf{C}_L. \quad (9.12)$$

Differently from the Γ -transformation the \mathbf{A} matrices are positive definite and so their rotation should preserve this property. A subtlety, however, is that due to the differing energy dependencies of \mathbf{T}_L and \mathbf{T}_R apparent in Eqn. (9.5), the eigenvectors \mathbf{C}_L and \mathbf{C}_R are not simply related to each other so that \overline{M}_{ij}^α and \overline{M}_{ji}^α become unrelated complex quantities and hence the ij contributions in Eqn. (9.11) cannot strictly be interpreted as independent channels.

Nevertheless, in Table (9.2) the major contributions to g_α evaluated at the Fermi energy from the double sum of Eqn. 9.11 are listed and at most two contributions account for at least 95% of the IETS signal. Single significant contributions are found only for the case of totally symmetric vibrations (a_g symmetry in the full molecular point group), these involving an electron entering through the $1B_1$ channel of the Left lead, scattering off an a_g vibration and exiting through the $1B_1$ channel of the Right lead. Otherwise, closely related pairs of contributions are involved, with for example the intense b_{2g} mode ν_{29} activated by a 50% contribution from an electron that enters the $1A_1$ channel and exits the $1B_1$ channel combined with a 45% contribution from an electron that enters the $1B_1$ channel and exits the $1A_1$ channel.

label	$A_{ii}^{L,\lambda}(E_F)$
$1A_1$	3.44
$2A_1$	0.144
$3A_1$	0.0128
$1A_2$	0.0107
$1B_1$	27.4
$2B_1$	0.0705
$1B_2$	2.26

Table 9.1: All significantly large eigenvalues in atomic units of the electrode-coupling weighted density of states, $\overline{A}_{ii}^{L,\lambda}$ at the Fermi energy E_F from Fig. (9.3).

The analysis presented in Table (9.2) presumes that the total IETS signal I_{inel}^α from Eqn. (9.5) can be approximated from the inelastic scattering conductance g_α evaluated only at the Fermi energy E_F . To test this hypothesis, the relative values of the total inelastic currents calculated using Eqn. (9.5) and its approximation are given in the table where they are seen to be in very good agreement. The lack of symmetry in the leading terms shown in the table arise due to the shift ω_α that must be applied to the outgoing channel energies. Owing to the large values of the active frequencies compared to the energy dependencies depicted in Fig. (9.4), such differences appear profound and indeed result in factors of two differences between the displayed eigenvalues $\overline{\mathbf{A}}^L(E_F)$ and the analogous values of $\overline{\mathbf{A}}^R(E_F - \omega_\alpha)$. However, Troisi [38, 120] has argued that such changes should not qualitatively affect IETS propensity rules and hence in Table (9.2) an approximate analysis of g_α based on this further approximation is presented. Indeed, the relative propensities evaluated using this crude approximation differ by at most 20% from the exact intensities I_{inel}^α , indicating its usefulness. Further, this approximation leads to the re-expression of

Eqn. (9.11) in terms of true channels as

$$g_\alpha = \sum_{ij} \bar{A}_{ii}^{L,\lambda} \bar{A}_{jj}^{R,\beta} |\bar{M}_{ij}^\alpha|^2 \quad (9.13)$$

and the dominant terms in these sums, now symmetrically disposed towards both leads, are also shown in Table (9.2). Further, this approximation facilitates the rewriting of Eqn. (9.6) in the simple form

$$Tr[\Gamma_L \mathbf{G}_0^r \mathbf{M}^\alpha \mathbf{G}_0^r \Gamma_R \mathbf{G}_0^a \mathbf{M}^\alpha \mathbf{G}_0^a] = Tr[\Gamma_L \frac{\partial \mathbf{G}_0^r}{\partial Q} \Gamma_R \frac{\partial \mathbf{G}_0^a}{\partial Q}] \quad (9.14)$$

using $\mathbf{G}_0^{r,a} \mathbf{M}^\alpha \mathbf{G}_0^{r,a} = \frac{\partial \mathbf{G}_0^{r,a}}{\partial Q}$. This result is precisely that obtained by Troisi [38, 120] using a perturbation expansion of the elastic component of the current. Equation (9.14) puts this very useful expression in the context of a general theory for the non-equilibrium transport process and a hierarchy of numerical methods for obtaining the exact and approximate IETS intensities.

v	Vibration α		I_{inel}^α		$g_\alpha(E_F)$ exact			$g_\alpha(E_F)$ approximate			
	ω (eV [cm^{-1}])	$d_{2h}(C_{2v})$	Total	%	channel	%	Total	channel	%	channel	%
30	0.014 (112)	$b_{3u}(B_1)$	0.269	48	$1A_1 \rightarrow 1B_1$	46	0.288	$1A_1 \rightarrow 1B_1$	48	$1B_1 \rightarrow 1A_1$	48
29	0.028 (228)	$b_{2g}(B_1)$	0.189	50	$1A_1 \rightarrow 1B_1$	45	0.229	$1A_1 \rightarrow 1B_1$	48	$1B_1 \rightarrow 1A_1$	48
26	0.043 (346)	$a_g(A_1)$	0.199	97.9	$1B_1 \rightarrow 1B_1$		0.225	$1B_1 \rightarrow 1B_1$	98	$1B_1 \rightarrow 1B_1$	
25	0.045 (365)	$a_u(A_2)$	0.032	49	$1B_1 \rightarrow 1B_2$	51	0.035	$1B_1 \rightarrow 1B_2$	50	$1B_2 \rightarrow 1B_1$	50
24	0.057 (462)	$b_{3u}(B_1)$	0.023	57	$1A_1 \rightarrow 1B_1$	42	0.029	$1A_1 \rightarrow 1B_1$	50	$1B_1 \rightarrow 1A_1$	50
23	0.072 (583)	$b_{1u}(A_1)$	0.002	43	$1B_1 \rightarrow 2B_1$	57	0.002	$1B_1 \rightarrow 2B_1$	50	$2B_1 \rightarrow 1B_1$	50
21	0.088 (713)	$b_{2g}(B_1)$	0.014	54	$1A_1 \rightarrow 1B_1$	46	0.01	$1A_1 \rightarrow 1B_1$	50	$1B_1 \rightarrow 1A_1$	50
20	0.098 (790)	$a_g(A_1)$	0.127	97	$1B_1 \rightarrow 1B_1$		0.121	$1B_1 \rightarrow 1B_1$	96		
19	0.102 (826)	$b_{1g}(A_2)$	0.01	48	$1B_1 \rightarrow 1B_2$	52	0.009	$1B_1 \rightarrow 1B_2$	50	$1B_2 \rightarrow 1B_1$	50
18	0.104 (836)	$b_{3u}(B_1)$	0.008	55	$1A_1 \rightarrow 1B_1$	45	0.005	$1A_1 \rightarrow 1B_1$	50	$1B_1 \rightarrow 1A_1$	50
17	0.125 (1009)	$b_{2g}(B_1)$	0.004	62	$1A_1 \rightarrow 1B_1$	38	0.004	$1A_1 \rightarrow 1B_1$	50	$1B_1 \rightarrow 1A_1$	50
15	0.138 (1114)	$a_g(A_1)$	1.000	100	$1B_1 \rightarrow 1B_1$		1.000	$1B_1 \rightarrow 1B_1$	98.7		
13	0.161 (1303)	$b_{1u}(A_1)$	0.004	49	$1B_1 \rightarrow 2B_1$	51	0.003	$1B_1 \rightarrow 2B_1$	50	$2B_1 \rightarrow 1B_1$	50
9	0.205 (1656)	$a_g(A_1)$	0.084	100	$1B_1 \rightarrow 1B_1$		0.073	$1B_1 \rightarrow 1B_1$	99.6		
8	0.212 (1712)	$a_g(A_1)$	0.531	100	$1B_1 \rightarrow 1B_1$		0.452	$1B_1 \rightarrow 1B_1$	99		

Table 9.2: Properties of some significant IETS active vibrational modes α of frequency ω and symmetry as specified in the molecular point group (conductance point group), including the relative total intensity I_{inel}^α from Eqn. (9.5), the relative zero-voltage conductance g_α from Eqn. (9.6) evaluated at the Fermi energy E_F , and the identity and contribution of its most significant channel contributor(s), and that as obtained approximately through the replacement of $\bar{\mathbf{A}}^R(E - \omega_\alpha)$ with $\bar{\mathbf{A}}^R(E)$.

9.3 Propensity rules in IETS

Based on this simple formalism, the factors that lead to the propensity of different modes in IETS are depicted graphically in Figure (9.4). The top part is a schematic plot of six characteristic normal modes and their frequencies. The second and third rows show the modulus of the eigenvectors of $(\mathbf{A}^L)^*$ and \mathbf{A}^R associated with the dominant channels through the coupling-weighted molecular density that indicate how transported charges enter and leave the molecular region. These Left and Right pairs of channels are coupled by a molecular vibronic coupling term $|\overline{M}_{ij}^\alpha|^2$ whose origin in terms of interfering atomic contributions and bond contributions is shown in the lower part of the figure.

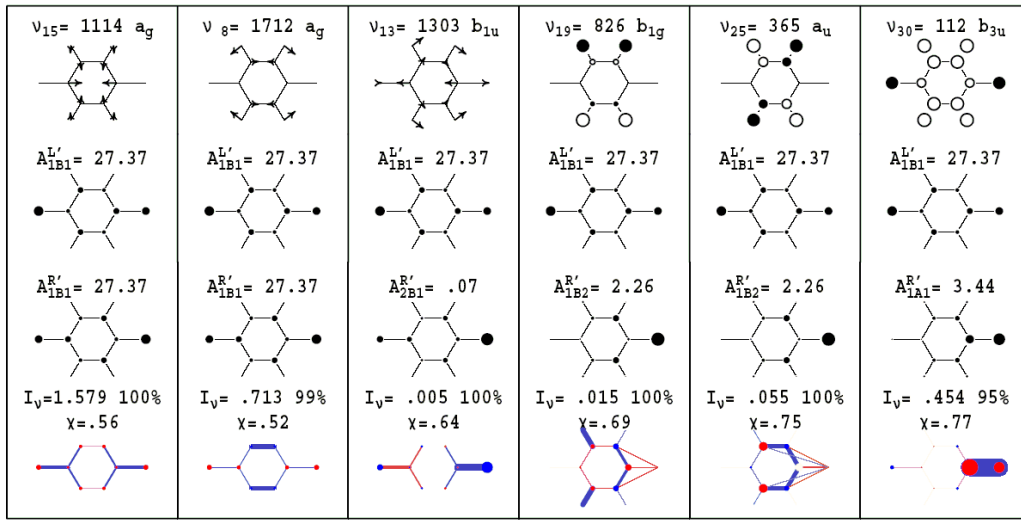


Figure 9.4: Diagrammatic description of the origin of the IETS intensity for six characteristic vibrational modes. First row: depictions of the normal modes, including either arrows for in-plane modes or open and closed circles for out-of-plane modes, along with the mode frequency in cm^{-1} and molecular symmetry. Second and third rows: circles indicating the absolute values of the atomic contributions to the dominant eigenvectors C_i^L of \mathbf{A}^L and C_j^R of \mathbf{A}^R along with the associated eigenvalues $\overline{A}_{ii}^{L,\lambda}$ and $\overline{A}_{jj}^{R,\beta}$, in a.u., from Table (9.1). Fourth row: origin of the vibronic term \overline{M}_{ij}^α that couples these channels expressed in terms of atomic contributions (circles) and bond contributions (lines) colored blue and red to indicate constructively and destructively interfering processes, respectively; also indicated is the total inelastic conductance at E_F of the mode and the percentage contribution arising from the indicated coupled channels (doubled for non-totally-symmetric modes to account also for its symmetry-related counterpart), and the destructive interference indicator χ .

To do this we can expand

$$|\overline{M}_{ij}^\alpha| = \text{Re}(\sum_E \sum_F \beta_{EF}^{ij} e^{-i\phi}), \quad (9.15)$$

where E and F refer to different atoms, ϕ is the phase of the complex number \overline{M}_{ij}^α , and the atomic (diagonal) and bond (off-diagonal) contributions β are defined using:

$$\beta_{EF}^{ij} = \sum_{m \in E} \sum_{n \in F} (C_{im}^L)^* M_{mn}^\alpha C_{nj}^R, \quad (9.16)$$

where $C_{ij}^{L(R)}$ are the elements of the eigenvectors and M_{mn}^α are the vibronic coupling matrix elements in the atomic-orbital basis. The off-diagonal elements of this coupling matrix represent scattering from the bonds of the molecule while the diagonal elements represent scattering off the atoms. Through chemical or other external modifications to the molecule, Fig. (9.4) indicates how the IETS propensities of different modes can be manipulated.

To show how the lower frames of Fig. (9.4) depict the molecular properties, the dominant contributions β_{EF}^{ij} evaluated for the most intense IETS mode, ν_{15} , are given in Table (9.3). The largest contribution (40 % of the total) arises from each of the two C-S bonds. The upper frames in Fig. (9.4) indicate why a large contribution arises from the C-S bonds: both the L and R channel eigenvectors contain components on these atoms, and the vibrational mode acts to change the C-S bond length. In the lower frame of Fig. (9.4), the thick and dark blue lines over the C-S bonds indicate this contribution graphically. From Table (9.3), the next most important contribution is 19 % and arises from each of the C- C_o bonds, where C_o is the carbon ortho to the linked carbon. In Fig. (9.4), the total intensity of blue color for the C-S and C- C_o bonds indicates their relative importance. Blue coloring is used to indicate that the contributions from the C-S and C- C_o bonds add constructively to enhance the inelastic current, their net effect being to generate $2 \times 40\% + 4 \times 19\% = 158\%$ of the current. This exceeds 100 % as the remaining minor contributions to the current, dominated as indicated in Table (9.3) by the atomic S (-8 % each) and C (-4 % each) contributions, act destructively to reduce the current. Contributions that act destructively are indicated in red in Fig. (9.4). The total color density shown in circles for the atomic contributions is scaled to that of the bond vectors.

	S	C	C_o	$C_{o'}$
S	-0.08			
C	0.40	-0.03		
C_o	-0.01	0.19	-0.04	
$C_{o'}$	-0.01	0.02	-0.02	-0.04

Table 9.3: Normalized atomic ($\beta_{EE}^{ij}/\sum_{EF}|\beta_{EF}^{ij}|$) and bond ($(\beta_{EF}^{ij} + \beta_{FE}^{ij})/\sum_{EF}|\beta_{EF}^{ij}|$) contributions to the molecular vibrational couplings between input and output electron scattering channels, $|\overline{M}_{ij}^\alpha|$ from Eqn. (9.15), as visualized in Fig. (9.4); contributions are shown for the sulfur (S), connected carbon (C), its ortho carbon (C_o), and its symmetry-related neighbor ($C_{o'}$).

For each mode depicted in Fig. (9.4), the impact of destructive interference between electron-scattering pathways is quantified using the indicator

$$\chi = 1 - \frac{|\sum_{EF} \beta_{EF}^{ij}|}{\sum_{EF} |\beta_{EF}^{ij}|}, \quad (9.17)$$

which takes on the value of $\chi = 0$ to indicate only constructive interference to $\chi \approx 1$, indicating strong destructive interference. Modes dominated by destructive interference are likely to be highly sensitive to external modifications through modulation of the interference. For the example of ν_{15} considered previously, bond scattering is opposed by atomic scattering so that χ is quite large at 0.56. Of all of the vibrational modes, this mode, the most intense mode, has one of the *lowest* values of χ , however, indicating that interference effects will in general limit the development of simple chemical models for IETS intensity.

From the analysis of the channels propensity rules can also be defined. The most active modes are the a_g modes. Based on the notion that the most intense modes will be those that access the dominant $1B_1$ paths through each of the junction-weighted densities of states, the most active modes are expected to be of A_1 symmetry in the C_{2v} conductance point group. Such modes will have either a_g or b_{1u} symmetry in the full molecular point group, d_{2h} . Indeed, a_g modes are found to be the most active ones, but b_{1u} modes are found to be very weak. To understand this differentiation, we note that the transmission eigenvectors $\mathbf{C}_{1B_1}^{L,R}$ associated with the Left and Right $1B_1$ channels can be represented as a sum of terms each with either a_g or b_{1u} symmetry:

$$\mathbf{C}_{1B_1}^{L,R} = \frac{1}{\sqrt{2}}(\psi_{a_g} \pm \psi_{b_{1u}}) \quad (9.18)$$

where the upper (lower) sign is for the left (right) eigenvector. Substituting Eqn. (9.18) into Eqn. (9.12) splits the sum into four terms:

$$\begin{aligned} \bar{M}_{ij}^\alpha &= \frac{1}{2}(\psi_{a_g})^\dagger \mathbf{M}^\alpha \psi_{a_g} - \frac{1}{2}(\psi_{b_{1u}})^\dagger \mathbf{M}^\alpha \psi_{b_{1u}} + \\ &\quad \frac{1}{2}(\psi_{a_g})^\dagger \mathbf{M}^\alpha \psi_{b_{1u}} - \frac{1}{2}(\psi_{b_{1u}})^\dagger \mathbf{M}^\alpha \psi_{a_g}. \end{aligned} \quad (9.19)$$

The product of the three elements in Eqn. (9.19) must be totally symmetric so only the first two terms may be non zero for a_g modes while only the last two terms are permissible for b_{1u} modes. For a_g modes, the two allowed terms differ fundamentally in nature from each other facilitating an allowed net contribution. However, for the b_{1u} modes, the two non-zero contributions exactly cancel each other, preventing inelastic scattering involving the same input and output channels. Hence the inelastic scattering for the b_{1u} mode ν_{13} shown in Fig. (9.4) involves two *different* B_1 channels, $1B_1$ and $2B_1$, so that the b_{1u} modes thus behave in the same fashion as do all other non-totally-symmetric vibrations. Conceptual approaches that exploit the sparseness properties of \mathbf{I}_L and \mathbf{I}_R alone do lead to the primary propensity rule favoring totally symmetric IETS excitations.

The propensity rules derived by transforming the \mathbf{I} 's parallel these propensity rules and can be thought of as arising through similar arguments and serve to identify the most active modes in IETS. However, through the complete description of the junction-weighted densities of states, it is possible to derive also propensity rules for the next most active vibrations: these will be the ones associated with both the largest and the second largest eigenvalues $\bar{A}_{ii}^{L,\lambda}$, in this case the $1B_1$ and $1A_1$ channels, respectively, which are coupled by

modes of b_{3u} and b_{2g} symmetry. Indeed, modes of both of these symmetries are identified as being quite prolific in Fig. (9.2) and in Table (9.2). Of note is the fact that these modes are out-of-plane modes that do not have a components in the direction of the charge flow; rather, they scatter electrons and holes between σ and π channels.

Within each particular symmetry class, the most active modes are seen from Fig. (9.4) to be those that involve atomic motion on atoms that have large amplitudes in the coupling-weighted Left and Right channels. As a result, a wide variety of scattering paths through the molecule can be invoked. As described earlier, the most intense a_g mode ν_{15} from Fig. (9.4) is an in-plane ring deformation mode that embodies some C-S stretching character, and all parts of the molecule contribute to the scattering. Also shown in Fig. (9.4) is the nature and scattering origin for the next most prolific mode, the a_g C-H bending mode ν_8 . This mode is coupled to some C_o-C_o' stretching character, and it is this that facilitates the inelastic scattering from the input $1B_1$ channel to the output $1B_1$ channel.

For the intense non-totally symmetric modes that scatter charges between σ and π channels, the most active modes are found to be those with significant C and S involvement. The scattering is not generated symmetrically from each end of the molecule, as scattering between input and output channels of the same type is constrained to be, but instead is typically dominated by a single C-S bond. Typifying this behavior is ν_{30} , the b_{3u} mode that couples the two most conductive junction channels $1A_1$ and $1B_1$ (see Table (9.1)). Figure (9.4) shows that the input and output channels both have amplitude on the one C-S bond while the out-of-plane vibration also has C-S amplitude, allowing the σ - π mixing to occur. This mode is indeed the third most active mode calculated for IETS (see Table (9.2)), but, as the bottom frame of Fig. (9.4) indicates, the dominant scattering from the C-S bond is strongly opposed by scattering from the individual C and S atoms. Were it not for this interference, this vibrations would be even more prolific in the calculated IETS. The largest destructive interference found was for the related b_{3u} mode ν_{24} for which $\chi = 0.91$.

Finally, I consider the C-H out-of-plane modes ν_{19} (b_{1g}) and ν_{25} (a_u) that have the same form except for opposite end-to-end symmetry. These modes couple the most prolific and third-most prolific molecule-weighted junction channels $1B_1$ and $1B_2$, but as can be seen from the forms of the channels shown in Fig. (9.4), very few atoms are active in both channels. Hence the scattering is intrinsically weak and contains contributions from non intuitive non bonded 1,3- and 1,4- intermolecular interactions. While these modes are predominantly C-H in character, they do provide scattering through their weak C-C contamination.

9.4 Conclusions

In conclusion, two approaches has been investigated to analyze the IETS signal in a 1,4-benzenedithiol molecule chemisorbed between two gold leads in the context of a full general formalism for non-equilibrium elastic and inelastic conduction processes. In both approaches, the inelastic current is split into a small number of non interfering contributions or channels. The first approach, based on the insight provided by Troisi *et al.* [38, 120] that only a few paths through the junctions are accessible, involves transformation of the

molecule-electrode couplings $\Gamma_{L(R)}$ and reduces dramatically the complexity of the problem. However, detailed insight into the influence of the molecule on these paths is required before the method can be put to practical use in the determination of propensity rules. The second approach provides this insight automatically through the transformation of the $(\mathbf{A}^L)^*$ and \mathbf{A}^R matrices that depicts the density of states of the molecule coupled to the contacts.

The A -channel transformation allows the dominant channels for electron or hole conduction through the junctions, channels of different symmetries, to be identified, leading to propensity rules based on the affect of the normal modes of vibration in scattering charges between these channels. As for molecules such as 1,4-benzenedithiol with dominant π -conduction character, the molecule-weighted junction channel $1B_1$ is very much more prolific than in any other channel. This leads to the first propensity rule that the totally symmetric modes (a_g) dominate IETS as only these can couple $1B_1$ from the Left lead to $1B_1$ in the Right lead. A similar propensity rule is expected for all molecules chemisorbed to gold through sulfur links, independent of the actual identity of the dominant channel. Weaker contributions to IETS are then identified from the nature of the next-most significant molecule-weighted junction channel eigenvalue(s), which for 1,4-benzenedithiol are found to be $1A_1$ and $1B_2$, leading to a propensity for b_{2g} and b_{3u} modes and b_{1g} and a_u modes, respectively, in its IETS.

Once these dominant channels are identified for modes of a particular symmetry type, the most active modes can be determined by examination of how the normal mode affects the atoms accessed by the appropriate molecule-weighted junction channels and the nature of the junction channels: the same atoms must be involved in each channel, and the vibration must perturb these atoms. For coupling between the $1B_1$ and $1B_2$ channels, few atoms are involved in both channels and so the IETS is weak, but the overlap between the $1B_1$ and $1A_1$ channels is large and hence the IETS is strong. These intense IETS modes involve the mixing of molecular σ and π character through out-of-plane C-S distortions. However, a more subtle feature acts to determine the final IETS intensities: the scattering amplitude can be decomposed in terms of interfering contributions associated with scattering from each atomic centre and from each bond in the molecule, and this interference is in general large. A practical consequence of this is that chemical and other variations are likely to modulate the IETS intensity associated with particular modes of vibration. The analysis presented thus provides simple and effective a priori means by which a very complex process involving no formal selection rules can be controlled and manipulated to achieve desired outcomes.

Conclusion

My work was focused in the investigation of some of the effects induced by the vibrations of the molecule to the conductivity in molecular electronic devices. As already mentioned, this work is particular important in order to investigate the stability of molecular devices, evaluating the dissipated power, and to simulate new techniques to probe the molecule, like IETS.

I applied the NEGF machinery up to the first perturbation term to get a consistent set of equations and evaluate the current including the vibrational effects. The code was successful in handling systems at low temperature strongly bounded to the contacts. This is the typical setup of many experiments using molecule on gold surfaces covalently bonded via thiol groups, as in break-junction or self-assembled monolayer experiments.

The application of the code to alkanethiols, Chapter 6, has shown how the vibrational degrees of freedom can play an important role in the final dissipation of the molecule. In particular it has shown the importance in electron scattering of vibrational modes which are localized in the junction region between the molecule and the contacts. This means that to catch the real dissipation effects a good characterization of the surface cannot be neglected. This demonstrate that if the molecule is characterizing the shape of the current-voltage characteristic, the surface is fundamental to get the right magnitude of the current and of the power dissipated, see also Di Ventra *et. al.* [121].

The same results were obtained in the IETS in alkanethiols, were the effect of sulphur-gold interaction was the origin of one of the most intense peak in the spectrum. The IETS has provided to be one of the most interesting topic for the application of the electron-phonon code. In fact, it is a very flexible technique to investigate many aspects of molecular devices which normally are beyond the possibility of more conventional spectroscopy techniques in molecular electronics. In particular I used the simulation of IETS to investigate how the geometry configuration of the molecule between the metallic electrodes and how the junction affects the spectrum. Particular important is this sensitivity to the metal-molecule interface if molecular electronics shall move in the direction of high reproducible devices for industry.

Moreover, from my simulation it is evident that the scattering of electrons in the molecule is a complex interplay between the density of electrons, the external bias applied and the localization of the most relevant vibrational modes. This suggests the possibility to decom-

pose the current into independent channels. Those channels can be labeled following the reduced symmetry point group of the molecule between the electrodes. In case the junction reduces to a simple thiol group which bonds the molecule to the metal, the number of dominant channels reduces drastically. The irreducible representations of those channels, coupled with the symmetry of the modes, has permitted to cast a light to the complicate propensity rules of IETS. Rules which depend on both the molecule and the interfaces with the contacts.

The computational efficiency of DFTB and the flexibility of the code have permitted to implement new features very easily during the proceeding of the PhD. In particular the introduction of symmetry was fundamental to the investigation of selection rules in IETS. This represents probably the largest strength of the method. However, other issues need to be investigated:

- The strength of DFTB relies on the possibility to use a systematic method of parametrization for the zero order Hamiltonian. However apart for organic compounds still a reliable parametrization for organic elements is missing with metal, in particular with gold.
- The inclusion of the charge polarization induced by the bias is fundamental for higher voltages. The merging of the electron-phonon code with the Poisson solving gDFTB is thus a mandatory future step.
- The correlation between electrons must be improved beyond the mean field approximation implemented in DFTB. Many studies [122] show that the charge correlation plays an important role in the alignment of the HOMO-LUMO gap and the Fermi energy of the contacts, fundamental aspect for every quantitative evaluation of the current. At the moment a scheme to include a quasiparticle correction, at the so called *GW* level, is under development [123, 124].

Concluding, this work was motivated by the large impact that molecular electronics has mostly in the scientific community. Despite many years of research, the field has still not reached a degree of maturity that permits the transition from the laboratories to the industry. However, the idea of using a single molecule to characterize the entire device is revolutionary for the impact it can have to the concept of electronics and in the entire engineering field. It is certainly a step to get closer to the workings of nature, considering that all the lifeforms on this planet are nothing else that extremely complex self-assembled systems made of molecules.

The possibilities are very large, but the theoretical, as the experimental, work is extremely challenging. Already the definition of the system is rather complicate considering that in the same system we have to face and describe at the same level of accuracy a bulk region (the contacts), a surface (the leads) and a molecular region. This puts immediately some constrains to the kind of theoretical methods that can be used, considering that *ab-initio* quantum chemistry methods are at the moment unable to handle such large systems.

Since the first seminal paper about molecular electronics [125], many issues have been addressed from the theoretical point of view, but many others need to be fully investigated.

Main fundamental points are still under debate: is a molecule mostly a wire or more a quantum dot? Which is the effect of the contacts and especially the surface on the conductivity? Which role do static and dynamic correlation play in conduction when considering also effects such as Coulomb blockade? How can the spin-spin interaction change the entire picture?

It is clear that only a full description of all these issues together can really address and solve the problem of theoretical description of molecular electronic conductivity.

At the moment, the best compromise between all these issues remains the Green's function approach using DFT as starting point. However, it is now clear that the method is unable to completely handle many fundamental characteristics of the molecular conductivity. There are basically two ways to go beyond a DFT description: changing directly the DFT method as starting point for the Hamiltonian or refining the calculation with corrections at the Green's function level. This second approach has been followed in our group in the gDFTB codes as, i. e., by the electron-electron correlation correction with *GW*.

However, the author suggests that in the future a more radical change in the approach will be needed to really overcome the problems that cannot be fully described at the DFT level of theory, many candidates for hybrid methodologies already exist, like time-dependent DFT (TDDFT).

Atomic Units

The *atomic units* (a.u.) are a set of units specifically designed to fulfil two specific purposes: first, present the results from atomistic calculations in digestible numbers and, second, decouple the numerical calculations from specific values of fundamental constants. To see how these units arise naturally let us consider the Schrödinger equation for the hydrogen atom. In SI (*Systeme International d'Unites*) units, we have

$$\left[-\frac{\hbar^2}{2m_e} \nabla^2 - \frac{e^2}{4\pi\epsilon_0 r} \right] \phi = \epsilon \phi \quad (\text{A.1})$$

where \hbar is the Plank's constant divided by 2π , m_e is the mass of the electron. To cast this equation into dimensionless form we let x, y and $z \rightarrow \lambda x', \lambda y'$ and $\lambda z'$ and obtain

$$\left[-\frac{\hbar^2}{2m_e \lambda^2} \nabla'^2 - \frac{e^2}{4\pi\epsilon_0 \lambda r'} \right] \phi' = \epsilon \phi' \quad (\text{A.2})$$

The constant in front of the kinetic and potential energy operators can then be factored, provided we choose λ such that

$$\frac{\hbar^2}{m_e \lambda^2} = \frac{e^2}{4\pi\epsilon_0 \lambda} = \epsilon_a \quad (\text{A.3})$$

where ϵ_a is the atomic unit energy called *Hartree*. Solving Eqn. (A.2) for λ we find

$$\lambda = \frac{4\pi\epsilon_0 \hbar^2}{m_e e^2} = a_0 \quad (\text{A.4})$$

Thus λ is just the Bohr radius a_0 which is the atomic unit of length called a *Bohr*. Finally, since

$$\epsilon_a \left[-\frac{1}{2} \nabla'^2 - \frac{1}{r'} \right] \phi' = \epsilon \phi' \quad (\text{A.5})$$

if we let $\varepsilon' = \varepsilon/\varepsilon_a$, we obtain the dimensionless equation

$$\left[-\frac{1}{2}\nabla'^2 - \frac{1}{r'} \right] \phi' = \varepsilon' \phi' \quad (\text{A.6})$$

which is the Schrödinger equation in atomic units.

Physical quantity	Conversion factor X	Value of X (SI)
Length	a_0	$5.2918 \times 10^{-11} \text{ m}^{-1}$
Mass	m_e	$9.1095 \times 10^{-31} \text{ Kg}$
Charge	e	$1.6022 \times 10^{-19} \text{ C}$
Energy	ε_a	$4.3598 \times 10^{-18} \text{ J}$
Action	\hbar	$1.0546 \times 10^{-34} \text{ Js}$

Table A.1: Conversion of atomic units to SI units.

The solution of this equation for the ground state of the hydrogen atom yields an energy ε' equal to -0.5 atomic units. Table (A.1) gives the conversion factor X between atomic units and SI units, such that the SI value of any quantity Q is related to its value in atomic units Q' by

$$Q = XQ'. \quad (\text{A.7})$$

Conversion factors for a few other units, which are not related to SI but which are necessary to read the existing literature, are so follows. One atomic unit of length equals 0.52918 Angströms (\AA) and one atomic unit of energy equals 27.211 electron volts (eV) or 627.51 kcal/mole.

Surface Green's Function: Decimation

Technique

In this appendix the algorithm to evaluate the contacts self-energies is discussed. The evaluation of the self-energies, from Eqn. (5.11) Chapter 5, is related to the computation of the so called surface Green's functions \mathbf{g}_L^r and \mathbf{g}_R^r of the contacts. These Green's functions are the propagators of the two contacts assuming that they are disconnected from the bridge. To evaluate them it is generally used a *decimation* algorithm, following the Guinea *et al.* [126] scheme.

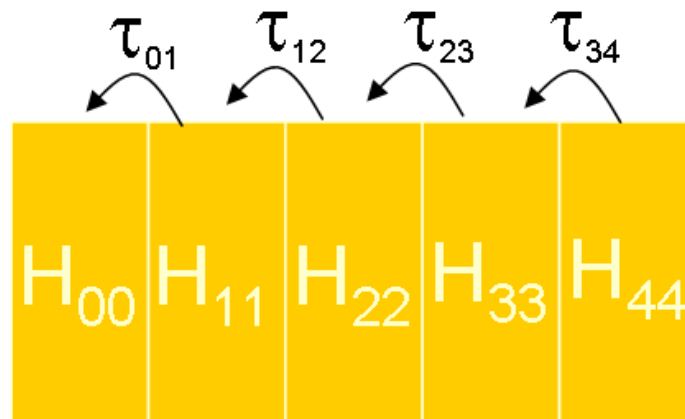


Figure B.1: The contact can be seen as a semi-infinite repetition of a fundamental supercell called principal layer (PL). The size of the principal layer is chosen large enough in the way that only adjacent PLs interact via the τ blocks.

In Fig. (B.1) it is shown schematically the shape of one contact. We can define them as the repetition of an infinite number of connected subsystem called principal layers (PL). The PLs are defined in such a way that only nearest neighbor interact. The Dyson's equation for the infinite system can be written in terms of block matrices as

$$\begin{pmatrix} \varepsilon \mathbf{S}_{00} - \mathbf{H}_{00} & \varepsilon \mathbf{S}_{01} - \tau_{01} & 0 & 0 & \cdots \\ \varepsilon \mathbf{S}_{10} - \tau_{10} & \varepsilon \mathbf{S}_{11} - \mathbf{H}_{11} & \varepsilon \mathbf{S}_{12} - \tau_{12} & 0 & \\ 0 & \varepsilon \mathbf{S}_{21} - \tau_{21} & \varepsilon \mathbf{S}_{22} - \mathbf{H}_{22} & \varepsilon \mathbf{S}_{23} - \tau_{23} & \\ 0 & 0 & \varepsilon \mathbf{S}_{32} - \tau_{32} & \varepsilon \mathbf{S}_{33} - \mathbf{H}_{33} & \\ \vdots & & & & \ddots \end{pmatrix} \cdot \begin{pmatrix} \mathbf{g}_{00}^r & \mathbf{g}_{01}^r & \mathbf{g}_{02}^r & \mathbf{g}_{02}^r & \cdots \\ \mathbf{g}_{10}^r & \mathbf{g}_{11}^r & \mathbf{g}_{12}^r & \mathbf{g}_{13}^r & \\ \mathbf{g}_{20}^r & \mathbf{g}_{21}^r & \mathbf{g}_{22}^r & \mathbf{g}_{23}^r & \\ \mathbf{g}_{30}^r & \mathbf{g}_{31}^r & \mathbf{g}_{32}^r & \mathbf{g}_{33}^r & \\ \vdots & & & & \ddots \end{pmatrix} = \mathbf{1} \quad (\text{B.1})$$

where $\varepsilon = (E + i\eta)$ with η a positive infinitesimal quantity (in the calculations was used 10^{-6}). The subindexes label the different PLs and the block \mathbf{g}_{mn} is the propagator connecting the m^{th} and n^{th} layer. For an ideal system we can assume that the blocks of the PLs are all equal ($\mathbf{H}_{00} = \cdots = \mathbf{H}_{mm} = \mathbf{H}_{PL}$) as the coupling terms ($\tau_{10} = \cdots = \tau_{nm} = \tau$). Moreover the coupling terms are related by the following relation: $\tau_{mn} = \tau_{nm}^\dagger$. The same relations are for the overlap matrix \mathbf{S} . We can separate the Dyson's equations connecting the surface layer, or 0th layer, with the rest, obtaining a set of linear equations

$$\begin{aligned} (\varepsilon \mathbf{S}_{PL} - \mathbf{H}_{PL}) \mathbf{g}_{00}^r - (\varepsilon \mathbf{S}_\tau - \tau) \mathbf{g}_{10}^r &= \mathbf{1} \\ (\varepsilon \mathbf{S}_{PL} - \mathbf{H}_{PL}) \mathbf{g}_{10}^r - (\varepsilon \mathbf{S}_\tau - \tau) \mathbf{g}_{20}^r - (\varepsilon \mathbf{S}_\tau^\dagger - \tau^\dagger) \mathbf{g}_{00}^r &= \mathbf{0} \\ (\varepsilon \mathbf{S}_{PL} - \mathbf{H}_{PL}) \mathbf{g}_{20}^r - (\varepsilon \mathbf{S}_\tau - \tau) \mathbf{g}_{30}^r - (\varepsilon \mathbf{S}_\tau^\dagger - \tau^\dagger) \mathbf{g}_{10}^r &= \mathbf{0} \\ &\cdots \\ (\varepsilon \mathbf{S}_{PL} - \mathbf{H}_{PL}) \mathbf{g}_{m0}^r - (\varepsilon \mathbf{S}_\tau - \tau) \mathbf{g}_{m+1,0}^r - (\varepsilon \mathbf{S}_\tau^\dagger - \tau^\dagger) \mathbf{g}_{m-1,0}^r &= \mathbf{0} \\ &\cdots \end{aligned} \quad (\text{B.2})$$

In the latter set of equations we can express all the blocks \mathbf{g}_{m0}^r , with m odd, as the following:

$$\mathbf{g}_{m0}^r = (\varepsilon \mathbf{S}_{PL} - \mathbf{H}_{PL})^{-1} [(\varepsilon \mathbf{S}_\tau - \tau) \mathbf{g}_{m+1,0}^r + (\varepsilon \mathbf{S}_\tau^\dagger - \tau^\dagger) \mathbf{g}_{m-1,0}^r] \quad (\text{B.3})$$

The new expression for every odd blocks of the Green's function can be substituted in the neighbor equations, getting the following

$$\begin{aligned}
\mathbf{W}_s^1 \mathbf{g}_{00}^r + \tau_1^1 \mathbf{g}_{20}^r &= \mathbf{1} \\
\mathbf{W}_b^1 \mathbf{g}_{20}^r + \tau_1^1 \mathbf{g}_{40}^r + \tau_2^1 \mathbf{g}_{00}^r &= \mathbf{0} \\
\mathbf{W}_b^1 \mathbf{g}_{60}^r + \tau_1^1 \mathbf{g}_{20}^r + \tau_2^1 \mathbf{g}_{20}^r &= \mathbf{0} \\
\mathbf{W}_b^1 \mathbf{g}_{80}^r + \tau_1^1 \mathbf{g}_{20}^r + \tau_2^1 \mathbf{g}_{40}^r &= \mathbf{0} \\
&\dots \\
\mathbf{W}_s^1 \mathbf{g}_{m0}^r + \tau_1^1 \mathbf{g}_{m+2,0}^r + \tau_2^1 \mathbf{g}_{m-2,0}^r &= \mathbf{0} \\
&\dots
\end{aligned} \tag{B.4}$$

where

$$\begin{aligned}
\mathbf{W}_s^1 &= (\varepsilon \mathbf{S}_{PL} - \mathbf{H}_{PL}) - (\varepsilon \mathbf{S}_\tau - \tau)(\varepsilon \mathbf{S}_{PL} - \mathbf{H}_{PL})^{-1}(\varepsilon \mathbf{S}_{PL}^\dagger - \tau^\dagger) \\
\mathbf{W}_b^1 &= (\varepsilon \mathbf{S}_{PL} - \mathbf{H}_{PL}) - (\varepsilon \mathbf{S}_{PL} - \tau)(\varepsilon \mathbf{S}_{PL} - \mathbf{H}_{PL})^{-1}(\varepsilon \mathbf{S}_\tau^\dagger - \tau^\dagger) + \\
&\quad - (\varepsilon \mathbf{S}_{PL}^\dagger - \tau^\dagger)(\varepsilon \mathbf{S}_{PL} - \mathbf{H}_{PL})^{-1}(\varepsilon \mathbf{S}_\tau - \tau) \\
\tau_1^1 &= -(\varepsilon \mathbf{S}_\tau - \tau)(\varepsilon \mathbf{S}_{PL} - \mathbf{H}_{PL})^{-1}(\varepsilon \mathbf{S}_\tau - \tau) \\
\tau_2^1 &= -(\varepsilon \mathbf{S}_\tau^\dagger - \tau^\dagger)(\varepsilon \mathbf{S}_{PL} - \mathbf{H}_{PL})^{-1}(\varepsilon \mathbf{S}_\tau^\dagger - \tau^\dagger)
\end{aligned} \tag{B.5}$$

We have actually recovered Eqn. (B.2) with new renormalized parameters. The first equation in Eqn. (B.4) connects now the renormalized 0^{th} and 2^{nd} layers and τ_1 and τ_2 are giving the effective interaction between them, while \mathbf{W}_s is the effective matrix of $(\varepsilon \mathbf{S}_{PL} - \mathbf{H}_{eff})$ for layer “0”, that means the layer in contact with the device.

We proceed in successive steps by eliminating the Green’s functions of the next alternating layers, which will now be $\mathbf{g}_{2n,0}^r$ for odd n . This procedure can be iterated, obtaining at each step the corresponding renormalized \mathbf{W}_b , \mathbf{W}_s , τ_1 and τ_2 matrices relating to those of the previous step in the following way:

$$\begin{aligned}
\mathbf{W}_s^i &= \mathbf{W}_s^{i-1} - \tau_{i-1}(\mathbf{W}_b^{i-1})^{-1}\tau_2^{i-1} \\
\mathbf{W}_b^i &= \mathbf{W}_b^{i-1} - \tau_{i-1}(\mathbf{W}_b^{i-1})^{-1}\tau_2^{i-1} - \tau_2^{i-1}(\mathbf{W}_b^{i-1})^{-1}\tau_1^{i-1} \\
\tau_1^i &= -\tau_1^{i-1}(\mathbf{W}_b^{i-1})^{-1}\tau_1^{i-1} \\
\tau_2^i &= -\tau_2^{i-1}(\mathbf{W}_b^{i-1})^{-1}\tau_2^{i-1}.
\end{aligned} \tag{B.6}$$

After the i^{th} step τ_1^i and τ_2^i give the effective interaction between layers “0” and 2^i having renormalized out those in between. We can thus expect both τ_1 and τ_2 to decrease for any energy value with increasing number of steps, becoming quickly negligible as the layers they effectively connect are just too far apart. The surface and bulk layers are then practically decoupled, and we are left with the equations:

$$\begin{aligned}\mathbf{W}_s^N \mathbf{g}_{00}^r &= \mathbf{1} \\ \mathbf{W}_b^N \mathbf{g}_{2^N n, 0}^r &= \mathbf{0}\end{aligned}\tag{B.7}$$

where N is the number of steps necessary to achieve convergence in the iteration process. Convergence is achieved when τ_1^N and $\tau_2^N < \delta$ where δ is a defined small threshold. The Green's function for the surface is therefore well described by

$$\mathbf{g}_{00}^r = (\mathbf{W}_s^N)^{-1}\tag{B.8}$$

In this example we have assumed that the chain of PLs grows in the right direction, which is the case of the right contact. The same algorithm can be applied for the left contact, where the PLs grows in the left direction, just exchanging τ_1 with τ_2 in the equations. In order to run this algorithm we need only the Hamiltonian of two PLs and their coupling for both the contacts.

Bibliography

- [1] International Technology Roadmap for Semiconductors (Semiconductor Industry Association), (2005).
- [2] G. Moore. Cramming more components onto integrated circuits. *Electronics*, 38:114–117, (1965).
- [3] R. Chau, S. Datta, and A. Majumdar. Opportunities and challenges of iii-v nanoelectronics for future high-speed, low-power logic applications. *IEEE CSIC Symposium Technical Digest*, pages 17–20, (2005).
- [4] G. D. Wilk, R. M. Wallace, and J. M. Anthony. High-kappa gate dielectrics: Current status and materials properties considerations. *J. Appl. Phys.*, 89:5243–5275, (2001).
- [5] H. S. P. Wong, D. J. Frank, P. M. Solomon, C. H. J. Wann, and J. J. Welser. Nanoscale CMOS. *Proc. IEEE*, 87:537–570, (1999).
- [6] L. L. Chang, M. Jeong, and M. Yang. CMOS circuit performance enhancement by surface orientation optimization. *IEEE Trans. Electron. Dev.*, 51:1621–1627, (2004).
- [7] D. A. Muller. A sound barrier for silicon? *Nature Mater.*, 4:645–647, (2005).
- [8] M. A. Reed. Molecular electronics: Back under control. *Nature Mater.*, 3:286–287, (2004).
- [9] C. A. Richter, D. R. Stewart, D. A. A. Ohlberg, and R. Stanley Williams. Electrical characterization of Al/AlOx/molecule/Ti/Al devices. *Appl. Phys. A*, 80:1355–1362, (2005).

-
- [10] W. Y. Wang, T. H. Lee, and M. A. Reed. Electronic transport in molecular self-assembled monolayer devices. *Proc. IEEE*, 93:1815–1824, (2005).
- [11] J. Park, A. N. Pasupathy, J. I. Goldsmith, C. Chang, Y. Yaish, J. R. Petta, M. Rinkoski, J. P. Sethne, H. D. Abruna, P. L. McEuen, and D. C. Ralph. Coulomb blockade and the Kondo effect in single-atom transistors. *Nature*, 417:722, (2002).
- [12] J. Chen and M. A. Reed. Electronic transport of molecular systems. *Chem. Phys.*, 281:127, (2002).
- [13] M. A. Reed, C. Zhou, C. J. Muller, T. P. Burgin, and J. M. Tour. Conductance of a Molecular Junction. *Science*, 278 (5336):252, (1997).
- [14] C. Zhou, C. Muller, M. Deshpande, J. Sleight, and M. A. Reed. Microfabrication of a mechanically controllable break junction in silicon. *App. Phys. Lett.*, 76:1160, (1995).
- [15] J. van Ruitenbeek, A. Alvarez, I. Pineyro, C. Grahmann, P. Joyez, M. Devoret, D. Esteve, and C. Urbina. Adjustable nanofabricated atomic size contacts. *Rev. of Scien. Inst.*, 67:108, (1996).
- [16] C. Muller, J. van Ruitenbeek, and L. de Jongh. Experimental observation of the transition from weak link to tunnel junction. *Physica C*, 191:485, (1992).
- [17] E. Sheer, P. Joyez, D. Esteve, C. Urbina, and M. Devoret. Conduction channels transmissions of atomic size aluminium contacts. *Phys. Rev. Lett.*, 78:3535, (1997).
- [18] J. Reichert, R. Ochs, D. Beckmann, H. Weber, M. Mayor, and H. von Löhneysen. Driving current through single organic molecules. *Phys. Rev. Lett.*, 88:176804, (2002).
- [19] H. Weber, J. Reichert, F. Weigend, R. Ochs, D. Beckmann, M. Mayor, R. Ahlrichs, and H. von Löhneysen. Electronic transport through single conjugated molecules. *Chem. Phys.*, 281:113–125, (2002).
- [20] M. Mayor, C. von Hänisch, H. Weber, J. Reichert, and D. Beckmann. A trans-Platinum (II) complex as a single-molecule insulator. *Angw. Chem. Int. Ed.*, 41 (7):1183, (2002).
-

-
- [21] C. Kergueris, J. P. Bourgoin, S. Palacin, D. Esteve, C. Urbina, M. Magoga, and C. Joachim. Electron transport through a metal-molecule-metal junction. *Phys. Rev. B*, 59:12505, (1999).
- [22] C. Lau, D. Stewart, R. Williams, and M. Bockrath. Direct observation of nanoscale switching centers in metal/molecule/metal structures. *Nano Lett.*, 4:569, (2004).
- [23] X. Cui, A. Primak, X. Zarate, J. Tomfohr, O. Sankey, A. Moore, T. Moore, D. Gust, G. Haris, and S. Lindsay. Reproducible measurements of single-molecule conductivity. *Science*, 294:571, (2001).
- [24] L. Patrone, S. Palacin, J. Bourgoin, J. Lagoute, T. Zambelli, and S. Gauthier. Direct comparison of the electronic coupling efficiency of sulfur and selenium anchoring groups for molecules adsorbed onto gold electrodes. *Chem. Phys.*, 281:325–332, (2002).
- [25] C. Collier, G. Mattersteig, E. Wong, Y. Luo, K. Beverly, J. Samapalo, F. Raymo, J. Stoddart, and J. Heath. A [2]Catenane-based solid state electronically reconfigurable switch. *Science*, 289:1172, (2000).
- [26] Z. Donhauser, B. Mantooth, K. Kelly, L. Bumm, J. Monnell, J. Stapleton, D. Price Jr., A. Rawlett, D. Allara, J. Tour, and P. Weiss. Conductance switching in single molecules through conformational changes. *Science*, 292:2303, (2001).
- [27] C. Zhou, M. R. Deshpande, M. A. Reed, L. Jones II, and J. M. Tour. Nanoscale metal/self-assembled monolayer/metal heterostructures. *Appl. Phys. Lett.*, 71:611, (1997).
- [28] Y. Kervennic, D. Vanmaekelbergh, L. Kouwenhoven, and H. Van der Zant. Planar nanocontacts with atomically controlled separation. *App. Phys. Lett.*, 83:3782, (2003).
- [29] H. Park, A. Lim, A. Alivisatos, J. Park, and P. McEuen. Fabrication of metallic electrodes with nanometer separation by electromigration. *App. Phys. Lett.*, 75:301, (1999).
- [30] M. Lambert, M. Goffman, J. Bourgoin, and P. Hesto. Fabrication and characterisation of sub-3 nm gaps for single-cluster and single-molecule experiments. *Nanotechnology*, 14:772, (2003).
-

-
- [31] S. Khondaker and Z. Yao. Fabrication of nanometer-spaced electrodes using gold nanoparticles. *App. Phys. Lett.*, 81:4613, (2002).
- [32] B. Xu and N. J. Tao. Measurement of single-molecule resistance by repeated formation of molecular junctions. *Science*, 301:1221, (2003).
- [33] L. Bumm, J. Arnold, M. Cygan, T. Dunbar, T. Burgin, L. Jones II, D. Allara, J. Tour, and P. Weiss. Are single molecular wires conducting? *Science*, 271:1705, (1996).
- [34] X. Xiao, B. Xu, and N. Tao. Measurement of single molecule conductance: benzendithiol and benzendimethanethiol. *Nano Lett.*, 4:267, (2004).
- [35] P. K. Hansma. *Tunneling Spectroscopy*. Plenum Press, New York, 1982.
- [36] J. T. Yates and T. E. Madey. *Vibrational Spectroscopy of Molecules on Surfaces*. Plenum Press, New York, 1987.
- [37] K.W. Hipps and U. Mazur. Vibrational and Low-Lying Electronic Transitions in Tetraalkylammonium Salts of CoBr_4^{2-} , CoCl_4^{2-} , $\text{Co}(\text{CNS})_4^{2-}$ As Observed by Raman, Infrared, and Tunneling Spectroscopies. *J. Phys. Chem.*, 91:5218, (1987).
- [38] A. Troisi and M. A. Ratner. Molecular transport junctions: Propensity rules for inelastic electron tunneling spectra. *Nano Lett.*, 6:1784, (2006).
- [39] N. Lorente, M. Persson, L. J. Lauhon, and W. Ho. Symmetry Selection Rules for Vibrationally Inelastic Tunneling. *Phys. Rev. Lett.*, 86:2593, (2001).
- [40] N. Lorente and M. Persson. Theory of Single Molecule Vibrational Spectroscopy and Microscopy. *Phys. Rev. Lett.*, 85:2997, (2000).
- [41] H. Kato and H. Shinohara. Spatially dependent inelastic tunneling in a single metallofullerene. *Phys. Rev. Lett.*, 94:136802, (2005).
- [42] Y.-C. Chen, M. Zwolak, and M. Di Ventra. Inelastic effects on the transport properties of alkanethiols. *Nano Lett.*, 5:621, (2005).
-

-
- [43] M. Galperin, M. A. Ratner, and A. Nitzan. On the line widths of vibrational features in inelastic electron tunneling spectroscopy. *Nano Lett.*, 4:1605, (2004).
- [44] Tikhodeev and H. Ueba. Relation between inelastic electron tunneling and vibrational excitation of single adsorbates on metal surfaces. *Phys. Rev. B*, 70:125414, (2004).
- [45] A. Troisi, M. A. Ratner, and A. Nitzan. Vibronic effects in off-resonant molecular wire conduction. *J. Chem. Phys.*, 118:6072, (2003).
- [46] J. Jiang, M. Kula, W. Lu, and Y. Luo. First-principles simulations of inelastic electron tunneling spectroscopy of molecular electronic devices. *Nano Lett.*, 5:1551, (2005).
- [47] Y. Meir and N. Wingreen. Landauer formula for the current through an interacting electron region. *Phys. Rev. Lett.*, 68:2512, (1992).
- [48] M. Büttiker. Four terminal phase-coherent conductance. *Phys. Rev. Lett.*, 57:1761, (1986).
- [49] M. Büttiker, Y. Imry, R. Landauer, and S. Pinhas. Generalized many-channel conductance formula with application to small rings. *Phys. Rev. B*, 31:6207, (1985).
- [50] G. D. Mahan. *Many-Particle Physics*. Plenum, second edition, 1993.
- [51] R. D. Mattuck. *A Guide to Feynman Diagrams in the Many-Body Problem*. Dover, second edition, 1992.
- [52] A. L. Fetter and J. D. Waleka. *Quantum Theory of Many-Particle System*. Dover, first edition, 2003.
- [53] S. Datta. *Electronic Transports in Mesoscopic Systems*. Cambridge, 1995.
- [54] T. N. Todorov. Tight-binding simulation of current-carrying nanostructures. *J. Phys. Cond. Matt.*, 14:3049, (2002).
- [55] L. V. Keldysh. Diagram technique for non-equilibrium processes. *Soviet Physics JETP*, 20:1018, (1964).
-

-
- [56] A. Pecchia, G. Romano, and A. Di Carlo. Theory of heat dissipation in molecular electronics. *Phys. Rev. B*, 75:035401, (2007).
- [57] C. Caroli, R. Combescot, P. Nozieres, and D. Saint-James. Direct calculation of the tunneling current. *J. Phys. C: Solid St. Phys.*, 4:916, (1971).
- [58] Leo P. Kadanoff and Gordon Baym. *Quantum Statistical Mechanics*. W. A. Benjamin, 1962.
- [59] M. Gell-Mann and F. E. Low. Quantum Electrodynamics at small distances. *Phys. Rev*, 95:1300, (1954).
- [60] T. Frederiksen, M. Paulsson, M. Brandbyge, and J. Antti-Pekka. Inelastic transport theory from first-principles: methodology and applications for nanoscale devices. *cond-matt*, (2006).
- [61] Hartmut Haug and Antti-Pekka Jaho. *Quantum Kinetics in Transport and Optics of Semiconductors*. Springer, 1996.
- [62] T. Frauenheim, G. Seifert, M. Elstner, T. Niehaus, C. Koeler, M. Amkreutz, M. Sternberg, Z. Hajnal, A. Di Carlo, and S. Suhai. Atomistic simulations of complex materials: ground-state and excited-state properties. *J. Phys.: Condensed Matter*, 14:3015, (2002).
- [63] T. Frauenheim, G. Seifert, M. Elstner, Z. Hajnal, G. Jungnickel, D. Porezag, S. Suhai, and R. Scholz. A Self-Consistent Charge Density-Functional Based Tight-Binding Method for Predictive Materials Simulations in Physics, Chemistry and Biology. *Phys. Stat. Sol. (b)*, 217(1):41, (2000).
- [64] M. Elstner, D. Porezag, G. Jungnickel, J. Elsner, M. Haugk, T. Frauenheim, S. Suhai, and G. Seifert. Self-consistent-charge density-functional tight-binding method for simulations of complex materials properties. *Phys. Rev. B*, 58:7260, (1998).
- [65] R. M. Dreizler and E. K. U. Gross. *Density Functional Theory*. Springer, Berlin and Heidelberg, 1990.
- [66] R. O. Jones and O. Gunnarsson. The density functional formalism, its application and prospects. *Rev. Mod. Phys.*, 61:689, (1989).
-

-
- [67] L. H. Thomas. The calculation of atomic fields. *Proc. Camb. Phil. Soc.*, 23:542, (1926).
- [68] E. Fermi. Eine statistische Methode zur Bestimmung einiger Eigenschaften des Atoms und ihre Anwendung auf die Theorie des periodischen Systems der Elemente. *Z. Phys.*, 48:73, (1928).
- [69] W. Kohn. Nobel lecture: Electronic structure of matter-wave functions and density functionals. *Rev. Mod. Phys.*, 71:1253, (1999).
- [70] J. F. Janak. Proof that $\partial E/\partial n = \epsilon_i$ in density-functional theory. *Phys. Rev. B*, 18:7165, (1978).
- [71] J. C. Slater and G. F. Koster. Simplified LCAO method for the periodic potential problem. *Phys. Rev.*, 94:1498, (1954).
- [72] G. Seifert, H. Eschrig, and W. Bieger. Eine approximative Variante des LCAO- X_α Verfahrens. *Z. Phys. Chem.*, 267:529, (1986).
- [73] J. A. Pople, D. P. Santry, and G. A. Segal. Approximate self-consistent molecular orbital theory. I. Invariant procedures. *J. Chem. Phys.*, 43:S129, (1965).
- [74] M. Scholz and H.-J. Koehler. *Quantenchemische Naehungsverfahren und ihre Anwendung in der organischen Chemie, vol. 3 of Quantenchemie-Ein Lehrgang*. Deutscher Verlag der Wissenschaften, 1981.
- [75] J. A. Pople and D. L. Beveridge. *Approximate Molecular Orbital Theory*. McGraw Hill, New York, 1970.
- [76] J. R. Reimers, Z. L. Cai, A. Bilić, N. S. Hush, and N. Y. Ann. *Acad. Sci.*, 235:1006, (2003).
- [77] R. Neumann, R. H. Nobes, and N. C. Handy. *Molec. Phys.*, 87:1, (1996).
- [78] Z.-L. Cai and J. R. Reimers. Application of time-dependent density-functional theory to the ${}^3\Sigma_u^-$ first excited state of H_2 . *J. Chem. Phys.*, 112:527, (2000).
-

-
- [79] G. C. Solomon, J. R. Reimers, and N. S. Hush. Single molecule conductivity: The role of junction-orbital degeneracy in the artificially high currents predicted by ab initio approaches. *J. Chem. Phys.*, 121:6615, (2004).
- [80] J. Jortner, A. Nitzan, and M. A. Ratner. *Lecture Notes in Physics: Introducing Molecular Electronics*.
- [81] O. Gunnarsson and B. I. Lundqvist. Exchange and correlation in atoms, molecules, and solids by the spin-density-functional formalism. *Phys. Rev. B*, 13:4274, (1976).
- [82] A. Bilić, J. R. Reimers, and N. S. Hush. The structure, energetics, and nature of the chemical bonding of phenylthiol adsorbed on the Au(111) surface: Implications for density-functional calculations of molecular-electronic conduction. *J. Chem. Phys.*, 122:094708, (2005).
- [83] T. A. Niehaus, S. Suhai, F. Della Sala, P. Lugli, M. Elstner, G. Seifert, and T. Frauenheim. Tight-binding approach to time-dependent density-functional response theory. *Phys. Rev. B*, 63:085108/1, (2001).
- [84] Z.-L. Cai, K. Sendt, and J. R. Reimers. Failure of density-functional theory and time-dependent density-functional theory for large extended π systems. *J. Chem. Phys.*, 117:5543, (2002).
- [85] S. J. A. van Gisbergen, P. R. T. Schipper, O. V. Gritensko, E. J. Baerends, J. D. Snijders, B. Champagne, and B. Kirtman. Electric field dependence of the exchange-correlation potential in molecular chains. *Phys. Rev. Lett.*, 83:694, (1999).
- [86] A. Pecchia and A. Di Carlo. Atomistic theory of transport in organic and inorganic nanostructures. *Rep. Prog. Phys.*, 67:1497, (2004).
- [87] B. A. Mantooth, Z. J. Donauser, K. F. Kelly, and P. S. Weiss. Cross-correlation image tracking for drift correction and adsorbate analysis. *Rev. Scien. Instr.*, 73:313, (2002).
- [88] M. Galperin, M. A. Ratner, and A. Nitzan. Molecular transport junctions: Vibrational effects. *J. Phys. Cond. Matt.*, 19:103201, (2007).
-

- [89] J. G. Kushmerick, J. Lazorcik, C. H. Patterson, R. Shashidhar, D. S. Seferos, and G. C. Bazan. Vibronic contributions to charge transport across molecular junctions. *Nano Lett.*, 4:639, (2004).
- [90] W. L. Wang, I. Kretzschmar, and M. Reed. Inelastic electron tunneling spectroscopy of an alkanedithiol self-assembled monolayer. *Nano Lett.*, 4:643, (2004).
- [91] Y. Yourdshahyan, H. K. Zhang, and A. M. Rappe. n-alkyl thiol head-group interactions with the Au(111) surface. *Phys. Rev. B*, 63:081405, (2001).
- [92] J. Gottschalck and B. J. Hammer. A density functional theory study of the adsorption of sulfur, mercapto, and methylthiolate on Au(111). *J. Chem. Phys.*, 116:784, (2002).
- [93] H. S. Kato, J. Noh, M. Hara, and M. Kawai. An HREELS Study of Alkanethiol Self-Assembled Monolayers on Au(111). *J. Phys. Chem. B*, 106:9655, (2002).
- [94] M. A. Bryant and J. E. Pemberton. Surface Raman Scattering of Self-Assembled Monolayers Formed from 1-Alkanethiols: Behavior of Films at Au and Comparison to Films at Ag. *J. Am. Chem. Soc.*, 113:8284, (1991).
- [95] C. Castiglioni, M. Gussoni, and G. Zerbi. Charge mobility in σ -bonded molecules: The infrared spectrum of polymethylene chains in the solid and liquid phases. *J. Chem. Phys.*, 95:7144, (1991).
- [96] Y.-C. Chen, M. Zwolak, and M. Di Ventra. Inelastic current-voltage characteristics of atomic and molecular junctions. *Nano Lett.*, 4:1709, (2004).
- [97] A. Troisi and M. A. Ratner. Modeling the inelastic electron tunneling spectra of molecular wire junctions. *Phys. Rev. B*, 72:033408, (2005).
- [98] W. Andreoni, A. Curioni, and H. Gronbeck. *Int. J. Quantum Chem.*, 80:598, (2000).
- [99] P. Fenter, F. Schreiber, L. Berman, G. Scoles, P. Eisenberger, and M. J. Bedzyk. On the structure and evolution of the buried S/Au interface in self-assembled monolayers: X-ray standing wave results. *Surf. Sci.*, 412/413:213, (1998).
-

-
- [100] G. J. Kluth, C. Carraro, and R. Marboudian. Direct observation of sulfur dimers in alkanethiol self-assembled monolayers on Au(111). *Phys. Rev. B*, 59:449, (1999).
- [101] M. S. Yeganeh, S. M. Dougal, R. S. Polizzotti, and P. Rabinowitz. Interfacial atomic structure of a self-assembled alkyl thiol monolayer/Au(111): A sum frequency generation-study. *Phys. Rev. Lett.*, 74:1811, (1995).
- [102] Y. Akinaga, T. Nakajima, and K. Hirao. A density functional study on the adsorption of methanethiolate on the (111) surfaces of noble metals. *J. Chem. Phys.*, 114:8555, (2001).
- [103] Y. Yourdshahyan and A. M. Rappe. Structure and energetics of alkanethiol adsorption on the Au(111) surface. *J. Chem. Phys.*, 117:825, (2002).
- [104] L. M. Molina and B. Hammer. Theoretical study of thiol-induced reconstructions on the Au(111) surface. *Chem. Phys. Lett.*, 360:264, (2002).
- [105] C. D. Bain, E. B. Troughton, Y.-T. Tao, J. Evall, M. Whitesides, George, and R. G. Nuzzo. Formation of monolayer films by the spontaneous assembly of organic thiols from solution onto gold. *J. Am. Chem. Soc.*, 111 (1):321, (1989).
- [106] L. H. Dubois, B. R. Zegarski, and R. G. Nuzzo. Molecular ordering of organosulfur compounds on Au(111) and Au(100): Adsorption from solution and in ultrahigh vacuum. *J. Chem. Phys.*, 98 (1):678, (1993).
- [107] M. D. Porter, T. B. Bright, D. L. Allara, and C. E. D. Chidsey. Spontaneously organized molecular assemblies. 4. Structural characterization of n-alkyl thiol monolayers on gold by optical ellipsometry, infrared spectroscopy, and electrochemistry. *J. Am. Chem. Soc.*, 109 (12):3559, (1987).
- [108] A. P. Scott and L. Radom. Harmonic vibrational frequencies: An evaluation of Hartree-Fock, Møller-Plesset, Quadratic Configuration Interaction, Density Functional Theory, and Semiempirical Scale Factors. *J. Phys. Chem.*, 100:16502, (1996).
- [109] K. W. Hipps and U. Mazur. *Handbook of Vibrational Spectrum*. Wiley, New York, 2002.
-

-
- [110] H. Basch, R. Cohen, and M. A. Ratner. Interface geometry and molecular junction conductance: Geometric fluctuation and stochastic switching. *Nano Lett.*, 5:1688, (2005).
- [111] H. Oevering, J. W. Verhoeven, M. N. Paddon-Row, E. Cotsaris, and N. S. Hush. Long-range exchange contribution to singlet-singlet energy transfer in a series of rigid bichromophoric molecules. *Chem. Phys. Lett.*, 8:117, (1985).
- [112] M. Brandbyge, M. R. Sorensen, and K. W. Jacobsen. Conductance eigenchannels in nanocontacts. *Phys. Rev. B*, 56:14956, (1997).
- [113] D. Djukic and J. M. van Ruitenbeek. Shot noise measurements on a single molecule. *Nano Lett.*, 6:789, (2006).
- [114] M. Kemp, A. Roitberg, V. Mujica, T. Wanta, and M. A. Ratner. Molecular wires: Extended coupling and disorder effects. *J. Phys. Chem.*, 100:8349, (1996).
- [115] M. Büttiker. Spatial variation of currents and fields due to localized scatterers in metallic conduction. *IBM J. Res. Dev.*, 32:63, (1988).
- [116] J. Heurich, J. C. Cuevas, W. Wenzel, and G. Schon. Electrical transport through single-molecule junctions: From molecular orbitals to conduction channels. *Phys. Rev. Lett.*, 88:256803, (2002).
- [117] J. C. Cuevas, A. L. Yeyati, and A. Martin-Rodero. Microscopic origin of conducting channels in metallic atomic-size contacts. *Phys. Rev. Lett.*, 80:1066, (1998).
- [118] D. Jacob and J. J. Palacios. Orbital eigenchannel analysis for ab initio quantum transport calculations. *Phys. Rev. B*, 73:075429, (2006).
- [119] A. Bagrets, N. Papanikolaou, and I. Mertig. Ab initio approach to the ballistic transport through single atoms. *Phys. Rev. B*, 73:045428, (2006).
- [120] A. Troisi and M. A. Ratner. Propensity rules for inelastic electron tunneling spectroscopy of single-molecule transport junctions. *J. Chem. Phys.*, 125, (2006).
-

- [121] M. Di Ventra, S. T. Pantelides, and N. D. Lang. First-principles calculation of transport properties of a molecular device. *Phys. Rev. Lett.*, 84:979, (2000).
- [122] J. B. Neaton, M. S. Hybertsen, and S. G. Louie. Renormalization of molecular electronic levels at metal-molecule interfaces. *Phys. Rev. Lett.*, 97:216405, (2006).
- [123] T. Niehaus, M. Rohlfing, F. Della Sala, A. Di Carlo, and T. Frauenheim. Quasiparticle energies for large molecules: A tight-binding-based Green's-function approach. *Phys. Rev. A*, 71:022508, (2005).
- [124] A. Gagliardi, T. A. Niehaus, T. Frauenheim, A. Pecchia, and A. Di Carlo. Quasiparticle correction for electronic transport in molecular wires. *J. Comp. Elect.*, 6:345, (2007).
- [125] A. Aviram and M. A. Ratner. Molecular rectifier. *Chem. Phys. Lett.*, 29:277, (1974).
- [126] F. Guinea, C. Tejedor, F. Flores, and E. Louis. Effective two-dimensional Hamiltonian at surfaces. *Phys. Rev. B*, 28:4397, (1983).
-

Own Publications

1. *The gDFTB Tool for Molecular Electronics*,
A. Pecchia, L. Latessa, A. Gagliardi, Th. Frauenheim, A. Di Carlo,
Molecular and Nano Electronics: Analysis, Design and Simulation, Vol. 17, Editor J. Seminario, Publisher Elsevier, 2006
 2. *A Priori Method for Propensity Rules for Inelastic Electron Tunneling Spectroscopy of Single-Molecule Conduction*,
A. Gagliardi, G. C. Solomon, A. Pecchia, Th. Frauenheim, A. Di Carlo, N. S. Hush and J. R. Reimers,
Physical Review B, 2007, 75, 174306.
 3. *Understanding the Inelastic Electron-Tunneling Spectra of Alkanedithiols on Gold*,
G. C. Solomon*, A. Gagliardi*, A. Pecchia, Th. Frauenheim, A. Di Carlo, J. R. Reimers and N. S. Hush,
Journal of Chemical Physics, 2006, 124, 094704.
 4. *Molecular Origins of Conduction Channels Observed in Shot-Noise Measurements*,
G. C. Solomon, A. Gagliardi, A. Pecchia, Th. Frauenheim, A. Di Carlo, J. R. Reimers and N. S. Hush,
Nano Letters, 2006, 6, 2431.
 5. *The Symmetry of Single-Molecule Conduction*,
G. C. Solomon, A. Gagliardi, A. Pecchia, Th. Frauenheim, A. Di Carlo, J. R. Reimers and N. S. Hush,
Journal of Chemical Physics, 2006, 125, 184702.
 6. *Incoherent Electron-Phonon Scattering in Octanethiols*,
A. Pecchia, A. Di Carlo, A. Gagliardi, S. Sanna, Th. Frauenheim and R. Gutierrez,
Nano Letters, 2004, 4, 2109.
-

7. *The Green's Function Density-Functional Tight-Binding (gDFTB) Method for Molecular-Electronic Conduction*,
J. R. Reimers, G. C. Solomon, A. Gagliardi, A. Bilić, N. S. Hush, Th. Frauenheim, A. Di Carlo and A. Pecchia,
Journal of Physical Chemistry A, 2007, 111, 5692.
8. *Simulations of Inelastic Tunnelling in Molecular Bridges*,
A. Gagliardi, G. C. Solomon, A. Pecchia, A. Di Carlo, T. Frauenheim, J. R. Reimers, N. S. Hush,
Non-Equilibrium Carrier Dynamics in Semiconductor, Vol. 110, Editor M. Saraniti and U. Ravaioli, Publisher Springer, 2006.
9. *Atomistic Simulation of the Electronic Transport in Organic Nanostructures: Electron-Phonon and Electron-Electron Interactions*,
A. Pecchia, A. Di Carlo, A. Gagliardi, Th. Niehaus and Th. Frauenheim,
Journal of Computational Electronics, 4, 79, 2005.
10. *Quasiparticle Correction for Electronic Transport in Molecular Wires*,
A. Gagliardi, Th. A. Niehaus, Th. Frauenheim, A. Pecchia and A. Di Carlo,
Journal of Computational Electronics, 2007, 6, 345.

* These authors contributed in a similar matter to publication.

Pieces of this thesis were published in (2), (3), (4), (5), (6) and (7).

Personal contributions

In the present work many topics were discussed. They were the results of collaborations with many people and groups. In this last paragraph the main personal contributions of the author are enlisted. The parts of the thesis which include new results are from Chapters 5 to Chapter 9. The principal contributions of the author are:

- Chapter 5: implementation of the Meir-Wingreen equation and the electron-phonon self-energies in the Landauer-Büttiker gDFTB code, Born approximation and part of the self consistent Born approximation. Implementation of the calculation for the electron-phonon couplings and the calculation of the power dissipated by virtual contacts.
- Chapter 6: Supervision for the code, analysis of the results with Dr. Alessandro Pecchia.
- Chapter 7: derivation of the simplified equation for the IETS. The contribution for all the calculations, analysis and conclusions are equally shared with Dr. Gemma C. Solomon.
- Chapter 8: Supervision for the code, analysis and discussion of the results with Dr. Gemma C. Solomon.
- Chapter 9: All the theoretical derivation, calculations, analysis and discussions performed by the author.

Acknowledgements

I am most grateful to Prof. Dr. Frauenheim for his friendship, help and for all the freedom he gave me in all these years. It is only thank to him if I was able to do so many collaboration and learning so much.

I want to acknowledge also Prof. Jeffrey R. Reimers, of the University of Sydney, for his invaluable help. I thank him also for his willingness and kindness. I am also indebted deeply to Prof. Aldo Di Carlo of the University “Tor Vergata” in Rome. It is only thank to him if I had the opportunity to start this PhD.

I want to express also my gratitude to some other people, first Dr. Alessandro Pecchia, for all the interesting discussions about science and life in general. I am most grateful also to Dr. Gemma C. Solomon for all the work done together and all the stimulating discussions we have in the last three years. A nice friend in the right side of the world. I deep in debt with Marius Wanko and Dr. Balint Aradi, especially for their revision of the manuscript of the thesis. I want to thank also Simone Lange and Simone Sanna for their friendship and assistance.

I am also very grateful to Prof. Noel S. Hush of the University of Sydney for the discussion concerning selection rules in inelastic electron tunneling spectroscopy. I would also express my gratitude to the entire group of Bremen Material Computer Science and the component of the previous group in Paderborn, in particular Pia Töelle, Dr. Thomas Niehaus and David Heringer. Thanks to all of them for all the help provided in these three years. Finally I want to acknowledge the group of Paderborn Institute for Scientific Computation (PaSco) for the support, the assistance and the funding provided during my PhD. My thanks to all those whom, by mistake, I forgot to mention.

The last part of the acknowledgment is in Italian, for some very special persons. Innanzitutto voglio ringraziare la mia famiglia, Enrica, mia madre, mio fratello, Silvia e Luciano. Persone senza le quali questo lavoro non sarebbe sicuramente mai stato concluso. A queste persone devo aggiungere un cane (Tango) e un gatto, anzi una Gatta (lei sa). Voglio inoltre ringraziare i miei amici piú stretti, Alessio, Andrea, Michele, Gabriele, Paolo, Mauro, Alessandro (Dottor) e Alberto. Molta strada si é fatta insieme e molta se ne fará ancora.

Per ultimi, ma non ultimi, due ringraziamneti speciali per due persone: una, purtroppo, partita e

l'altra appena arrivata. Mio padre e la piccola Giorgia. É stato infatti grazie a mio padre se ho cominciato ad apprezzare le scienze e quindi una buona parte del merito (o della colpa) se io sono qui é sua. Ricordo quando mi narró il primo racconto di fantascienza, "Incontro con Rama" di Arthur Clarke. Il suo riassunto puó essere integralmente riportato su queste pagine: "Una astronave aliena arriva nel nostro sistema solare e se ne va". Mio padre era cosí, ingegnere fino al midollo. Quando chiesi maggiori dettagli mi regaló la sua edizione del romanzo. La seconda persona é appena nata. Questa Tesi é anche dedicata a lei e spero che le porti fortuna.
